

REPORT DOCUMENTATION PAGE

AFRL-SR-BL-TR-01-

Public reporting burden for this collection of information is estimated to average 1 hour per response, including the time for reviewing the data needed, and completing and reviewing this collection of information. Send comments regarding this burden estimate or any reducing this burden to Department of Defense, Washington Headquarters Services, Directorate for Information Operations and Reports, 22202-4302. Respondents should be aware that notwithstanding any other provision of law, no person shall be subject to any penalty for not providing information if it does not have a currently valid OMB control number. PLEASE DO NOT RETURN YOUR FORM TO THE ABOVE ADDRESS.

1. REPORT DATE (DD-MM-YYYY) 02-01-2001		2. REPORT TYPE Final Technical		3. DATES COVERED (From - To) 02/1997-09/2000	
4. TITLE AND SUBTITLE Weakly Compressible Descriptions of Turbulence in Compressible Flows				5a. CONTRACT NUMBER F49620-97-1-0089	
				5b. GRANT NUMBER	
				5c. PROGRAM ELEMENT NUMBER	
				5d. PROJECT NUMBER	
6. AUTHOR(S) Robert D. Moser				5e. TASK NUMBER	
				5f. WORK UNIT NUMBER	
				8. PERFORMING ORGANIZATION REPORT NUMBER	
7. PERFORMING ORGANIZATION NAME(S) AND ADDRESS(ES) University of Illinois at Urbana-Champaign, Urbana, IL 61801					
9. SPONSORING / MONITORING AGENCY NAME(S) AND ADDRESS(ES) AFOSR 801 N. Randolph St. Room 732 Arlington, VA 22203-1977				10. SPONSOR/MONITOR'S ACRONYM(S) AFOSR	
				11. SPONSOR/MONITOR'S REPORT NUMBER(S)	

12. DISTRIBUTION / AVAILABILITY STATEMENT

Unlimited, Appendix A copyright Cambridge University Press

AIR FORCE OFFICE OF SCIENTIFIC RESEARCH (AFOSR)
NOTICE OF TRANSMITTAL DTIC. THIS TECHNICAL REPORT
HAS BEEN REVIEWED AND IS APPROVED FOR PUBLIC RELEASE
LAW AFR 190-12. DISTRIBUTION IS UNLIMITED.

13. SUPPLEMENTARY NOTES

14. ABSTRACT

Weakly compressible asymptotics and direct numerical simulation are used to investigate the effects of compressibility on high speed turbulent shear layers. The asymptotic analysis leads to a decomposition procedure that can be used to approximately determine the acoustic and nonacoustic components of a compressible flow. In boundary layers, it is found that the acoustic fluctuations are only weakly coupled to the nonacoustic, so equations describing only the nonacoustic fluctuations (incompressible, variable density) would provide a good description of the turbulence.

20010220 070

15. SUBJECT TERMS

Turbulence, Compressible, Boundary Layer, Mixing Layer

16. SECURITY CLASSIFICATION OF:

a. REPORT

b. ABSTRACT

c. THIS PAGE

17. LIMITATION OF ABSTRACT

UU

18. NUMBER OF PAGES

19a. NAME OF RESPONSIBLE PERSON

19b. TELEPHONE NUMBER (include area code)

Standard Form 298 (Rev. 8-98)
Prescribed by ANSI Std. Z39.18

DTIC QUALITY INSPECTED 1

WEAKLY COMPRESSIBLE DESCRIPTIONS OF TURBULENCE IN COMPRESSIBLE FLOWS

Final Report for Grant F49620-97-1-0089

Robert D. Moser
Department of Theoretical and Applied Mechanics
University of Illinois, Urbana-Champaign

1 Motivation and Objectives

A large fraction of the effort in turbulence research, including numerical simulations, experiments, theory and modeling, has been directed toward incompressible turbulence. This is largely due to the simplifications that the incompressible assumption allows, and to the belief that turbulence is in essence an incompressible phenomenon. However, many of the flows of technological interest are compressible (e.g. external aerodynamics, propulsion systems) leading to the requirement that our understanding of incompressible turbulence be translated to these compressible flows. An example of this is that most commonly used turbulence models for compressible flows are modifications of models developed for incompressible flows (e.g. the k - ϵ model).

Fortunately, in many flows the small-scale turbulence is nearly incompressible, albeit with non-constant density, even though the flow itself is highly compressible. For example, in much of the literature on compressible boundary layers (see the review by Spina et al., 1994), differences relative to an incompressible boundary layer (up to $M = 5$, say) are understood as being caused by variations in the mean density across the layer. This has long been appreciated and is the basis of the Van Driest (Van Driest 1951, 1956) transformation and the Morkovin hypothesis (Morkovin 1961).

These observations suggest that a formulation based on low Mach number asymptotics, in which the turbulence is treated as weakly compressible while the mean is considered to be fully compressible, would provide a good description of the boundary layer to quite large Mach numbers, and a rational basis for the development of compressible turbulence models. Aided by direct numerical simulation data, the research under this grant is aimed at developing and evaluating such weakly compressible descriptions of compressible turbulence.

2 Supported Research

There were four primary research activities supported under this grant, all aimed at the weakly compressible analysis of turbulence in compressible shear layers. These activities are listed below:

1. Direct numerical simulation of a compressible boundary layer at $Ma = 2.5$
2. Low Mach-number asymptotic analysis and numerical decomposition of compressible boundary layers.
3. Development and implementation of a new B-spline collocation numerical method for the numerical simulation of compressible shear layers.
4. Numerical simulation and analysis of compressible mixing layers.

The key results of each of these activities will be described briefly below. More details are available in the papers attached as appendices.

2.1 DNS of a Compressible Boundary Layer

Using a technique similar to that of Spalart (1989) to homogenize the streamwise direction, a Mach 2.5 compressible boundary layer was simulated. A B-spline Galerkin method was used and the simulation was performed in a computational domain large enough to eliminate most finite domain size effects. The simulation was used to evaluate a variety of approximations used in the modeling of compressible boundary layers. For example, the Strong Reynolds Analogy (Morkovin, 1961) was evaluated and found to be in disagreement with the DNS data when applied in its most common form. Valid approximations were also determined. Of particular interest to this project was the determination that the velocity-temperature correlation was consistent with that in an incompressible boundary layer.

The details of the simulation and the results were reported in Guarini et al (2000), a reprint of which is included as appendix A. This research activity was also sponsored by the NASA-Ames Research Center through a Graduate Research Fellowship for Guarini. The efforts of the PI and computer resources at HPCMP were supported through the current grant.

2.2 Analysis of Compressible Turbulent Boundary Layers

A weakly compressible asymptotic analysis similar to that of Zank & Matthaeus (1991) was developed for the turbulence in a compressible boundary layer. In developing such

an asymptotic analysis, a variety of different assumptions can be made regarding scaling of different components of the compressible fields. The direct numerical simulation data of Maeder, Adams & Kleiser (2000) at three Mach numbers (3, 4.5 and 6) were analyzed to determine the appropriate scalings. Further, it was determined that unlike the heat-flux dominated approximations of Zank & Matthaeus (1991), the acoustic contributions to some quantities (e.g. pressure fluctuations and velocity dilatation) are not negligible. To evaluate the impact of acoustics on the turbulent boundary layer, a decomposition procedure was devised to allow a compressible turbulent field to be decomposed into acoustic and non-acoustic parts. This decomposition was applied to the DNS data of Maeder et al (2000). The asymptotic analysis suggests and the decomposition analysis confirms that the acoustic fluctuations are only weakly coupled to the nonacoustic, even at $Ma = 6$. The nonacoustic equations are thus autonomous, and can be considered to be the governing equations for the turbulence in the compressible boundary layer. These equations can thus be used as a basis for further simulation and modeling.

The decomposition analysis and its results are described in a paper under consideration for publication in Theoretical and Computational Fluid Dynamics (Borodai & Moser, 2000), and a preprint is included as Appendix B.

The consequences to modeling approximations of the low Mach number asymptotics and the autonomous nonacoustic governing equations is being explored. Several are already clear. For example, this analysis shows that the pressure-dilatation correlation and the so called dilatational dissipation, both terms in the equation for turbulent kinetic energy, should be negligibly small, as has been recently observed in DNS data. The analysis also suggests that the statistics of the compressible turbulent boundary layer should be related to those of incompressible boundary layers with passive scalars. This connection is continuing to be explored.

2.3 Development of Compressible Shear Layer Code

Experience with the boundary layer simulation described above indicated that the Galerkin formulation had several practical shortcomings, the most obvious being inefficiencies inherent in evaluation of nonlinear terms. B-spline collocation methods do not suffer from this shortcoming. Furthermore it was determined that they have several other desirable features. In particular, these collocation methods have better resolution properties than the related Galerkin methods. A detailed comparison of these B-spline collocation methods with other high-resolution methods was conducted, and as a result, they were selected as the basis for a new implementation of a compressible shear flow code. This code is being used for the mixing layer simulation discussed in 2.4 below.

The results of the numerical methods evaluations are the subject of a paper being considered for publication in Journal of Computational Physics (Kwok, Moser & Jimenez, 2000), and a preprint of this paper is included as Appendix C.

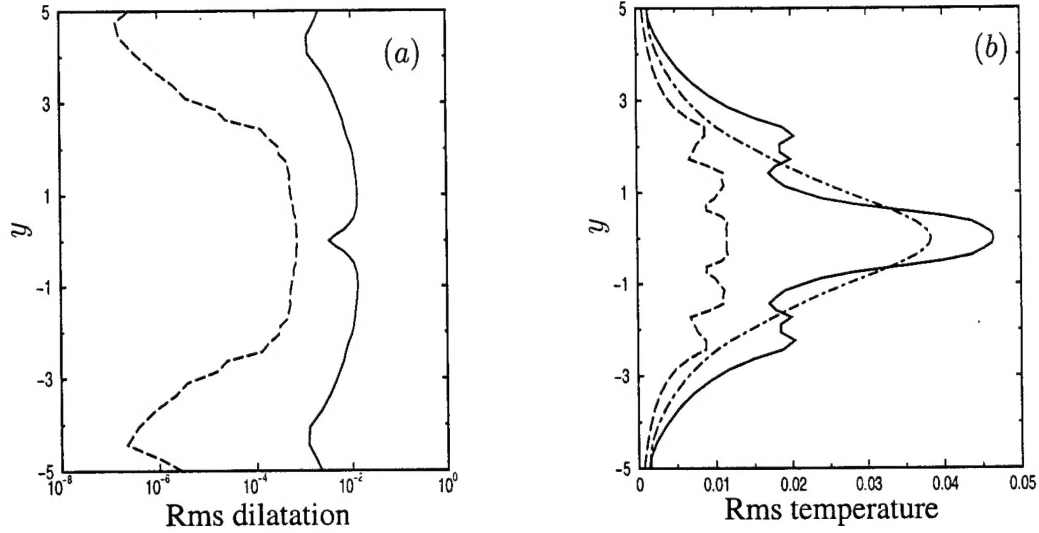


Figure 1: Rms of a) velocity divergence and b) temperature fluctuations in a two-dimensional $Ma_c = 0.4$ mixing layer. Shown are —total, ---, nonacoustic and -.-acoustic contributions

2.4 Simulation and Analysis of Mixing Layers

The compressible shear layer code described in 2.3 is being used to perform simulations of compressible mixing layers. Free shear layers, such as the mixing layer are known to exhibit much stronger compressibility effects than boundary layers at similar free-stream Mach numbers. They are thus of great interest in investigating the coupling of acoustic fluctuations with turbulence. A decomposition analysis similar to that for the boundary layer is being applied to the mixing layer.

Two-dimensional mixing layer simulations with convective Mach number of 0.4 and 0.8 were carried out to provide input for both the theory development and planned three dimensional simulations. In particular, the simulations provide critical information on the relative importance of incompressible, acoustic and thermal parts of the velocity, temperature, pressure and density fields. For a mixing layer with equal free-stream temperatures, we expect the thermal fluctuations to be less important than in the boundary layer, since the mean temperature gradients are small. Indeed, for a mixing layer with $Ma_c = 0.4$, the thermal velocity dilatation is much smaller than the acoustic dilatation, and the thermal and acoustic temperature fluctuations are of the same magnitude (Figure 1). Thus in this case, the thermal component of the flow is one order higher than that for the boundary layer. This requires minor adjustment to the decomposition procedure.

The acoustic and nonacoustic dilatation and temperature fluctuations were determined as in the boundary layer starting from the equation

$$\gamma \bar{p} \frac{\partial u'_{nj}}{\partial x_j} = \frac{\gamma - 1}{Pr Re} \frac{\partial}{\partial x_k} \left(\mu_n \frac{\partial T'_n}{\partial x_k} \right). \quad (1)$$

This is remarkably successful, even at quite high Mach numbers. For example at $Ma_c = 0.8$,

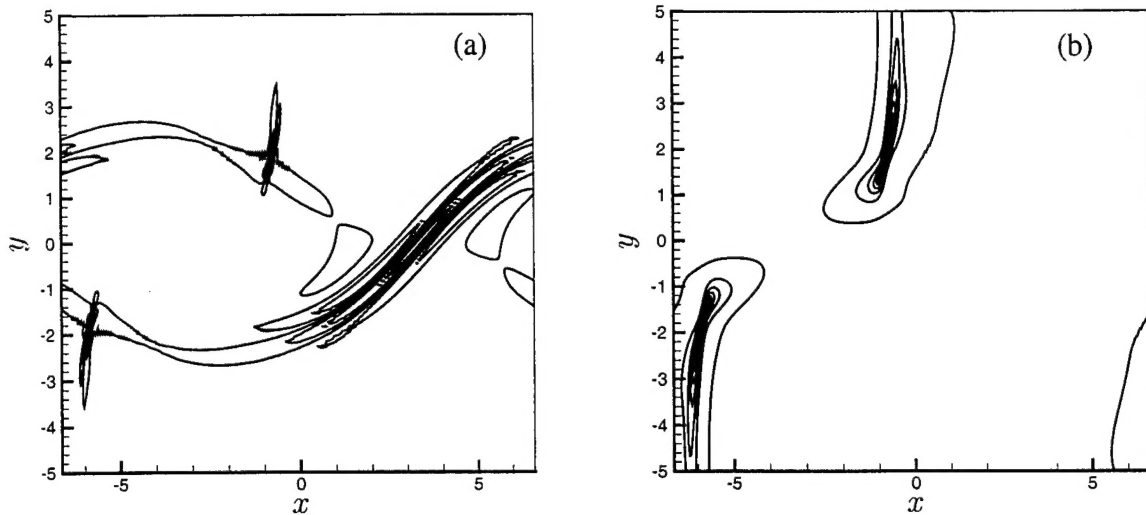


Figure 2: Contours of velocity divergence in a $Ma = 0.8$ mixing layer. Shown are a) the contribution from thermal fluctuations, and b) the contribution from acoustic fluctuations. The shock is clearly visible in b).

where in the two-dimensional mixing layer, eddy shocklets appear, this decomposition correctly isolates the shock dilatation in the acoustic field (Figure 2).

Numerical simulations of three-dimensional compressible shear layers are now under way. These simulations are begun with initial conditions taken from the incompressible simulations of Rogers & Moser (1994). In addition to providing the turbulence fields required to apply the decomposition analysis. These new simulations allow compressibility effects to be evaluated directly by comparison to the evolutions of the incompressible fields.

3 Other Information

Supported under this grant have been Stanislov Borodai and Wai-Yip Kwok, both graduate students in the TAM department at University of Illinois. The work supported here was presented at the 1997, 1998 and 1999 meetings of the Division of Fluid Dynamics of the American Physical Society, and three papers have resulted from this work (Borodai & Moser, 2000, Kwok, Moser & Jimenez, 2000, Guarini et al., 2000).

Acknowledgment

This work is sponsored by the Air Force Office of Scientific Research, USAF, under grant/contract number F49620-97-1-0089.

References

- S. Borodai and R. D. Moser 2000 The decomposition of compressible boundary layer turbulence into acoustic and variable density parts, Submitted to *Theo. Comp. Fluid Mech.*
- S. E. Guarini, R. D. Moser, K. Shariff & A. Wray 2000 Direct numerical simulation of a supersonic turbulent boundary layer at $M = 2.5$, *J. Fluid Mech.* **414**, 1-33.
- W. Y. Kwok, R. D. Moser and J. Jimenez 1999 A critical evaluation of the resolution properties of B-spline and compact finite difference methods. Submitted to *J. Comput. Physics*.
- T. Maeder, N. A. Adams, and L. Kleiser 2000 Direct simulation of turbulent supersonic boundary layers by an extended temporal approach. Submitted to *Journal of Fluid Mechanics*.
- M. V. Morkovin 1961 Effects of compressibility on turbulent flows. In *Mecanique de la Turbulence*, ed. A. Favre, 367-380.
- M. M. Rogers and R. D. Moser 1994 Direct simulation of a self-similar turbulent mixing layer, *Phys. Fluids A*, **6**, 902-923.
- Spalart, P. R. 1989 Direct simulation of a turbulent boundary layer up to $R_\theta = 1410$, *J. Fluid Mech* **187**, 61-98.
- E. Spina, A. Smits, and S. K. Robinson 1994 The Physics of Supersonic Turbulent Boundary Layers. *Ann. Rev. Fluid Mechanics*, **26**, 287.
- E. R. Van Driest 1951 Turbulent Boundary Layer in Compressible Fluids. *J. Aeronaut. Sci.*, **18**, 145.
- E. R. Van Driest 1956 On Turbulent Flow Near a Wall. *J. Aeronaut. Sci.*, **23**, 1007.
- G. P. Zank and W. H. Matthaeus 1991 The equations of nearly incompressible fluids. 1. Hydrodynamics, turbulence and waves. *Phys. Fluids A*, **3**, 69-82.

APPENDIX A

Reprint of "Direct numerical simulation of a supersonic turbulent boundary layer at $M = 2.5$ " by S. E. Guarini, R. D. Moser, K. Shariff & A. Wray (2000) from *J. Fluid Mech.* **414**, pages 1-33.

Direct numerical simulation of a supersonic turbulent boundary layer at Mach 2.5

By STEPHEN E. GUARINI¹, ROBERT D. MOSER²
KARIM SHARIFF¹ AND ALAN WRAY¹

¹NASA-Ames Research Center, Moffett Field, CA 94035, USA

²Department of Theoretical and Applied Mechanics, University of Illinois,
Urbana, IL 61801, USA

(Received 20 March 1999 and in revised form 21 January 2000)

A direct numerical simulation of a supersonic turbulent boundary layer has been performed. We take advantage of a technique developed by Spalart for incompressible flow. In this technique, it is assumed that the boundary layer grows so slowly in the streamwise direction that the turbulence can be treated as approximately homogeneous in this direction. The slow growth is accounted for by a coordinate transformation and a multiple-scale analysis. The result is a modified system of equations, in which the flow is homogeneous in both the streamwise and spanwise directions, and which represents the state of the boundary layer at a given streamwise location. The equations are solved using a mixed Fourier and B-spline Galerkin method.

Results are presented for a case having an adiabatic wall, a Mach number of $M = 2.5$, and a Reynolds number, based on momentum integral thickness and wall viscosity, of $Re_{\theta^*} = 849$. The Reynolds number based on momentum integral thickness and free-stream viscosity is $Re_{\theta} = 1577$. The results indicate that the Van Driest transformed velocity satisfies the incompressible scalings and a small logarithmic region is obtained. Both turbulence intensities and the Reynolds shear stress compare well with the incompressible simulations of Spalart when scaled by mean density. Pressure fluctuations are higher than in incompressible flow. Morkovin's prediction that streamwise velocity and temperature fluctuations should be anti-correlated, which happens to be supported by compressible experiments, does not hold in the simulation. Instead, a relationship is found between the rates of turbulent heat and momentum transfer. The turbulent kinetic energy budget is computed and compared with the budgets from Spalart's incompressible simulations.

1. Introduction

The study of supersonic turbulent boundary layers has primarily consisted of experimental investigations with a few recent attempts at numerical simulation. The experimental measurements are limited to basic turbulence quantities and by the spatial resolution near the wall, among other difficulties. The simulations have been hampered by large cost and low Reynolds number. The goal of the present work was to identify similarities and differences between compressible and incompressible boundary layers, as well as to test the applicability of Morkovin's hypothesis and the strong Reynolds analogy.

1.1. Background and motivations

Though most flows encountered in nature and in aerospace applications are turbulent or partially so, turbulence remains one of the most elusive subjects in aeronautics. There is no general turbulence theory or model. With the addition of compressibility the turbulence problem becomes even more complex. For instance, in boundary layers at high Mach numbers, large temperature gradients develop between the wall region and the outer layer. These gradients result in large variations of mean fluid properties, such as viscosity, which result in significant changes in the Reynolds number across the wall-normal direction. As the Mach number becomes hypersonic, shocks may form, dilatation becomes important, and baroclinic terms may be significant.

To account for the effects of compressibility, many theories have been developed based on a weakly compressible hypothesis (see the review by Spina, Smits & Robinson 1994). The hypothesis is that, at moderate free-stream Mach numbers ($M \lesssim 5$ according to Morkovin 1962), dilatation is small and any differences from incompressible turbulence can be accounted for by fluid property variations across the layer. This has long been appreciated and is the basis of the Van Driest (1951, 1956) transformation and the Morkovin (1962) hypothesis. Morkovin postulates that in the weak compressibility regime normal stresses will obey the incompressible scaling when they are multiplied by the local mean density divided by the free-stream value. Even at moderate free-stream Mach numbers the fluctuating and turbulence Mach numbers are small and one would not expect eddy shocklets to be a predominant feature of the flow field. However, at higher free-stream Mach numbers the turbulent velocity fluctuations are more likely to be supersonic leading to increased compressibility effects. Further support for the weak compressibility assumption is provided by the fact that large-scale structures are convected at $0.9U_\infty$ (Spina, Donovan & Smits 1991) which results in a small relative Mach number between the large eddies and the mean flow. Finally, another measure of compressibility, the gradient Mach number (Sarkar 1995), is also small in the boundary layer. The gradient Mach number is based on the velocity difference across the scale of an eddy.

The validity of the weak compressibility theories in compressible boundary layers has been checked in a variety of experiments over the years (see these and the references therein: Gaviglio 1987; Smith & Smits 1993; and Eléna & Gaviglio 1993). However, in most experiments the data reported have been limited to simple turbulence quantities such as the mean and RMS velocity and temperature. Detailed correlation statistics needed to directly check the validity of Morkovin's hypothesis are only available from a few experiments. The data from the direct numerical simulations reported here provide an opportunity to evaluate these theories in more detail than has been previously possible.

1.2. Previous simulations

Although there have been numerous experimental investigations of the compressible turbulent boundary layer, there have been relatively few attempts at direct numerical simulation of this flow. To date there have been three such attempts known to us: (i) Guo & Adams (1994) and Adams *et al.* (1998); (ii) Rai, Gatski & Erlebacher (1995); and (iii) Hatay & Biringen (1995).

The simulations of Guo & Adams and Adams *et al.* had an isothermal wall at the laminar adiabatic wall temperature and, like the current simulations, used a method that transformed the spatially evolving boundary layer into a parallel, streamwise homogeneous flow. To obtain their transformed parallel shear flow, Guo & Adams

(1994) require that the spatial mean of the periodic simulation obey the parabolized time-mean equations. These equations contain streamwise derivatives of Reynolds stresses which are obtained by performing simulations at different downstream stations. This approach leads to forcing terms in the mean equations that are similar to those produced by Spalart's approach, except that terms involving the coordinate transformation are not present.

Guo & Adams (1994) and Adams *et al.* (1998) simulate boundary layers at three Mach numbers $M = 3, 4.5$ and 6 . In Guo & Adams, these simulations were performed in relatively small spatial domains; in particular, for $M = 3$ the domain was 16 times smaller in streamwise by spanwise area than those reported here. The effects of these small domains is evident in their statistical results, most notably the two-point correlations. Such small domains introduce considerable uncertainty regarding the impact of the domain size on the dynamics of the boundary layer, though experience with the minimal channel (Jimenez & Moin 1991) suggests that basic statistical quantities such as turbulence intensities should be reasonably accurate. One of the major design considerations of the current simulations was to avoid the uncertainties associated with such small simulation domains.

Unlike the current simulations and those of Guo & Adams, Rai *et al.* (1995) simulated a true spatially evolving boundary layer. They simulated a very long streamwise domain from a laminar inlet, through transition to a fully turbulent boundary layer. This clearly avoids any uncertainties that might be associated with the approximate spatial growth treatment used here and in Guo & Adams, but the cost is that the spatial domain that must be simulated is spectacularly large. As a result, even with the extremely large problem size they were able to run (17 million nodes), Rai *et al.*'s resolution was over a factor of 3 coarser in the streamwise direction (measured in wall units) than the current simulations. Such coarse resolution introduces uncertainties that are different from those associated with the approximate spatial growth treatment. Simulations like that reported here, which can be run with much better spatial resolution, are useful for assessing the impact of the coarse resolution that must be used in a simulation like that of Rai *et al.*

Finally, Hatay & Biringen (1995) performed a parallel-flow boundary layer calculation at $M = 2.5$. However, the data they present suggest that the turbulence is not being sustained. Indeed, the turbulence intensities appear to drop significantly over the course of the simulation. It is possible that the Reynolds number of their simulation is too low to sustain turbulence. The authors quote a Reynolds number based on displacement thickness of $Re_{\delta^*} \approx 1000$, which corresponds to a momentum-thickness Reynolds number of $Re_{\theta} \approx 140$. Fernholz & Finley (1980) call flows in the Reynolds number range of $300 \leq Re_{\theta} \leq 6000$ transitional, based on an analysis of mean velocity profiles. While their definition of transitional flows does not preclude having sustained turbulence below $Re_{\theta} \approx 300$, the Reynolds number in Hatay & Biringen's simulation is well below the lower limit of this range.

Clearly, the direct numerical simulation of a compressible turbulent boundary layer is a difficult undertaking, in which various compromises must be made to make the simulation practical. In the research reported here, we have pursued the most reliable compressible boundary layer simulation that we were able to do with current computation capabilities, choosing good spatial resolution and adequate domain size over true spatial evolution. Such a simulation allows a much more detailed analysis of compressibility effects in the boundary layer than has been previously possible. The current simulation will be described and analysed in what follows, which includes simulation details (§2), turbulence statistics (§3), Reynolds analogies

(§4), the turbulent kinetic energy budget (§5) and conclusions (§6). The details of the approximate spatial growth treatment are given in the Appendix.

2. Simulation details

The details of the current simulation are provided in this section. The parameters used in the compressible turbulent boundary layer simulation are compared with the incompressible boundary layer simulations of Spalart (1988); the incompressible channel simulation of Kim, Moin & Moser (1987); and the compressible boundary layer simulations of Guo & Adams (1994) and Rai *et al.* (1995).

2.1. Simulation method

One difficulty in performing compressible turbulent boundary layer simulations is that the streamwise direction is inhomogeneous. This precludes the use of periodic boundary conditions, and as a result FFTs, in this direction. Furthermore it necessitates use of a long entrance length for the flow to adjust from artificial in-flow conditions.

Several techniques have been developed to address one or both of these issues for incompressible flow (Spalart & Leonard 1987; Spalart 1988; Spalart & Watmuff 1993; Bertolotti, Herbert & Spalart (1992); and Lund, Wu & Squires 1998). Of these we utilize the one developed in Spalart & Leonard (1987) and Spalart (1988). Spalart recognized that the slow growth of the boundary layer in the streamwise direction makes it possible to treat the turbulence as approximately homogeneous in this direction. The slow growth is taken into account by using a coordinate transformation and a transformation of dependent variables as in multi-scale asymptotics. The result is a modified system of equations (Navier–Stokes plus some extra terms, which we shall call ‘slow growth terms’) that is homogeneous in both the streamwise and spanwise directions, and which represents the state of the boundary layer at a given streamwise location (or, equivalently, a given thickness). Using Spalart’s method, the boundary layer can be simulated separately at each streamwise station. A detailed description of this method and the modified set of equations can be found in the Appendix.

The resulting equations are solved using a mixed Fourier-spectral and B-spline-Galerkin method (Guarini 1998). The dependent variables (specific volume, $\sigma = 1/\rho$; momentum, $m = \rho u$; and pressure, p) are expanded in terms of a Fourier representation in the horizontal directions and a third-order (quadratic) B-spline representation in the wall-normal direction. The Fourier directions are de-aliased using the 3/2-rule, where all nonlinear terms are calculated using 3/2 times the number of modes used to advance the solution. Quadratic nonlinearities are fully de-aliased using this rule while higher-order nonlinearities are only partially de-aliased. B-splines have a variety of good numerical properties, and have been used successfully in the incompressible pipe flow simulation of Loulou (1996) and the compressible jet of Rao (1997). B-splines have high resolving power, allow easy implementation of boundary conditions, and allow the use of stretched grids. More details on B-splines may be found in: De Boor (1978), Kravchenko, Moin & Moser (1996), and Shariff & Moser (1998). Their use in the present work is described in Guarini (1998). In the wall-normal direction, Giles’ (1989, 1990) second-order non-reflecting boundary conditions are used at the free-stream boundary and adiabatic no-slip boundary conditions are used at the wall. This combination of splines and Fourier methods produces a very accurate numerical method. For the time discretization the mixed implicit/explicit method of Spalart, Moser & Rogers (1991) is used. All terms are

Sim.	M	Re_θ	$N_x \times N_z$	$L_x^+ \times L_z^+$	$\Delta x^+ \times \Delta z^+$
S1	0.0	225	—	—	—
S2	0.0	300	85×64	$2680^+ \times 670^+$	$31.5^+ \times 10.5^+$
S3	0.0	670	171×128	$4900^+ \times 1225^+$	$28.7^+ \times 9.50^+$
S4	0.0	1410	288×213	$11400^+ \times 2850^+$	$39.6^+ \times 13.4^+$
KMM	0.0	—	192×160	$2300^+ \times 1150^+$	$12.0^+ \times 7.00^+$
GA	3.0	3015	192×144	$527^+ \times 300^+$	$2.74^+ \times 2.08^+$
GA	4.5	2618	180×144	$260^+ \times 155^+$	$1.44^+ \times 1.08^+$
GA	6.0	2652	180×128	$229^+ \times 137^+$	$1.27^+ \times 1.07^+$
Rai	2.25	6000	971×321	full spatial	$27.0^+ \times 10.4^+$
Present	2.5	1577	256×192	$2269^+ \times 1134^+$	$8.86^+ \times 5.91^+$

TABLE 1. Comparison of parameters used in the incompressible simulations of Spalart (1988) (S1–S4) and Kim *et al.* (1987) (KMM); the compressible simulations of Guo & Adams (1994) (GA) and Rai *et al.* (1995); and the present simulation.

treated explicitly except for the highest wall-normal derivative in the viscous, pressure gradient, and ‘acoustic coupling term’

$$\gamma \sigma p \frac{\partial m_2}{\partial x_2}, \quad (2.1)$$

that appears in the pressure equation. In the implicit treatment, non-constant coefficients that vary in the horizontal directions cannot be easily treated. Both the viscous and acoustic coupling terms are split into a term with coefficients (viscosity and σp respectively) varying in the wall-normal direction only, which is treated implicitly, and the remainder, which is treated explicitly.

2.2. Choice of parameters

A turbulent boundary layer at a Mach number of 2.5 and a Reynolds number based on displacement thickness of $Re_{\delta^*} = 6258$ was simulated. This results in a Reynolds number based on momentum integral thickness and wall viscosity of $Re_{\theta} \approx 849$. The Reynolds number based on momentum integral thickness and free-stream viscosity was $Re_\theta \approx 1577$. The Mach number was chosen because of the availability of experimental data and because it is in a range where we might begin to see some compressibility effects.

There are two important sets of parameters, the grid size ($N_x \times N_y \times N_z$) and the domain size ($L_x \times L_y \times L_z$), that determine the overall quality/accuracy of the simulation. The coordinate system is oriented such that the x -, y -, and z -directions are the streamwise, wall-normal, and spanwise directions, respectively (in this paper we use a mixed index or symbol notation where x_1 , x_2 , and x_3 correspond to x , y , and z , respectively). The current simulation has $256 \times 209 \times 192$ ($N_x \times N_y \times N_z$) Fourier–B-spline modes and a domain size of $2269^+ \times 875^+ \times 1134^+$ ($L_x \times L_y \times L_z$), where $y^+ = y u_\tau / \nu_w$. Here ν_w is the kinematic viscosity at the wall and u_τ is the friction velocity $(\tau_w / \rho_w)^{1/2}$, where τ_w and ρ_w are the shear stress and density at the wall, respectively. The domain and grid parameters were selected to provide sufficient resolution in a domain that is large enough to eliminate most finite domain size effects. That this is the case is demonstrated below.

One way to assess the adequacy of the resolution and domain size is by comparison to DNS of similar flows. The resolution and domain size used in the current simulation

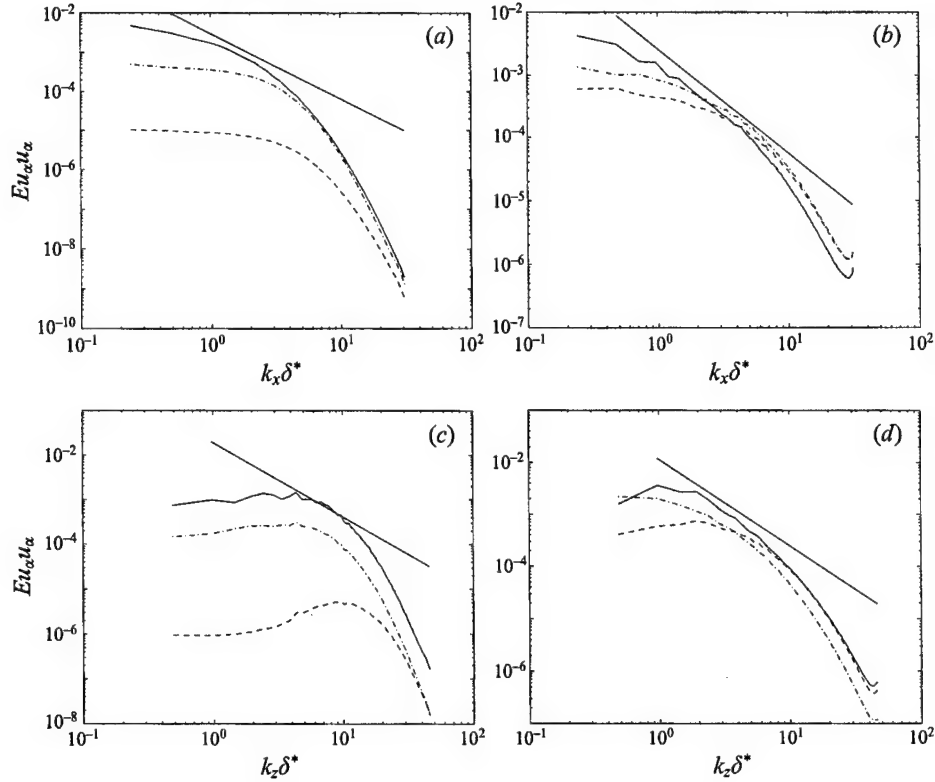


FIGURE 1. One dimensional energy spectra $E_{u_i u_i}$. Plotted versus (a) k_x at $y^+ = 4$; (b) k_x at $y^+ = 80$; (c) k_z at $y^+ = 4$; (d) k_z at $y^+ = 80$. —, Streamwise velocity component; ----, wall-normal velocity component; - · -, spanwise velocity component.

are compared with the incompressible boundary layer simulations of Spalart (1988) (S1–S4), the incompressible channel flow of Kim *et al.* (1987) (KMM) and the compressible boundary layer simulations of Guo & Adams (1994) (GA) (table 1). The resolution required in the $M = 3$ simulation of Guo & Adams was significantly finer than that of the incompressible simulations or the present simulation. The reason for Guo & Adams' extremely fine resolution is not clear. However, the need for increased resolution of the current simulation relative to KMM is due to sharp density gradients present in the compressible flow. KMM is used for comparison because their resolution is better than Spalart's simulations, as determined by the drop in energy spectra. The adequacy of the spatial resolution was confirmed by examining the spectra, where $E_{u_i u_i}$ is the energy spectrum for the velocity component u_i . Examples are shown in figure 1. These spectra and those at other y -locations suggest the resolution is adequate. Another indication of the adequacy of the resolution is the value of $k_{max}\eta$, where k_{max} is the maximum wavenumber in x and η is the local Kolmogorov scale. The maximum and minimum of this value in the current simulation are 1.6 and 0.5, respectively, which is considered adequate. For comparison the simulation of Kim *et al.* (1987) had values of 1 and 0.4 for the maximum and minimum, respectively.

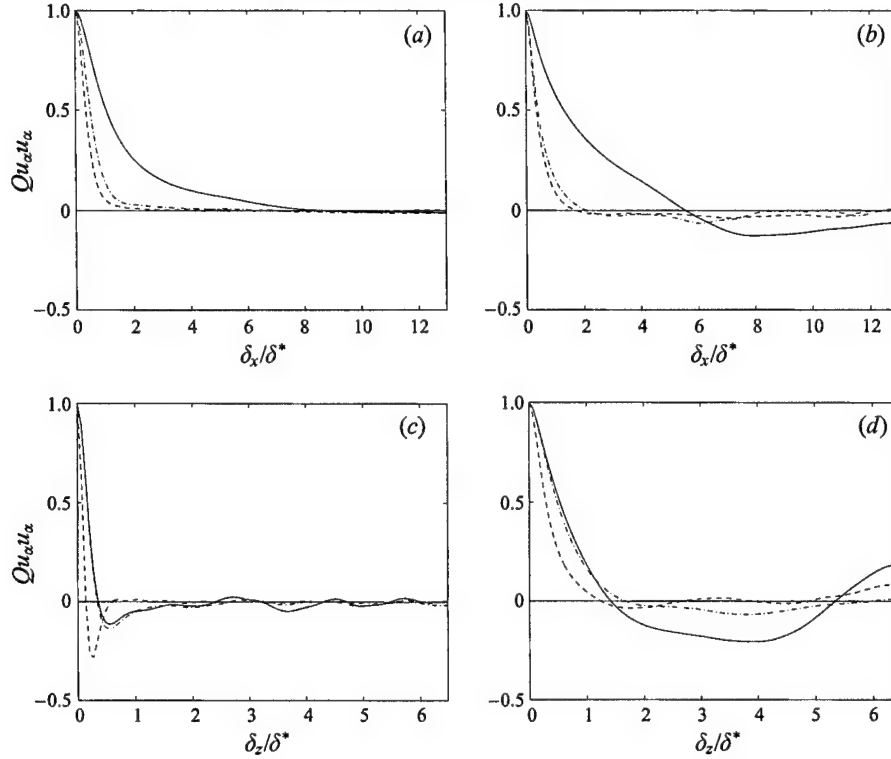


FIGURE 2. Two-point correlations $Q_{u_i u_i}$. Plotted versus (a) δ_x/δ^* at $y^+ = 4$; (b) δ_x/δ^* at $y^+ = 150$; (c) δ_z/δ^* at $y^+ = 4$; (d) δ_z/δ^* at $y^+ = 150$. —, Streamwise velocity component; ----, wall-normal velocity component; - · -, spanwise velocity component.

The periodic domain size of the current simulation was selected to ensure that the streamwise and spanwise two-point correlations are nearly zero for large separations, where the two-point correlation for the velocity component u_i is $Q_{u_i u_i}$. As is evident in figure 2, the near-wall correlations are indeed near zero for large separations, though they could be better for the streamwise component. However, far from the wall ($y^+ = 150$) low-level large-scale coherence is evident in the correlation, perhaps due to acoustics as suggested by Coleman, Kim & Moser (1995).

In the wall-normal direction, the B-splines were defined on a non-uniform set of knots (grid points) which is given by

$$t_i = (\Delta y_{\max} - \Delta y_{\min}) \left[\frac{i N_m}{N_k} + (e^{-\alpha i N_m / N_k} - 1) / \alpha \right] + \frac{\Delta y_{\min} i N_m}{N_k}, \quad (2.2)$$

where $\alpha = 0.14$, $N_m = 1.09$, $N_k = 207$, $\Delta y_{\min} = 1.0$, and $\Delta y_{\max} = 110.0$. With this distribution there were 13 grid points in the first 9 wall units, including the grid point at the wall. The minimum grid spacing in the wall-normal direction was 0.48^+ wall units while the maximum was 7.8^+ wall units at the free-stream boundary, which was located at $y^+ = 875$.

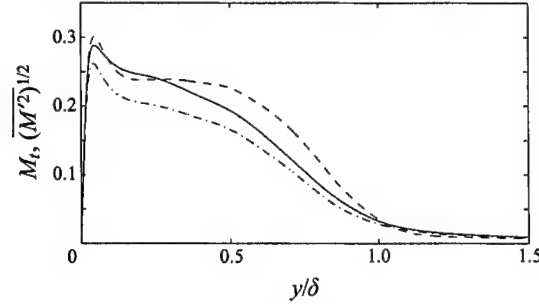


FIGURE 3. Turbulent and fluctuating Mach numbers as functions of y/δ : —, turbulent Mach number, M_t ; ----, RMS of Mach number fluctuations, $(\overline{M'^2})^{1/2}$; - · -, turbulent Mach number with spanwise component removed.

2.3. A note on averaging

In the results that follow, both Reynolds and Favre averaging are used depending on simplicity of presentation and conventions used in the papers to which we are comparing. In each case care will be taken to distinguish between the two.

The Reynolds average of f over the x - and z -directions will be denoted by \bar{f} , and fluctuations about this mean will be denoted by f' . The Favre average over the x - and z -directions, \tilde{f} , is a density-weighted average:

$$\tilde{f} = \frac{\overline{\rho f}}{\bar{\rho}}. \quad (2.3)$$

Fluctuations about the Favre average will be denoted by f'' .

2.4. The turbulent Mach number

One convenient measure of the turbulent compressibility effects is the fluctuating Mach number, M' , which is just the RMS fluctuation of the Mach number. A similar quantity is the turbulent Mach number given by

$$M_t = \frac{(\overline{u'_i u'_i})^{1/2}}{\bar{a}}. \quad (2.4)$$

Morkovin (1962) suggests that the turbulence is only weakly affected by compressibility provided $M' \lesssim 0.2$ (0.3 according to Spina *et al.* 1994). Despite the relatively low Mach number, the peak values of M' and M_t in the simulation are approximately 0.3 (figure 3). Nevertheless, as will be shown in § 3, Morkovin's density scaling and the Van Driest transformation still apply. The shoulder in figure 3 is at $(\overline{M'^2})^{1/2} \approx 0.25$, while the experimental data shown in Spina *et al.* (1994), for $M_\infty = 2.3$ and $Re_\theta = 4700$, have a shoulder at $(\overline{M'^2})^{1/2} \approx 0.20$. The reason for the difference is most likely the neglect, in the experiments, of the spanwise velocity in calculating the Mach number. As one can see in figure 3, the turbulent Mach number is consistent with the experimental value of 0.2 when the spanwise velocity component is not included.

A measure of intrinsic compressibility is the ratio of mean-square dilatation fluctuations to mean-square vorticity fluctuations:

$$\overline{(\partial u'_i / \partial x_i)(\partial u'_j / \partial x_j)} / \overline{\omega'_k \omega'_k}. \quad (2.5)$$

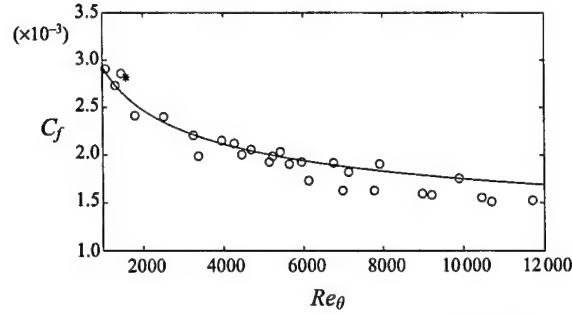


FIGURE 4. Comparison of the computational C_f with the experimental data of Coles (1954): *, simulation data point; \circ , experimental data points ($2.2 \leq M \leq 2.8$); —, Van Driest II (Bardina *et al.* 1997).

This ratio measures the level of compressibility, as given by dilatation, relative to the turbulent motion, as given by enstrophy. In the simulation we find that this ratio is approximately 5×10^{-4} throughout the boundary layer.

3. Turbulence statistics

In this section, several turbulence statistics are examined to evaluate their consistency with accepted experimental and computational results.

To obtain statistics, averages are computed over the streamwise and spanwise directions of each field; then an ensemble average over 55 fields spanning 31.33 time units was calculated. Time is non-dimensionalized by δ^*/a_∞ . The flow was determined to be stationary when several quantities (C_f , θ , u_τ , Re_θ , and T_w) began to oscillate about a mean value.

3.1. Mean flow

The skin friction coefficient is defined as

$$C_f = 2 \left(\frac{u_\tau}{U_\infty} \right)^2 \frac{\bar{p}_w}{\bar{p}_\infty}. \quad (3.1)$$

In the simulation the skin friction coefficient was found to be $C_f \approx 0.00282$. There are very few experimental studies at the low Reynolds number of the simulation. However, the simulation compares favourably with the experimental results compiled by Coles (1954) and the skin friction correlation given in Bardina, Huang & Coakley (1997) based on the Van Driest II skin friction transformation (figure 4).

The Van Driest transformed velocity, U_c , is plotted in wall units in figure 5. U_c is defined as

$$U_c = \int_0^U (\bar{T}_w/\bar{T})^{1/2} dU. \quad (3.2)$$

Experiments have shown that U_c satisfies the same scaling laws as the mean streamwise velocity in incompressible flow. On the plot we have included the linear sub-layer relation, $U_c^+ = y^+$, the standard log-law, and a composite profile that consists of Reichardt's (1951) inner layer profile and Finley's wake function (Cebeci & Bradshaw

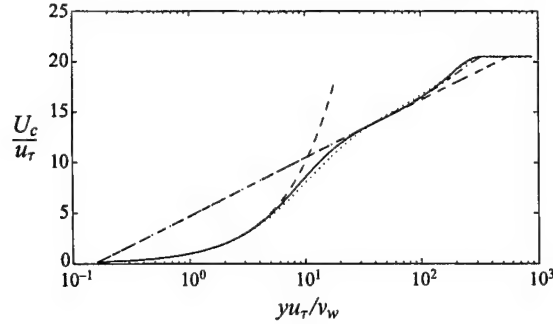


FIGURE 5. Van Driest transformed velocity in wall units: —, DNS time average; ----, linear sub-layer $U_c^+ = y^+$; - · - ·, log-law $U_c^+ = (1/0.40) \ln(yu_\tau/v_w) + 4.7$; ·····, Reichardt's profile with Finley's wake function; - - - -, Coles' profile.

1977):

$$\frac{U_c}{u_\tau} = \frac{1}{\kappa} \ln \left(1 + \kappa \frac{yu_\tau}{v_w} \right) + C_1 \left[1 - e^{-yu_\tau/(\eta_1 v_w)} - \left(\frac{yu_\tau}{\eta_1 v_w} \right) e^{-yu_\tau b/(v_w)} \right] + \frac{1}{\kappa} \left[\left(\frac{y}{\delta} \right)^2 - \left(\frac{y}{\delta} \right)^3 + 6\Pi \left(\frac{y}{\delta} \right)^2 - 4\Pi \left(\frac{y}{\delta} \right)^3 \right], \quad (3.3)$$

where δ is the y location at which $U_c(y = \delta) = U_{c\infty}$, $C_1 = -(1/\kappa) \ln(\kappa) + C$, $\eta_1 = 11$, and $b = 0.33$. This profile is used in the Appendix to calculate the slow-growth terms. In addition, the more commonly cited Coles' profile (Coles 1956) is shown. In the region of $30 \leq y^+ \leq 70$, the simulation data fall on the log-law curve, where we have chosen the constants $\kappa = 0.40$ and $C = 4.7$ for the plot; κ was determined by finding the minimum of $y^+(\partial U_c^+/\partial y^+)$ as a function of y^+ . Using this value and the location of the minimum, C was then calculated. These values compare well with those of Spalart (1988), and κ is within the range of values quoted in the literature (see Smits & Dussauge 1996). At low Reynolds numbers the log-region becomes vanishingly thin making the determination of κ and C difficult. There is also some disagreement as to whether or not the values are Reynolds number dependent at the low Reynolds number of the simulation (Spalart 1988). The value of Π for the time-averaged profile was $\Pi = 0.25$, determined from the equations in the Appendix. Reichardt's 'basic' profile with Finley's wake function gives a rather good representation of U_c throughout the boundary layer. Since this is the profile shape assumed when computing the slow streamwise derivatives (see the Appendix), the good agreement implies that the assumed profile does not introduce a significant error in the computation of these derivatives. It is interesting to note that if we use U rather than the transformed velocity U_c the values of κ and C are 0.477 and 2.64, respectively, which are quite different from the incompressible values.

3.2. RMS velocity, pressure, and vorticity

When normalized by u_τ the turbulence intensities from the current compressible boundary layer are lower than the intensities from the incompressible boundary layer (figure 6a). Morkovin (1962) predicted that scaling by the square root of the mean density profile should collapse RMS data for the streamwise velocity component and possibly the spanwise and wall-normal components. When this scaling

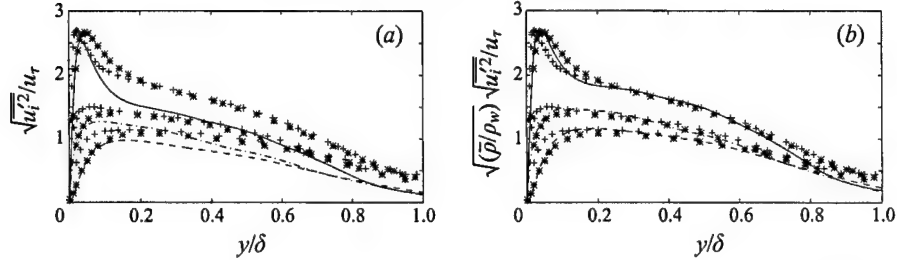


FIGURE 6. RMS velocity profiles plotted versus y/δ , (a) scaled by $1/u_\tau$, and (b) scaled by $\sqrt{(\bar{\rho}/\rho_w)}/u_\tau$. Lines correspond to the compressible simulation and symbols are used for Spalart's incompressible simulations: —, streamwise velocity component; ----, wall-normal velocity component; - · - ·, spanwise velocity component; +, Spalart ($Re_\theta = 1410$); *, Spalart ($Re_\theta = 670$).

is used there is good agreement for all three velocity components (figure 6b). In the experiments good collapse is obtained for the streamwise component but the experiments are inconclusive with respect to the collapse of the other two components (Smits & Dussauge 1996). Smits & Dussauge (1996) attribute this to both the difficulty in measuring the spanwise and wall-normal components and the scarcity of measurements of these two components.

There are two additional points which need to be mentioned in connection with figure 6. The first is that Re_θ , based on local viscosity in the compressible simulation, varies across the boundary layer from 849 to 1577. Spalart's (1988) two simulations at $Re_\theta = 670$ and 1410 span this range. This is important because in y/δ units, the location of the peaks in the intensities moves toward the wall, since it remains approximately fixed in wall units. Further, Spalart showed that at these low Reynolds numbers, the magnitude of the peaks in intensities increases with Reynolds number. The second issue concerns the choice of δ in figure 6. As discussed by Spalart, the collapse of the data over a wide range of Reynolds numbers is sensitive to the choice of δ . In making our comparison, we used a definition of δ based on the composite profile of (3.3) and made no effort to find a definition that would better collapse the data. This might account for the differences that are evident at $y \geq 0.65\delta$.

In the compressible simulation the pressure fluctuations, when scaled by $\rho_w u_\tau^2$, are larger than those found in the incompressible simulations through most of the boundary layer (figure 7). The peak pressure fluctuations are larger than Spalart's $Re_\theta = 670$ simulation and occur at nearly the same location. The value of the RMS pressure at the wall and at the peak are $(p'_{rms})_w/(\rho_w u_\tau^2) \approx 2.7$ and $(p'_{rms})_{max}/(\rho_w u_\tau^2) \approx 3.0$, respectively. In the free stream the pressure fluctuations approach $(p'_{rms})_\infty/(\rho_w u_\tau^2) \approx 0.47$. This is comparable to the value of the radiated pressure measured by Laufer (1964) of $(p'_{rms})_\infty/(\rho_w u_\tau^2) \approx 0.4$.

RMS vorticity profiles for the present simulation agree very well with those found in Spalart's incompressible simulations when normalized by u_τ^2/ν_w (figure 8) and plotted in wall units, with the compressible results being slightly larger than the incompressible simulations away from the wall. Note that from Spalart's data it is clear that near the wall the maximum may be Reynolds number dependent. The near-wall RMS vorticity is shown plotted in wall units here because the wall scaling is known to (approximately) collapse such profiles for different Reynolds numbers in incompressible flows, and indeed in y/δ units our data did not collapse with that of Spalart's.

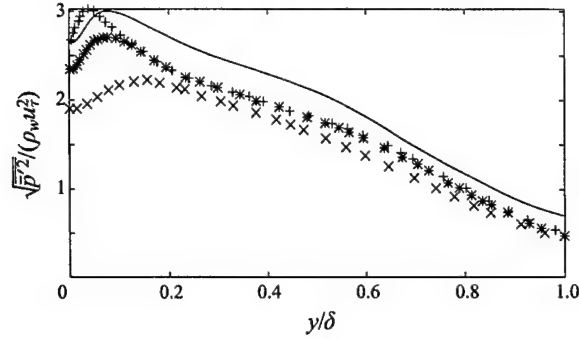


FIGURE 7. RMS pressure fluctuations versus y/δ : —, compressible DNS; +, Spalart ($Re_\theta = 1410$); *, Spalart ($Re_\theta = 670$); x, Spalart ($Re_\theta = 300$).

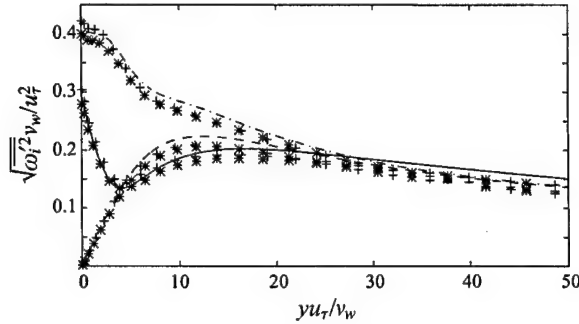


FIGURE 8. RMS of vorticity fluctuations. Lines correspond to the compressible simulation: —, $\overline{\omega_1'^2}$; ---, $\overline{\omega_2'^2}$; - · -, $\overline{\omega_3'^2}$; +, Spalart ($Re_\theta = 1410$); *, Spalart ($Re_\theta = 670$).

3.3. Reynolds shear stress

Reynolds averaging the momentum equation,

$$\frac{\partial \rho u_i}{\partial t} = -\frac{\partial}{\partial x_j} \{ \rho u_i u_j \} - \frac{\partial p}{\partial x_i} + \frac{1}{Re} \frac{\partial \tau_{ij}}{\partial x_j}, \quad (3.4)$$

we get

$$\frac{\partial \bar{\rho} \bar{u}_i}{\partial t} = -\frac{\partial}{\partial x_j} \{ \bar{\rho} \bar{u}_i \bar{u}_j + \overline{\rho u_i' u_j'} \} - \frac{\partial \bar{p}}{\partial x_i} + \frac{1}{Re} \frac{\partial \bar{\tau}_{ij}}{\partial x_j}. \quad (3.5)$$

The sum of the Reynolds shear stress and mean shear stress terms is

$$\frac{\partial}{\partial x_2} \left\{ -\overline{\rho u_1' u_2'} + \frac{1}{Re} \left[\bar{\mu} \frac{\partial \bar{u}_1}{\partial x_2} + \mu' \left(\frac{\partial u_1'}{\partial x_2} + \frac{\partial u_2'}{\partial x_1} \right) \right] \right\}. \quad (3.6)$$

In incompressible boundary layers a constant total stress region is observed near the wall. The constant-stress region is consistent with the law of the wall and is also present in the current simulation (figure 9). The constant-stress region extends to 30 or 40 wall units above the wall.

As was the case for the turbulence intensities, $\overline{u'v'}$ agrees with the incompressible

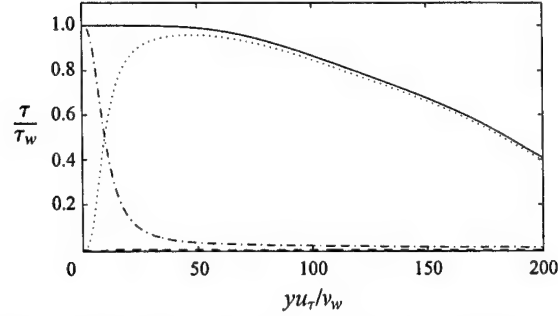


FIGURE 9. Simulation results for Reynolds stress, mean shear stress, and total stress versus yu_τ/v_w : —, total shear stress; ·····, Reynolds stress ($\rho u'_1 u'_2$); —·—, mean shear stress ($\mu(\partial u/\partial y)$); ----, stress correlations ($\mu'[(\partial u'/\partial y) + (\partial v'/\partial x)]$).

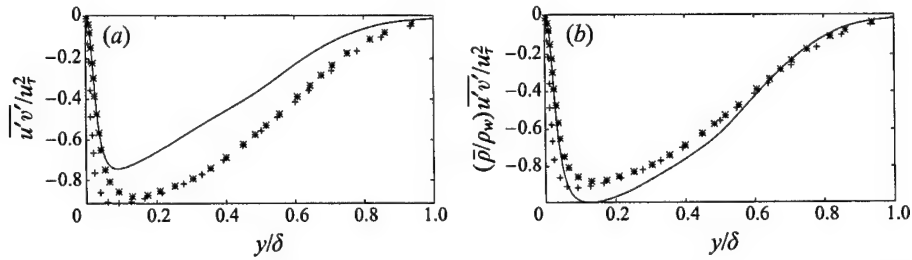


FIGURE 10. $\overline{u'v'}$ versus y/δ , (a) scaled by $1/u_\tau^2$, and (b) scaled by $(\bar{\rho}/\rho_w)/u_\tau^2$: —, compressible DNS; +, Spalart ($Re_\theta = 1410$); *, Spalart ($Re_\theta = 670$).

results when scaled by the local mean density (figure 10). This agreement is not as close as for the intensities, but this is primarily due to the square root in the definition of the intensities.

4. Reynolds analogies

For incompressible laminar boundary layers, the similarity of the momentum and energy equations allows one to approximately relate quantities pertaining to heat transfer with quantities pertaining to momentum transfer. O. Reynolds discovered this principle in its simplest form. The 'Reynolds analogy' has been extended with additional approximations to the compressible and turbulent cases. Morkovin (1962) suggests that a Reynolds analogy might apply to compressible turbulence, a concept known as the 'strong Reynolds analogy (SRA)'. More recently, other expressions of a Reynolds analogy have been formulated by several authors (Gaviglio 1987 and Huang, Coleman & Bradshaw 1995), and these will also be studied below.

4.1. The strong Reynolds analogy

To investigate the validity of the strong Reynolds analogy, and its consequences, a brief review of its derivation and a critical examination of the underlying assumptions are given in this section. The analogy is based on the observation that the transport equations for mean velocity and mean total enthalpy, $h_t = C_p T + u_i^2/2$, for a stationary,

zero-pressure-gradient boundary layer,

$$\bar{\rho}\tilde{u}_1\frac{\partial\tilde{u}_1}{\partial x_1} + \bar{\rho}\tilde{u}_2\frac{\partial\tilde{u}_1}{\partial x_2} = \frac{\partial}{\partial x_2} \left\{ \bar{\mu}\frac{\partial\tilde{u}_1}{\partial x_2} - \overline{\rho u_1'' u_2''} \right\}, \quad (4.1a)$$

$$\bar{\rho}\tilde{u}_1\frac{\partial\tilde{h}_t}{\partial x_1} + \bar{\rho}\tilde{u}_2\frac{\partial\tilde{h}_t}{\partial x_2} = \frac{\partial}{\partial x_2} \left\{ \frac{\bar{\mu}}{Pr}\frac{\partial\tilde{h}_t}{\partial x_2} - \overline{\rho u_2'' h_t''} \right\}, \quad (4.1b)$$

have the same form if the Prandtl number is 1. If the Prandtl numbers are different, the equations are still of the same form provided the molecular diffusivity can be neglected, which is true in a turbulent boundary layer, except very near the wall. The two equations, however, have different boundary conditions.

The total temperature, T_t , is defined by the relationship $h_t = C_p T_t$. If one assumes that gradients of mean total temperature and velocity in x can be neglected and further (without justification) that

$$T_t'' = C u_1'', \quad (4.2)$$

one can eliminate the turbulent terms in the mean transport equations and solve for \tilde{T}_t in terms of \tilde{u}_1 ,

$$\tilde{T}_t = C \tilde{u}_1 + D. \quad (4.3)$$

This result was first stated in a slightly different form by Young (1953)[†] and later by Morkovin (1962), who called assumption (4.2) the strong Reynolds analogy. Since $\partial\tilde{T}_t/\partial y = 0$ at an adiabatic wall and the velocity gradient, $\partial\tilde{u}_1/\partial y$, is non-zero at the wall, it follows that the constant, C , must be zero. This implies that the mean total temperature is constant with value \tilde{T}_{tw} and the total temperature fluctuations are zero. In the current simulation the maximum deviation of the mean total temperature from a constant is about 7%, thus approximately verifying the result for the mean. However, in the simulation, RMS total temperature fluctuations are comparable in magnitude to the static temperature fluctuations (see figure 11), and are thus not negligible. The discussion that follows addresses the validity of (4.2), with $C = 0$, and the relationships derived from it.

The fact that measured total temperature fluctuations are not negligible was recognized by Morkovin (1962). Nonetheless, relations derived assuming that they are negligible have been widely used in the literature. These relations can be obtained by writing the definition of total temperature and subtracting its Favre mean:

$$C_p T_t'' = C_p T'' + \tilde{u}_1 u_1'' + \frac{u_1'' u_1''}{2} - \frac{\widetilde{u_1'' u_1''}}{2}. \quad (4.4)$$

By retaining only the terms that are linear in the fluctuations, and assuming that $\tilde{u}_1 u_1'' \gg \tilde{u}_2 u_2''$ and $\tilde{u}_1 u_1'' \gg \tilde{u}_3 u_3''$, we get

$$C_p T_t'' = C_p T'' + \tilde{u}_1 u_1''. \quad (4.5)$$

So far, the approximations made are excellent. One can verify this by considering the correlation coefficient $R_{u_1''(T_t'' - T'')}$ between streamwise velocity fluctuations and the difference between total and static temperature fluctuations. The correlation coefficient differs from unity by less than 0.9% for $y/\delta > 0.05$, showing that (4.5) is very accurate.

In Morkovin's analysis, the SRA is invoked to argue that the total temperature

[†] Young calls (4.3) and (4.2) solutions to the equations. This terminology is imprecise and attaches too much legitimacy to (4.3) and (4.2). We prefer not to identify the two as solutions, but rather to say that the assumption (4.2) implies (4.3).

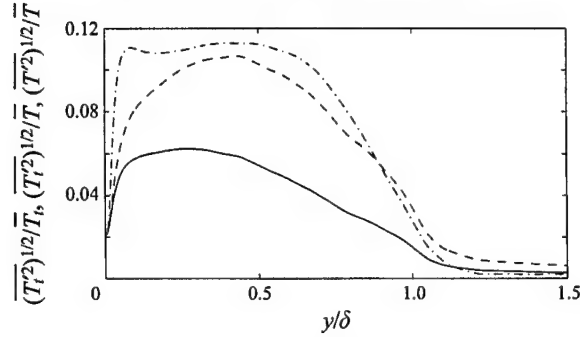


FIGURE 11. Comparison of RMS total and static temperature fluctuations: —, $(T_t'')^{1/2}/T_t$; ----, $(T_t'^2)^{1/2}/T$; — · —, $(T''^2)^{1/2}/T$.

fluctuations are negligible compared to the static temperature fluctuations, and thus (4.5) becomes

$$C_p T'' + \tilde{u}_1 u_1'' \approx 0, \quad (4.6)$$

which is not valid, as discussed above (figure 11). Substituting $\gamma R/(\gamma - 1)$ for C_p and defining the Mach number, M_a :

$$M_a^2 = \frac{\tilde{u}_1^2}{\gamma R \tilde{T}}, \quad (4.7)$$

(4.6) can be rewritten:

$$\frac{T''}{\tilde{T}} = -(\gamma - 1) M_a^2 \frac{u_1''}{\tilde{u}_1}. \quad (4.8)$$

The (questionable) relations, (4.6) and (4.8), between T'' and u_1'' have several statistical consequences which are given by

$$\frac{(\overline{T''^2})^{1/2}/\tilde{T}}{(\gamma - 1) M_a^2 (\overline{u_1''^2})^{1/2}/\tilde{u}_1} \approx 1, \quad (4.9a)$$

$$-R_{u_1'' T''} \approx 1, \quad (4.9b)$$

$$Pr_t = \frac{\overline{\rho u_1'' u_2''} (\partial \tilde{T} / \partial y)}{\overline{\rho u_2'' T''} (\partial \tilde{u}_1 / \partial y)} \approx 1. \quad (4.9c)$$

These are three of the five SRA relationships Morkovin (1962) presented. Equations (4.9a) and (4.9b) are direct consequences of (4.6), whereas (4.9c) is obtained by multiplying (4.6) by $\rho u_2''$, averaging, and assuming that

$$\tilde{u}_1 = -C_p \left(\frac{\partial \tilde{T}}{\partial y} \right) / \left(\frac{\partial \tilde{u}_1}{\partial y} \right), \quad (4.10)$$

which comes from the mean total temperature equation when it is assumed that \tilde{T}_t is constant and that nonlinear fluctuating terms and velocity components other than \tilde{u}_1 are small.

From the simulation results we see that equation (4.9a) is satisfied for $y/\delta < 0.6$ (figure 12). However, in the same region, (4.9b) and (4.9c) are not satisfied (see figures 13 and 14). The correlation $R_{u_1'' T''}$ is approximately 0.6 through most of the boundary

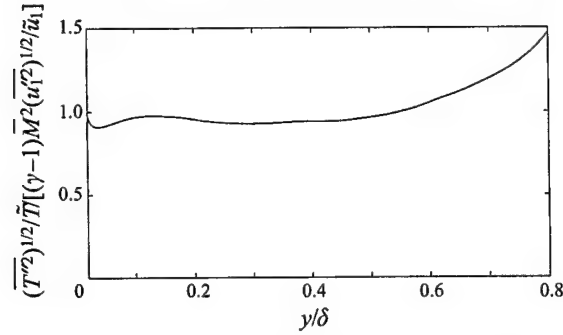


FIGURE 12. Test of the strong Reynolds analogy, as expressed by (4.9a).

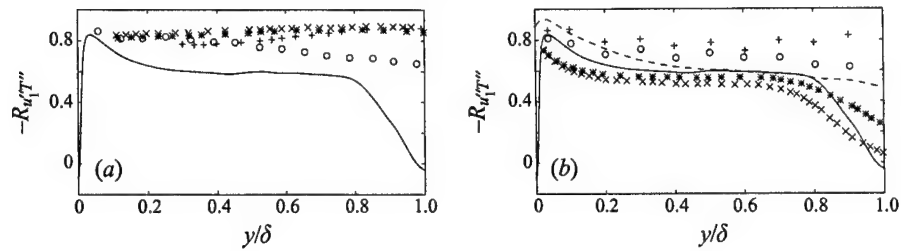


FIGURE 13. Correlation coefficient, $-R_{u_i''T''}$, versus y/δ . (a) Comparison with compressible experiments: —, time average of DNS; x, Debieve ($M = 2.3$, $Re_\theta = 5650$) (Gaviglio 1987); *, Debieve ($M = 2.3$, $Re_\theta = 5650$) (Gaviglio 1987); +, Dussauge ($M = 1.7$, $Re_\theta = 5700$) (Gaviglio 1987); o, Smith & Smits (1993) ($M = 2.9$, $Re_\theta = 77\,600$). (b) Comparison with incompressible experiments: —, time average of DNS; x, Fulachier ($Re_\theta = 5000$) (Gaviglio 1987); *, Rey (Gaviglio 1987); +, Subramanian & Antonia (1981) $Re_\theta = 990$; o, Subramanian & Antonia (1981) $Re_\theta = 7100$; ----, incompressible simulation of Bell & Ferziger (1993).

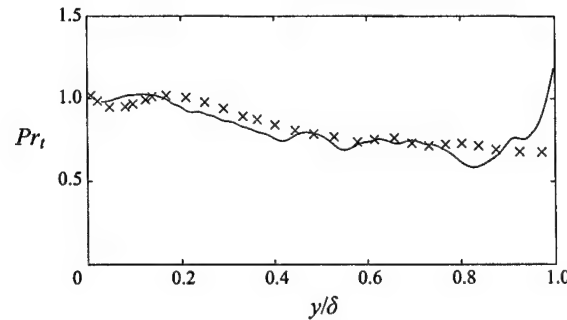


FIGURE 14. Turbulent Prandtl number, Pr_t , versus y/δ : —, time average DNS data; x, incompressible heated wall simulations of Bell & Ferziger (1993).

layer, and the turbulent Prandtl number is about 0.7 except near the wall ($y/\delta < 0.2$) where it is near 1. The current results for the velocity-temperature correlation are in disagreement with the available data from compressible boundary layer experiments (figure 13), which show the correlation to be close to 1 (approximately 0.9), in agreement with predictions of the SRA.

The reason for this disagreement between simulations and experiments is not clear, but is of great interest. The speculations of Gaviglio (1987) that the large correlation values observed in experiments are due to acoustic waves suggests the possibility that the acoustics are somehow different (weaker) in the simulations. However, tests for numerical artifacts (e.g. damping) in the simulated acoustics did not reveal any problems, and our radiated sound pressure magnitude compares well with that of Laufer (1964). Another interesting observation is that in the current simulations both the velocity-temperature correlations and the turbulent Prandtl number agree reasonably well with data from incompressible boundary layers, both experimental and computational (see figures 13*b* and 14). This might be expected, given the weak compressibility of the boundary layer at this Mach number. This agreement at least makes plausible the proposition that the current simulation results are physical, despite disagreement with compressible experiments. The basis for comparison with the incompressible heated wall in figure 13(*b*) is that the heated wall produces a temperature gradient of the same sign as that obtained in the current simulation.

Further analysis suggests that the key to the discrepancy is the magnitude of the total temperature fluctuations. In the experiments, it is total temperature and momentum that are measured directly, with other quantities computed using several approximate relations. By using these relations in the simulation data it was found that (a) they yield accurate values for the derived quantities; and (b) when the total temperature fluctuations in the simulations are reduced by a factor of 2, the relations used in the experiments yield correlations $R_{u''T''}$ consistent with the experiments. The total temperature fluctuations in the experiments are indeed approximately a factor of 2 lower than the simulations (Kistler 1959). A factor of 2 error in the total temperature is much larger than the uncertainties in either the experiments or the simulation, so there is clearly something wrong with one or the other (or both). A potentially useful approach to settling this question would be to use a physical model of the experimental probes in the simulations, and process the resulting signals as is done in the experiments, to see if results consistent with the experiments are recovered. Until this issue is resolved, it would be wise to view both the experimental and computational results on these quantities with some suspicion.

Of the three relations shown, only the RMS relation (4.9*a*) is very nearly satisfied. The question arises as to how this relationship can be satisfied even though total temperature fluctuations are of the same order as temperature fluctuations. This success of (4.9*a*) can be explained by rearranging the definition of total temperature fluctuations (4.5) as follows:

$$\frac{\overline{T''^2} + \overline{T_t''^2} - 2\overline{T_t''T''}}{\tilde{T}^2} = (\gamma - 1)^2 M_a^4 \frac{\overline{u_1''^2}}{\tilde{u}_1^2}. \quad (4.11)$$

The condition that must be satisfied for (4.9*a*) to be valid when total temperature fluctuations are not neglected is

$$\frac{\overline{T''^2}}{\tilde{T}^2} \gg \frac{\overline{T_t''^2} - 2\overline{T_t''T''}}{\tilde{T}^2}, \quad (4.12)$$

which the simulation data confirms (figure 15). While all the terms on the left-hand side of (4.11) are of the same order, in the inner portion of the boundary layer the term on the left-hand side of (4.12) is nearly a factor of 6 greater than the term on the right. So the success of (4.9*a*) is due to a relationship between total and static

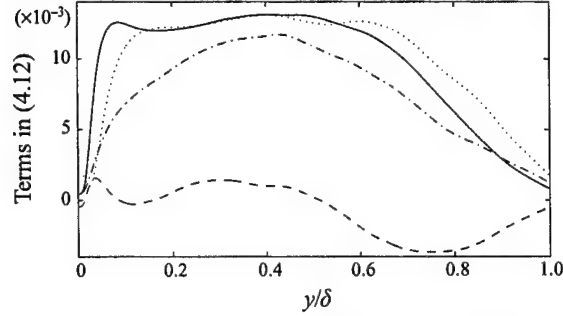


FIGURE 15. Comparison of terms in (4.12): —, $\overline{T''^2}/\bar{T}^2$; ---, $\overline{T_i''^2}/\bar{T}^2$; ·····, $-2\overline{T_i''T''}/\bar{T}^2$; - · - ·, $(\overline{T_i''^2} - 2\overline{T_i''T''})/\bar{T}^2$.

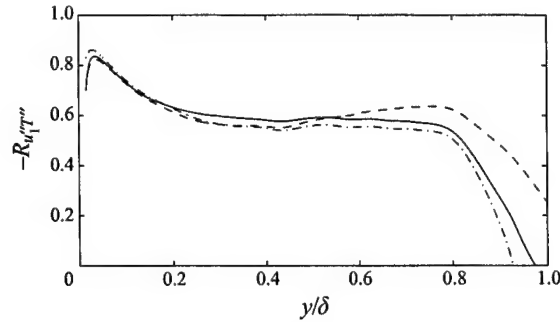


FIGURE 16. Comparison of $R_{u_i''T''}$ from (4.15) to simulation data: —, time average of DNS data; ----, profile predicted by (4.15); — · —, profile predicted by the modified Reynolds analogy of Huang *et al.* (1995).

temperature fluctuations rather than the assumption of negligible total temperature fluctuations.

Gaviglio (1987) has shown that fluctuations in total and static temperature can be directly related to the correlation coefficient $R_{u_i''T''}$ if (4.9a) is assumed to be valid. The RMS of the linearized definition of total temperature, (4.5), is

$$(\overline{T_t''^2})^{1/2} = \left(\overline{T''^2} + \frac{\tilde{u}_1^2}{C_p^2} \overline{u_1''^2} + 2 \frac{\tilde{u}_1}{C_p} (\overline{T''^2})^{1/2} (\overline{u_1''^2})^{1/2} R_{u_i''T''} \right)^{1/2}, \quad (4.13)$$

where the last term was written in terms of $R_{u_i''T''}$. Now if we say that (4.9a),

$$(\overline{T''^2})^{1/2} = \frac{\tilde{u}_1}{C_p} (\overline{u_1''^2})^{1/2}, \quad (4.14)$$

is empirically valid then (4.13) becomes

$$R_{u_i''T''} = \frac{\overline{T_i''^2}}{2\overline{T''^2}} - 1. \quad (4.15)$$

As expected in the case of negligible total temperature fluctuations this equation reduces to $R_{u_i''T''} = -1$. The value of $R_{u_i''T''}$ predicted by (4.15) agrees well with the actual values (figure 16).

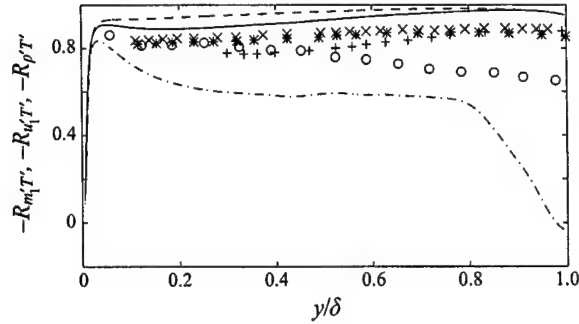


FIGURE 17. Comparison of $-R_{m_i T'}$, $-R_{u_i T'}$, and $-R_{p T'}$ versus y/δ : —, $-R_{m_i T'}$; ---, $-R_{p T'}$; — · —, $-R_{u_i T'}$; symbols showing the experimental results for $-R_{u_i T'}$ are the same as in figure 13a.

Since for incompressible flow $-R_{u_i T'}$ is significantly less than unity, the correlation coefficient between streamwise momentum fluctuations and temperature fluctuations, $-R_{m_i T'}$, will also be much less than unity for incompressible flow (the two are in fact equal). For the compressible simulation, however, $-R_{m_i T'}$ is much closer to 1 (figure 17). This is because $-R_{m_i T'}$ is a weighted average of $R_{u_i T'}$ and $R_{p T'}$, and $R_{p T'}$ is very close to 1 (dashed curve in figure 17) since pressure fluctuations may be assumed to be small compared to density and temperature fluctuations in the equation of state (Lele 1994). The contribution of $R_{p T'}$ to the weighted average pushes $-R_{m_i T'}$ towards unity. The close correlation between streamwise momentum and temperature fluctuations may indicate a greater similarity between the transport equations for turbulent momentum and heat transport than in the incompressible case, which may be due to a reduction in the importance of the pressure gradient term.

4.2. 'Modified Reynolds analogies'

Both Gaviglio (1987) and Huang *et al.* (1995) point out that for flows with non-adiabatic boundaries the agreement between (4.9a) and measurements is poor. Both authors propose new relationships between temperature and velocity fluctuations which have been called 'modified' Reynolds analogies. Since the agreement of this relation with the current adiabatic wall simulations is not perfect either, we now assess these modified Reynolds analogies. The modified Reynolds analogies of Rubesin (1990), Gaviglio (1987) (GSRA), and Huang *et al.* (1995) (HSRA) all have the form

$$\frac{(\overline{T'^2})^{1/2}/\tilde{T}}{(\gamma - 1)\tilde{M}^2(\overline{u'^2})^{1/2}/\tilde{u}_1} \approx \frac{1}{c(1 - a(\partial\tilde{T}/\partial\tilde{T}))}. \quad (4.16)$$

If $a = 0$ and $c = 1$ then the standard SRA is obtained. For all the modified expressions $a = 1$. Rubesin used $c = 1.34$. Gaviglio and Huang *et al.* use the mixing length hypothesis to obtain $c = 1.0$ and $c = Pr_t$, respectively. The difference between the derivation of Gaviglio and Huang *et al.* is that Gaviglio assumes that the mixing lengths for temperature and velocity fluctuations are equal. In figure 18 the ratio of the left-hand side of (4.16) to the right-hand side is plotted for the SRA, GSRA, and HSRA. The version presented by Huang *et al.* (1995) is in excellent agreement with the data throughout the boundary layer. The value of $R_{u_i T'}$ that is predicted by the modified analogy of Huang *et al.* can be derived by substituting equation (4.16), with

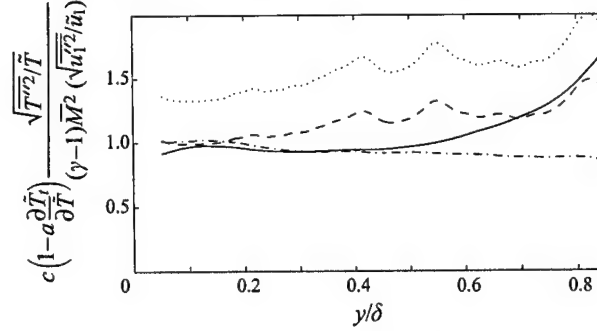


FIGURE 18. Plot of the Strong Reynolds analogy, and the modified Reynolds analogies of Gaviglio (1987) and Huang *et al.* (1995): —, SRA; ----, GSRA; - · - ·, HSRA; · · · · ·, Rubesin.

$c = Pr_t$, into (4.13) to obtain

$$\frac{[\overline{T_t''^2}/\overline{T''^2} - 1]}{[2Pr_t(1 - \partial\tilde{T}_t/\partial\tilde{T})]} - \frac{Pr_t}{2} \left(1 - \frac{\partial\tilde{T}_t}{\partial\tilde{T}}\right) = 1 + R_{u_1''T''}. \quad (4.17)$$

The profile for $R_{u_1''T''}$ predicted by (4.17) agrees well with the simulation data (figure 16).

Why does the expression of Huang *et al.* work so well? Substituting the definition of the turbulent Prandtl number, (4.9c), and the derivative of the total temperature,

$$\frac{\partial\tilde{T}_t}{\partial y} = \frac{\partial\tilde{T}}{\partial y} + \frac{\tilde{u}_1}{C_p} \frac{\partial\tilde{u}_1}{\partial y}, \quad (4.18)$$

into (4.16), with $c = Pr_t$, we obtain

$$\frac{\overline{\rho u_2'' T''}}{(\overline{T''^2})^{1/2}} = -\frac{\overline{\rho u_2'' u_1''}}{(\overline{u_1''^2})^{1/2}}. \quad (4.19)$$

This relationship expresses an analogy between the rates of turbulent heat and momentum transfer normalized by the property that is transported. We may divide through by the RMS of the wall-normal velocity fluctuations to obtain a relationship between the correlation coefficients $R_{u_2''T''}$ and $R_{u_1''u_2''}$:

$$R_{u_2''T''} = -R_{u_1''u_2''}, \quad (4.20)$$

where it is assumed that the correlations $\overline{\rho' u_2'' u_1''}$ and $\overline{\rho' u_2'' T''}$ are small compared to $\overline{\rho u_2'' u_1''}$ and $\overline{\rho u_2'' T''}$. The simulation results indicate that the two correlation coefficients are very nearly equal throughout the boundary layer (figure 19).

4.3. Turbulent Prandtl number

Morkovin was aware that total temperature fluctuations are not negligible compared to temperature fluctuations and stated that another set of expressions could be developed by assuming that $\overline{\rho u_2'' T_t''}$ is much smaller than $\overline{\rho u_2'' T''}$. In the lower half of the boundary layer ($y/\delta < 0.5$) this is a good assumption (figure 20).

Using this assumption, an expression can be developed for the turbulent Prandtl number. Multiplying (4.5) by $\rho u_2''$ and averaging gives

$$\overline{\rho u_2'' T_t''} = \overline{\rho u_2'' T''} + \frac{\tilde{u}_1}{C_p} \overline{\rho u_2'' u_1''}. \quad (4.21)$$

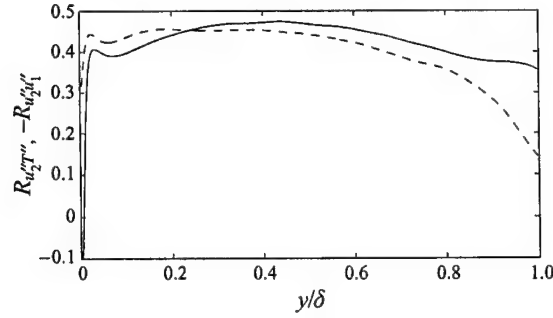


FIGURE 19. Comparison of $R_{u_2''T''}$ and $-R_{u_2''u_1''}$ versus y/δ : —, $R_{u_2''T''}$; ---, $-R_{u_2''u_1''}$.

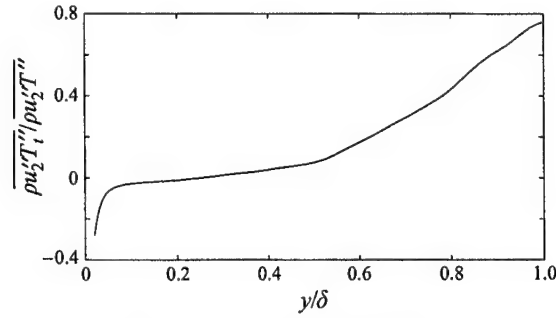


FIGURE 20. Plot of the ratio $\overline{\rho u_2''T''}/\overline{\rho u_1''T''}$ versus y/δ .

Neglecting $\overline{\rho u_2''T''}$ relative to $\overline{\rho u_2''T''}$ yields

$$\frac{\overline{\rho u_2''u_1''}}{\overline{\rho u_2''T''}} = -\frac{C_p}{\tilde{u}_1}. \quad (4.22)$$

Substituting (4.18) into (4.22) gives

$$Pr_t = \frac{\overline{\rho u_2''u_1''}}{\overline{\rho u_2''T''}} \frac{(\partial \tilde{T}/\partial y)}{(\partial \tilde{u}_1/\partial y)} = \frac{\partial \tilde{T}}{\partial y} \left(\frac{\partial \tilde{T}}{\partial y} - \frac{\partial \tilde{T}_t}{\partial y} \right)^{-1}. \quad (4.23)$$

This prediction agrees with the simulation data in the inner portion of the boundary layer, but as the boundary layer edge is approached the agreement becomes poor (figure 21).

5. Turbulent kinetic energy budget

For the benefit of those formulating turbulence models, the budgets for both the Reynolds stresses and the turbulent kinetic energy have been calculated. In this section, the turbulent kinetic energy budget is presented and compared with the incompressible simulations of Spalart (1988). The Reynolds stress budgets are presented in Guarini (1998). Favre averages are used in the analysis to simplify the resulting equations.

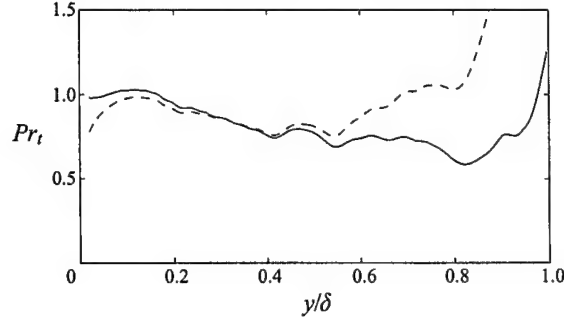


FIGURE 21. Turbulent Prandtl number Pr_t vs. y/δ : —, time average DNS data; ----, Pr_t from (4.23).

The turbulent kinetic energy is defined as:

$$\bar{k} = \frac{1}{2} \frac{\overline{\rho u_i'' u_i''}}{\bar{\rho}}, \quad (5.1)$$

and the turbulent kinetic energy equation is, after assuming homogeneity in the x - and z -directions, given by

$$\frac{\partial}{\partial t}(\bar{\rho}\bar{k}) + \bar{u}_2 \frac{\partial}{\partial x_2}(\bar{\rho}\bar{k}) = P + T + \Pi + D - \phi + V_c. \quad (5.2)$$

The symbols are defined as

$$P = -\overline{\rho u_i'' u_2''} \frac{\partial \bar{u}_i}{\partial x_2}, \quad (5.3a)$$

$$T = -\frac{1}{2} \frac{\partial}{\partial x_2} \overline{\rho u_i'' u_i'' u_2''}, \quad (5.3b)$$

$$\Pi = \Pi_t + \Pi_d = -\frac{\partial}{\partial x_2} (\overline{u_2'' p'}) + \overline{p' \frac{\partial u_i''}{\partial x_i}}, \quad (5.3c)$$

$$D = \frac{\partial}{\partial x_2} \frac{\overline{u_i''}}{Re} \tau'_{i2}, \quad (5.3d)$$

$$\phi = \frac{\overline{\tau'_{ii}}}{Re} \frac{\partial \bar{u}_i''}{\partial x_i}, \quad (5.3e)$$

$$V_c = -\overline{u_2''} \frac{\partial \bar{p}}{\partial x_2} + \overline{u_i''} \frac{\partial \bar{\tau}_{ii}}{\partial x_i} - \bar{\rho}\bar{k} \frac{\partial \bar{u}_2}{\partial x_2}. \quad (5.3f)$$

The terms in (5.2) can be interpreted as follows: the left-hand side is the substantial derivative of the turbulent kinetic energy along a mean streamline; P is the rate of generation of turbulent kinetic energy by mean velocity gradients; T is turbulent transport; Π are the pressure terms (pressure diffusion and pressure dilatation, respectively); D is viscous diffusion; $-\phi$ is viscous dissipation per unit volume; and finally, V_c includes the terms that arise when the density is not constant. The first two terms of V_c are due to the difference between the Favre and Reynolds average and the last term is the production term due to dilatation. The pressure dilatation as well as the dilatational dissipation, which are not included in V_c , are also due

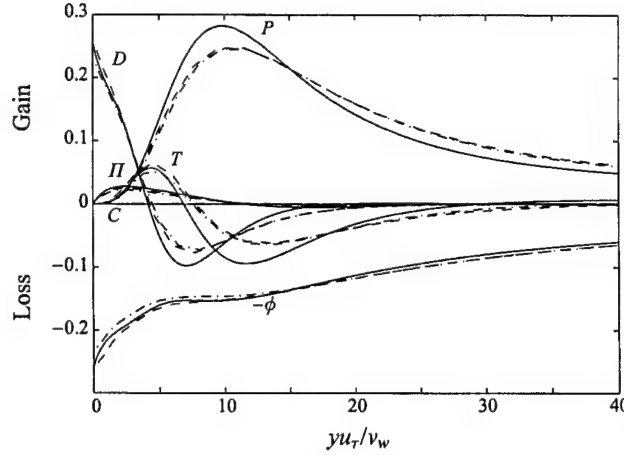


FIGURE 22. Turbulent kinetic energy budget: —, simulation data; ----, Spalart's data $Re_\theta = 1410$; — · —, Spalart's data $Re_\theta = 670$. Symbols are: C, Convective term; P, Generation term; T, Turbulent transport; Π , Pressure terms; D, Viscous transport; $-\phi$, Viscous dissipation.

to non-constant density. In the literature the dissipation per unit mass is commonly referred to as ϵ . Here we use the dissipation per unit volume, which we denote as ϕ for clarity. The dissipation and pressure terms are in a form similar to that given in Huang *et al.* (1995). The compressible turbulent kinetic energy budget agrees with the incompressible results of Spalart at two different Reynolds numbers (figure 22). The generation term is larger than in the incompressible simulation, and the viscous transport and turbulent transport terms are also greater in magnitude than in the incompressible simulation. V_c is small and has not been included on the plot for clarity. Its maximum value is a factor of 25 smaller than that of the generation term.

The effects of compressibility on the dissipation have been of interest in the literature, especially in the context of compressible turbulence models (Zeman 1990 and Sarkar *et al.* 1991). To study dissipation in the current simulation, consider ϕ which can be expanded as

$$\phi = \frac{\bar{\mu}}{Re} \frac{\partial u'_i}{\partial x_l} \left(\frac{\partial u'_i}{\partial x_l} + \frac{\partial u'_l}{\partial x_i} - \frac{2}{3} \delta_{il} \frac{\partial u'_k}{\partial x_k} \right) + \frac{\mu'}{Re} \frac{\partial u'_i}{\partial x_l} \left(\frac{\partial u'_i}{\partial x_l} + \frac{\partial u'_l}{\partial x_i} - \frac{2}{3} \delta_{il} \frac{\partial u'_k}{\partial x_k} \right) + \frac{\mu'}{Re} \frac{\partial u'_i}{\partial x_l} \left(\frac{\partial \bar{u}_i}{\partial x_l} + \frac{\partial \bar{u}_l}{\partial x_i} - \frac{2}{3} \delta_{il} \frac{\partial \bar{u}_k}{\partial x_k} \right), \quad (5.4)$$

where the three terms in this expression will be referred to as ϕ_1 , ϕ_2 , and ϕ_3 , respectively. The fluctuations about the Favre average in (5.3e) have been replaced using the identity

$$\frac{\tau'_{il} \partial u'_i}{Re \partial x_l} = \frac{\tau'_{il} \partial u'_i}{Re \partial x_l}. \quad (5.5)$$

The terms, ϕ_2 and ϕ_3 , which involve viscosity fluctuations, are negligible compared to ϕ_1 in this simulation.

The first term, ϕ_1 , can be decomposed into parts that are more amenable to

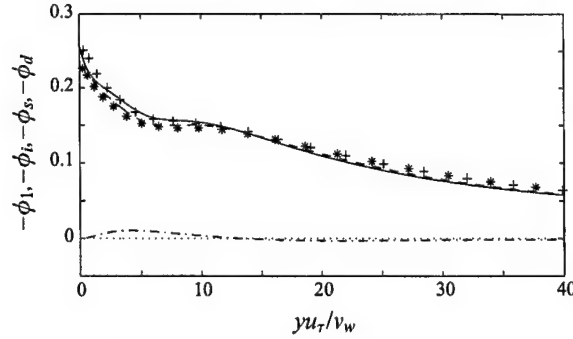


FIGURE 23. Comparison of dissipation terms: —, $-\phi_1 = -(\phi_s + \phi_i + \phi_d)$; ----, solenoidal dissipation ($-\phi_s$); — · —, dissipation due to inhomogeneity ($-\phi_i$); ·····, dissipation due to dilatation $-\phi_d$; +, Spalart's data $Re_\theta = 1410$; *, Spalart's data $Re_\theta = 670$.

comparison with incompressible flows by expressing velocity gradients in terms of the rate-of-deformation tensor, S'_{ij} , and spin tensor, Ω'_{ij} , which is related to the vorticity through $\Omega'_{ij}\Omega'_{ij} = \omega'_i\omega'_i/2$. Simplifying gives for ϕ_1 :

$$\phi_1 = \frac{\bar{\mu}}{Re} \overline{\omega'_i\omega'_i} + 2 \frac{\bar{\mu}}{Re} \left(\frac{\partial^2}{\partial x_i \partial x_i} \overline{u'_i u'_i} - 2 \frac{\partial}{\partial x_i} \overline{u'_i \frac{\partial u'_i}{\partial x_i}} \right) + \frac{4}{3} \frac{\bar{\mu}}{Re} \frac{\partial u'_i}{\partial x_i} \frac{\partial u'_k}{\partial x_k}, \quad (5.6)$$

where the first term on the right is the homogeneous incompressible dissipation, or the solenoidal part of the dissipation, ϕ_s , the second term, ϕ_i , is due to inhomogeneity, and the third term, ϕ_d , is due to dilatation. Both the dissipation due to dilatation and inhomogeneity are very small compared to the solenoidal dissipation (figure 23). At the wall the dissipation due to inhomogeneity provides a very slight contribution to the total dissipation. The compressible result agrees well with the incompressible results of Spalart.

Finally, we consider the pressure terms. There are three: pressure diffusion (Π_t), pressure dilatation (Π_d), and compressibility (Π_c). The pressure dilatation term is also associated with compressibility effects, since the dilatation is zero for an incompressible flow. The three pressure terms are

$$\Pi_t = -\frac{\partial \overline{u''_2 p'}}{\partial x_2}, \quad \Pi_d = \overline{p' \frac{\partial u''_i}{\partial x_i}}, \quad \Pi_c = -\overline{u''_2} \frac{\partial \bar{p}}{\partial x_2}. \quad (5.7a-c)$$

Of the three, Π_d and Π_c are much smaller than Π_t near the wall (figure 24). In fact, the sum of the pressure terms is almost indistinguishable from Π_t in the wall region, which shows that the compressibility terms have very little effect on the overall contribution of the pressure terms to the turbulent kinetic energy budget. Away from the wall, all the terms are small and the compressibility term contributes to the sum of the terms. The pressure diffusion term is larger than the value obtained by Spalart in both his $Re_\theta = 1410$ and $Re_\theta = 670$ cases.

The results and analysis given here show that at $M = 2.5$, the effects of compressibility on the turbulent kinetic energy balance are not due to the new compressibility terms that appear in the equations. Instead, the effects are more subtle, quantitatively affecting the terms that appear in the incompressible case.

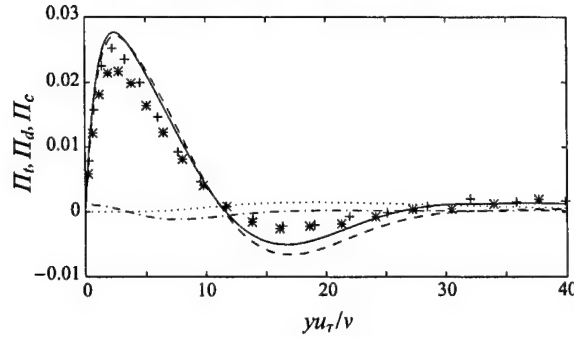


FIGURE 24. Comparison of pressure terms: —, $\Pi_i + \Pi_d + \Pi_c$; ----, Π_i ; - · - ·, Π_d ; · · · ·, Π_c ; +, Spalart's data $Re_\theta = 1410$; *, Spalart's data $Re_\theta = 670$.

6. Conclusions

A direct numerical simulation of a Mach 2.5 turbulent boundary layer was carried out using the method described in the Appendix. The Reynolds number of the simulation was $Re_\theta = 849$. Comparison with available experiments and with other simulations (i.e. those of Spalart) suggest that the current simulation provides an accurate description of a compressible turbulent boundary layer.

It was shown that many of the scaling relations used to express compressible boundary layer statistics in terms of those for incompressible boundary layers are consistent with the current simulation. In particular, we have shown that the Van Driest transformed velocity behaves much the same as the streamwise velocity in the incompressible case. There was a small logarithmic region with $\kappa = 0.40$ and $C = 4.7$. It was also shown that the RMS velocity fluctuations are collapsed with incompressible results by the mean density scaling suggested by Morkovin. When this scaling is applied, the data from the current simulation agree remarkably well with Spalart's $Re_\theta = 670$ and $Re_\theta = 1410$ simulations. The mean density scaling of $\overline{u'v'}$ also results in a fairly good collapse with incompressible results.

An inconsistency with the standard analysis of compressible turbulent boundary layers was found in that the total temperature fluctuations were of the same order as temperature fluctuations. This invalidates many of the assumptions made in deriving the strong Reynolds analogy (SRA). However, the relationship between RMS temperature and streamwise velocity fluctuations, (4.9a), agreed with the simulation data reasonably well nonetheless. A condition for the validity of the RMS relationship in the presence of significant total temperature fluctuations was derived, (4.12), and this condition is satisfied by the simulation data. An expression for the correlation coefficient $R_{u'T''}$ derived by Gaviglio (4.15) using the RMS relationship agrees very well with the simulation data.

The low value of the correlation coefficient found in the simulations indicates that instantaneous relationships between temperature and velocity fluctuations, (4.8) for example, are invalid. Experimental evidence, however, suggests a much higher value of the correlation coefficient than was found in this simulation. It appears that this difference between experiments and the current simulation can be due to a difference of about a factor of 2 in the magnitude of the total temperature fluctuations, with the experimental values being smaller. The reason for this is not known.

The modified Reynolds analogy of Huang *et al.* showed better agreement with

the simulation data than Gaviglio's modified Reynolds analogy and the original expression of Morkovin. Using Huang *et al.*'s modified analogy, a relationship between the rate of turbulent heat transfer and turbulent momentum transfer was derived and shown to agree with the simulation data. The streamwise momentum and temperature fluctuations were found to be very highly correlated throughout the boundary layer with a correlation coefficient $0.88 \leq -R_{m,T'} \leq 1$. This is in contrast to the low correlation between the velocity and thermal fields away from the wall and also stands in contrast to the lack of correlation between streamwise momentum and temperature in the incompressible case (where velocity and momentum are proportional).

The turbulent kinetic energy budget was calculated and compared with those of Spalart's incompressible simulations. The peak rate of production was found to be larger than for the incompressible case. This is balanced by an increase in the magnitude of turbulent transport and viscous transport when compared to the incompressible simulations. Some of this difference might be attributable to the different small-scale resolution used in these two simulations, with the current simulation having better resolution than the simulations of Spalart. Balances for the terms in the Reynolds stress tensor have been computed and are presented in Guarini (1998).

The authors would like to thank NASA's Numerical Aerodynamic Simulation facility (NAS) and the Air Force Aeronautical Systems Center (ASC) Major Shared Resource Center (MSRC) for their computational support. The simulation and code development were done on the Cray C-90 supercomputers at these two facilities. The support of a NASA Graduate Student Researchers Program grant (NGT 2-52209) and AFOSR grant F49620-97-1-0089 is gratefully acknowledged by the first and second authors, respectively.

Appendix. Theoretical development

In this appendix we review Spalart's transformation and apply it to the compressible boundary layer. This involves the development of a generalized coordinate system in which boundary layer growth is minimal, the definition of the two scales involved in the problem, the transformation of the Navier-Stokes equations to the new curvilinear coordinate system, and the calculation of the slow-growth terms. This analysis for the compressible case mirrors that developed by Spalart (Spalart & Leonard 1987; Spalart 1988) for the incompressible boundary layer. The particulars of that analysis that are directly relevant to the current development are recalled briefly in § A.2 and § A.3 to fix the ideas and the nomenclature.

A.1. Equations

The form of the Navier-Stokes equations is chosen for computational convenience. The energy equation is transformed so that pressure is a state variable instead of energy. The fluid variables, u_i , $m_i = \rho u_i$, p , and $\sigma = (1/\rho)$ are non-dimensionalized by a_o , $\rho_o a_o$, $\rho_o a_o^2$, and $(1/\rho_o)$, respectively. Lengths are non-dimensionalized by δ_o and times by (δ_o/a_o) . Then the Navier-Stokes equations become

$$\frac{\partial \sigma}{\partial t} = \sigma^2 \frac{\partial m_j}{\partial x_j}, \quad (\text{A } 1a)$$

$$\frac{\partial m_i}{\partial t} = -\frac{\partial}{\partial x_j}(\sigma m_i m_j) - \frac{\partial p}{\partial x_i} + \frac{1}{Re} \frac{\partial \tau_{ij}}{\partial x_j}, \quad (\text{A } 1b)$$

$$\frac{\partial p}{\partial t} = -\frac{\partial p u_j}{\partial x_j} - (\gamma - 1)p \frac{\partial u_j}{\partial x_j} + \left(\frac{\gamma - 1}{Re}\right) \tau_{ij} \frac{\partial u_i}{\partial x_j} + \frac{1}{Re Pr} \frac{\partial q_j}{\partial x_j}. \quad (\text{A } 1c)$$

The Reynolds number is $Re = (\rho_o a_o \delta_o) / \mu_o$ and the Prandtl number is $Pr = (\mu C_p) / k$. The Fourier heat conduction law, q_j , is given by

$$q_j = \mu \frac{\partial T}{\partial x_j}, \quad (\text{A } 2)$$

and the stress, τ_{ij} , is

$$\tau_{ij} = \mu \left(\frac{\partial u_i}{\partial x_j} + \frac{\partial u_j}{\partial x_i} - \frac{2}{3} \delta_{ij} \frac{\partial u_k}{\partial x_k} \right). \quad (\text{A } 3)$$

The temperature, T , is non-dimensionalized by $T_o \equiv a_o^2 / (\gamma R)$, such that the equation of state, $T = \gamma \sigma P$, results.

A.2. Coordinate system

Following Spalart (Spalart & Leonard 1987; Spalart 1988), the Navier-Stokes equations are transformed into a coordinate system that is fitted to the growing boundary layer. The new coordinate system is (ξ, η, z) , where

$$\xi = x \quad \text{and} \quad \eta = \eta(x, y). \quad (\text{A } 4)$$

Curves of $\eta = \text{const.}$ are slightly inclined to the wall with a slope $\tilde{S}(\xi, \eta)$ chosen in such a way that we fit the growth of both the boundary layer and the viscous sublayer. This coordinate system is selected so that when a small section of the boundary layer is simulated, the variation of the mean fluid dynamic variables along a constant- η curve is so small that approximate homogeneity will hold.

The Jacobian of the transformation involves two parameters, \tilde{S} and \tilde{T} , where

$$\tilde{S} \equiv \frac{\partial y}{\partial \xi} \Big|_{\eta, z} \quad \text{and} \quad \tilde{T} \equiv \frac{\partial y}{\partial \eta} \Big|_{\xi, z}. \quad (\text{A } 5)$$

The quantity \tilde{S} gives the slope of the constant- η curves, while \tilde{T} is the local stretching between the y - and η -coordinates, and $\tilde{S}_\eta = \tilde{T}_\xi$ follows from (A 5). In terms of \tilde{S} and \tilde{T} , the Jacobian is given by

$$\begin{Bmatrix} \partial/\partial x \\ \partial/\partial y \\ \partial/\partial z \end{Bmatrix} = \begin{bmatrix} 1 & -\tilde{S}/\tilde{T} & 0 \\ 0 & 1/\tilde{T} & 0 \\ 0 & 0 & 1 \end{bmatrix} \begin{Bmatrix} \partial/\partial \xi \\ \partial/\partial \eta \\ \partial/\partial z \end{Bmatrix}. \quad (\text{A } 6)$$

A.3. Multiple-scale analysis

Even in the transformed coordinate system, the mean variables evolve slowly in ξ . The fluctuations also have a slow variation in intensity at constant η . Thus, for example, we approximate

$$u'(\xi, \eta, z, t) = A_u(\xi, \eta) u_p(\xi, \eta, z, t), \quad (\text{A } 7)$$

where A_u is a slowly varying amplitude and u_p is homogeneous, so that in the simulation it can be treated as periodic in ξ . The subscript on A refers to the fluid dynamic variable with which it is associated. The fluctuations of the other state variables may be similarly decomposed. After introducing a slow variable $\Xi = \epsilon \xi$ and a fast variable ξ , and using the techniques of multiple-scale asymptotics, decomposition of the velocity into a mean and fluctuating part yields

$$u(\xi, \Xi, \eta, z, t) = U(\Xi, \eta) + A_u(\Xi, \eta) u_p(\xi, \eta, z, t), \quad (\text{A } 8)$$

and the derivative in the streamwise direction becomes

$$\frac{\partial u}{\partial \xi} = \epsilon \frac{\partial U}{\partial \Xi} + A_u \frac{\partial u_p}{\partial \xi} + \epsilon u_p \frac{\partial A_u}{\partial \Xi}. \quad (\text{A } 9)$$

Using (A 7) this can be rewritten in the compact form

$$u_\xi = \epsilon U_\Xi + u'_\xi + \epsilon u'_\Xi, \quad (\text{A } 10)$$

where $u'_\Xi = A_{u_\Xi} u' / A_u$.

To allow $u'_\Xi = A_{u_\Xi} u' / A_u$ to be determined in the actual simulation, note that

$$\frac{A_{u_\Xi}}{A_u} = \frac{(u'_{rms})_\Xi}{u'_{rms}}. \quad (\text{A } 11)$$

The coordinate system is also slowly varying in ξ and hence $y = y(\Xi, \eta)$, so that (A 5) is rewritten as

$$\tilde{S} = \epsilon \left. \frac{\partial y}{\partial \Xi} \right|_{\eta, z} \quad \text{and} \quad \tilde{T} = \left. \frac{\partial y}{\partial \eta} \right|_{\Xi, z}. \quad (\text{A } 12)$$

The simulations can be regarded as being performed at a fixed value $\Xi = \Xi_0$ of the slow variable. We are then free to choose η such that $y(\Xi_0, \eta) = \eta$ which implies $\tilde{T}(\Xi_0, \eta) = 1$. We define S such that $\tilde{S} = \epsilon S$.

A.4. Modified Navier–Stokes equations

Using the definitions above and replacing derivatives in ξ with slow and fast derivatives gives the transformed Navier–Stokes equations, that contain several additional terms, shown enclosed in square brackets:

$$\frac{\partial \sigma}{\partial t} = \sigma^2 \frac{\partial m_j}{\partial \xi_j} + \epsilon \left[-S \sigma^2 \frac{\partial m_1}{\partial \eta} \right] + \epsilon [-(\bar{\sigma}_\Xi + \sigma'_\Xi) \sigma m_1 + \sigma(U_\Xi + u'_\Xi)], \quad (\text{A } 13a)$$

$$\begin{aligned} \frac{\partial m_1}{\partial t} = & -\frac{\partial}{\partial \xi_j} (\sigma m_1 m_j) - \frac{\partial p}{\partial \xi} + \frac{1}{Re} \frac{\partial \tau_{1j}}{\partial \xi_j} + \epsilon \left[S \frac{\partial}{\partial \eta} (u_1 m_1) + S \frac{\partial p}{\partial \eta} \right] \\ & + \epsilon [(\bar{\sigma}_\Xi + \sigma'_\Xi) m_1^2 - 2(U_\Xi + u'_\Xi) m_1 - (\bar{p}_\Xi + p'_\Xi)], \end{aligned} \quad (\text{A } 13b)$$

$$\begin{aligned} \frac{\partial m_2}{\partial t} = & -\frac{\partial}{\partial \xi_j} (\sigma m_2 m_j) - \frac{\partial p}{\partial \eta} + \frac{1}{Re} \frac{\partial \tau_{2j}}{\partial \xi_j} + \epsilon \left[\frac{S}{2} \frac{\partial}{\partial \eta} (u_1 m_2 + u_2 m_1) \right] \\ & + \epsilon [(\bar{\sigma}_\Xi + \sigma'_\Xi) m_1 m_2 - (U_\Xi + u'_\Xi) m_2 - (V_\Xi + v'_\Xi) m_1], \end{aligned} \quad (\text{A } 13c)$$

$$\begin{aligned} \frac{\partial m_3}{\partial t} = & -\frac{\partial}{\partial \xi_j} (\sigma m_3 m_j) - \frac{\partial p}{\partial z} + \frac{1}{Re} \frac{\partial \tau_{3j}}{\partial \xi_j} + \epsilon \left[\frac{S}{2} \frac{\partial}{\partial \eta} (u_3 m_1 + u_1 m_3) \right] \\ & + \epsilon [(\bar{\sigma}_\Xi + \sigma'_\Xi) m_1 m_3 - (W_\Xi + w'_\Xi) m_1 - (U_\Xi + u'_\Xi) m_3], \end{aligned} \quad (\text{A } 13d)$$

$$\begin{aligned} \frac{\partial p}{\partial t} = & -\frac{\partial p u_j}{\partial \xi_j} - (\gamma - 1) p \frac{\partial u_j}{\partial \xi_j} + \left(\frac{\gamma - 1}{Re} \right) \tau_{ij} \frac{\partial u_i}{\partial \xi_j} + \frac{1}{Re Pr} \frac{\partial q_j}{\partial \xi_j} \\ & + \epsilon \left[S \frac{\partial}{\partial \eta} (p u_1) + S(\gamma - 1) p \frac{\partial u_1}{\partial \eta} \right] + \epsilon [-(\bar{p}_\Xi + p'_\Xi) \sigma m_1 - (U_\Xi + u'_\Xi) \gamma p]. \end{aligned} \quad (\text{A } 13e)$$

Note that all additional viscous terms have been neglected, since they are all multiplied by (S/Re) , which is small. In particular, near the wall, where the viscous terms are large, the value of S is approximately zero. The terms in square brackets are the corrections to the original Navier–Stokes equations that account for boundary layer growth. In each equation the first set of bracketed terms results from the coordinate transformation and the second set results from the multiple-scale analysis. These equations will be solved in a finite domain in the fast variable ξ . Thus, in the solution domain, functions of the slow variable Ξ can be taken as constant (functions of y) and the fluctuating quantities can be taken as homogeneous in the fast variable.

A.5. Slow derivatives of mean quantities

Before the modified equations (A 13) can be solved numerically, the slow derivatives must be determined in terms of the simulation solution variables. For any arbitrary slowly varying function f , $f_\Xi = f_\xi/\epsilon$. In what follows, it will be convenient to determine relations for f_ξ rather than f_Ξ . The slow derivatives of the mean thermodynamic quantities are calculated using the Van Driest (1955) temperature–velocity relationship as given by Walz (Fernholz & Finley 1980),

$$\frac{\bar{T}}{\bar{T}_\infty} = 1 + r \frac{\gamma - 1}{2} M_\infty^2 \left[1 - \left(\frac{\bar{u}}{\bar{u}_\infty} \right)^2 \right], \quad (\text{A } 14)$$

where the recovery factor, r , is taken to be $r = 0.896$. Equation (A 14) was found to be valid *a posteriori* in the simulations. Differentiating (A 14), the temperature derivative is expressed in terms of the mean velocity:

$$\frac{\bar{T}_\xi}{\bar{T}_\infty} = -r(\gamma - 1) M_\infty^2 \left(\frac{\bar{u}}{\bar{u}_\infty} \right) \left(\frac{\bar{u}_\xi}{\bar{u}_\infty} \right). \quad (\text{A } 15)$$

Since the pressure gradient, \bar{p}_ξ , is zero we get

$$\frac{\bar{p}_\xi}{\bar{p}} = -\frac{\bar{T}_\xi}{\bar{T}}. \quad (\text{A } 16)$$

Introducing means and fluctuations into the relationship $\sigma\rho = 1$, averaging, and neglecting $\sigma'\rho'$ gives after differentiation

$$\frac{\bar{\sigma}_\xi}{\bar{\sigma}} = -\frac{\bar{p}_\xi}{\bar{p}}. \quad (\text{A } 17)$$

Thus all the slow derivatives of mean thermodynamic variables are related directly to the slow derivative of the mean streamwise velocity.

For his incompressible simulation at the first station, Spalart used the well-known scaling laws for the mean streamwise velocity to calculate its slow derivatives. There is no equivalent scaling for compressible flow. However, the Van Driest transformation allows one to define a transformed velocity which satisfies the incompressible scalings. This transformation was found to be valid *a posteriori* in the simulations (see § 3.1). In the definition of the van Driest transformed velocity, U_c (3.2), $\sqrt{\bar{T}_w/\bar{T}}$ is a function of ξ and U . Differentiating (3.2) with respect to ξ yields

$$\frac{\partial U_c(\xi, \eta)}{\partial \xi} = \int_0^{U(\xi, \eta)} \frac{\partial}{\partial \xi} \left(\frac{\bar{T}_w}{\bar{T}} \right)^{1/2} dU + \left(\frac{\bar{T}_w}{\bar{T}} \right)^{1/2} \bigg|_{U(\xi, \eta)} \frac{\partial U(\xi, \eta)}{\partial \xi}. \quad (\text{A } 18)$$

Now, the Van Driest temperature–velocity relationship (A 14) implies that temperature is a function of U alone provided the recovery factor, r , is independent of ξ .

Experiments have verified that this assumption is valid (Fernholz & Finley 1980). The first term in (A 18) is therefore zero yielding

$$U_\xi = \left(\frac{\bar{T}}{\bar{T}_w} \right)^{1/2} U_{c_i}. \quad (\text{A } 19)$$

To obtain U_{c_i} (or U_ξ) for use in the modified Navier–Stokes equations (A 13), the strategy is to develop a relationship between U_{c_i} and U_c using well-known model profiles for the velocity U_c . Then U_{c_i} can be calculated from U_c as determined in the simulation. Note that model profiles discussed below are used *only to evaluate slow derivatives*. The mean velocity profile is determined from the simulation *not from the model profiles*.

To develop an expression for U_{c_i} , a model profile for U_c that is valid across the entire boundary layer is needed. Since U_c is the Van Driest transformed velocity, we can use a model profile for the incompressible boundary layer, in particular, we use the relation of Coles (1956):

$$\frac{U_{c_m}}{u_\tau} = \begin{cases} U_{c_b}/u_\tau + (\Pi/\kappa)w(y/\delta), & y \leq \delta, \\ U_{c_\infty}/u_\tau, & y > \delta, \end{cases} \quad (\text{A } 20)$$

where U_{c_b} is a basic law-of-the-wall profile and $w(y/\delta)$ is a wake function. In order to distinguish the model profile from that of the simulation, the model profile is denoted by U_{c_m} . For the basic profile and wake function we use the relations of Reichardt (1951) and Finley (Cebeci & Bradshaw 1977), respectively:

$$\frac{U_{c_b}}{u_\tau} = \frac{1}{\kappa} \ln \left(1 + \kappa \frac{yu_\tau}{v_w} \right) + C_1 \left[1 - e^{-yu_\tau/(\eta_1 v_w)} - \left(\frac{yu_\tau}{\eta_1 v_w} \right) e^{-yu_\tau b/v_w} \right], \quad (\text{A } 21)$$

and

$$\Pi w \left(\frac{y}{\delta} \right) = \left(\frac{y}{\delta} \right)^2 - \left(\frac{y}{\delta} \right)^3 + 6\Pi \left(\frac{y}{\delta} \right)^2 - 4\Pi \left(\frac{y}{\delta} \right)^3. \quad (\text{A } 22)$$

Several of the constants in these expressions are prescribed, that is $C_1 = -(1/\kappa) \ln(\kappa) + C$, $\eta_1 = 11$, and $b = 0.33$. The constants, u_τ , κ , and C are calculated from the simulation mean velocity profile at each time step. This leaves two parameters, δ and Π , which are determined by matching the properties of the model profile to the instantaneous simulation mean velocity profile. This profile is a good representation of the mean velocity throughout the boundary layer (see figure 5). Reichardt's profile is used instead of the classic profile of Coles because it captures both the linear sub-layer behaviour, where $U_c^+ = y^+$, and also the logarithmic behaviour of the mean velocity profile. The standard log-law becomes infinite at the wall which is undesirable in a simulation.

The parameters, δ and Π are set so that the free-stream velocity U_{c_∞} and the transformed displacement thickness of the model profile U_{c_m} match those in the simulation. Thus we have

$$U_{c_\infty} = U_{c_m}(\delta), \quad (\text{A } 23a)$$

$$\int_0^\infty \left(1 - \frac{U_c}{U_{c_\infty}} \right) dy = \int_0^\delta \left(1 - \frac{U_{c_m}}{U_{c_\infty}} \right) dy. \quad (\text{A } 23b)$$

These relations lead to a nonlinear system of equations for δ and Π (see Guarini 1998).

The slow derivative U_{c_t} can be written as

$$\frac{U_{c_t}}{u_\tau} = \frac{u_{\tau_t}}{u_\tau} \left(\frac{U_c}{u_\tau} \right) + \frac{\partial}{\partial \xi} \left(\frac{U_c}{u_\tau} \right). \quad (\text{A } 24)$$

Using the model profile to evaluate the derivative, (A 24) can be written

$$\frac{U_{c_t}}{u_\tau} = \frac{u_{\tau_t}}{u_\tau} \left(\frac{U_c}{u_\tau} \right) + \frac{\partial U_{c_m}}{\partial \delta} \delta_\xi + \frac{\partial U_{c_m}}{\partial u_\tau} u_{\tau_t} + \frac{\partial U_{c_m}}{\partial \Pi} \Pi_\xi, \quad (\text{A } 25)$$

leaving just u_{τ_t} , δ_ξ , and Π_ξ to be determined. It is known that Π becomes independent of Reynolds number for $Re_\theta > 5000$ (Cebeci & Bradshaw 1977) and that the variation of Π for lower Reynolds numbers is very small, thus the approximation $\Pi_\xi = 0$ is used. Since $U_{c_{\infty_t}} = 0$, (A 25) can be evaluated at $y = \delta$ to obtain a relation between u_{τ_t}/u_τ and δ_ξ/δ :

$$\frac{u_{\tau_t}}{u_\tau} = - \frac{(u_\tau^2 \delta / U_{c_\infty} v_w) \{ (1 + \kappa \delta u_\tau / v_w)^{-1} + R \}}{(u_\tau^2 \delta / U_{c_\infty} v_w) \{ (1 + \kappa \delta u_\tau / v_w)^{-1} + R \} + 1} \left(\frac{\delta_\xi}{\delta} \right), \quad (\text{A } 26)$$

where

$$R = \frac{C_1}{\eta_1} \left[e^{-\delta u_\tau / (v_w \eta_1)} + \left(\frac{\delta u_\tau b}{v_w} - 1 \right) e^{-\delta u_\tau b / v_w} \right], \quad (\text{A } 27)$$

and the assumption $S(y = \delta) = \delta_\xi/\delta$ has been made. To find δ_ξ/δ , the momentum integral equation, and the assumption $\delta_\xi/\delta = \theta_\xi/\theta$ (constant shape factor) is used to obtain

$$\frac{\delta_\xi}{\delta} = \frac{\tau_w}{\theta \bar{\rho}_\infty U_\infty^2}. \quad (\text{A } 28)$$

This closes the system of equations for U_{c_t}/u_τ .

Since the slowly varying amplitude functions are proportional to the RMS fluctuations, we can calculate the slow derivative of the velocity fluctuations by assuming a similar scaling law as was used by Spalart for his simulations, which yields

$$\frac{A_{vi\xi}}{A_{vi}} = \frac{u_{\tau_t}}{u_\tau}. \quad (\text{A } 29)$$

Since the simulation results show that the scaling used in the incompressible case is modified by the mean density profile, (A 29) could be improved by including this scaling.

To determine the metric S we take the first derivative with respect to ξ of the following expression given by Spalart (1988):

$$\eta_s = \frac{y_2^p (c_4 y^+) + y^p (y/\delta)}{y_2^p + y^p}, \quad (\text{A } 30)$$

where $y_2 = (y_1 y_3)^{1/2}$, $y_1 u_\tau / v_w = c_1$, $y_3 / \delta = c_2$, and $p = c_3 / \log_{10}(y_3 / y_1)$. Spalart's choices for the constants c_1 , c_2 , c_3 , and c_4 are 0.5, 0.3, 5.0, and 0.001, respectively; η_s is a weighted average of wall units and y/δ units. It should be noted that the quantity η_s is not the same as η and does not satisfy the conditions $y = \eta$ and $T = 1$ at the station of the simulation. Nonetheless, η_s can be used to calculate \tilde{S} since it follows the growth of the boundary layer and viscous sublayer (see Spalart 1988).

All the slow terms in (A 13) can now be determined from the simulated quantities, thus closing the equations.

REFERENCES

- ADAMS, N. A., MAEDER, T., GUO, Y. & KLEISER, L. 1998 Direct simulation of turbulent supersonic boundary layers by an extended temporal approach. Submitted to *J. Fluid Mech.*
- BARDINA, J. E., HUANG, P. G. & COAKLEY, T. J. 1980 Turbulence modeling validation, testing, and development. *NASA Tech. Mem.* 110446.
- BELL, D. M. & FERZIGER, J. H. 1993 Turbulent boundary layer DNS with passive scalars. In *Near-Wall Turbulent Flows* (ed. R. M. C. So, C. G. Speziale, B. E. Launder), pp. 327–336. Elsevier.
- BERTOLOTI, F. P., HERBERT, TH. & SPALART, P. R. 1992 Linear and nonlinear stability of the Blasius boundary layer. *J. Fluid Mech.* **242**, 441–474.
- CEBECI, T. & BRADSHAW, P. 1977 *Momentum Transfer in Boundary Layers*. Hemisphere.
- COLEMAN, G. N., KIM, J. & MOSER, R. D. 1995 A numerical study of turbulent supersonic isothermal-wall channel flow. *J. Fluid Mech.* **305**, 159–183.
- COLES, D. 1954 Measurements of turbulent friction on a smooth flat plate in supersonic flow *J. Aero. Sci.* **21**, 433–448.
- COLES, D. 1956 The law of the wake in the turbulent boundary layer. *J. Fluid Mech.* **1**, 191–226.
- DE BOOR, C. 1978 *A Practical Guide to Splines*. Springer.
- ELÉNA, M. & GAVIGLIO, J. 1993 Compressible turbulent boundary layer: survey of methods of analysis and results. *La Recherche Aéronautique* **2**, 1–21.
- FERNHOLZ, H. H. & FINLEY, P. J. 1980 A critical commentary on mean flow data for two-dimensional compressible boundary layers. *AGARD-AG-253*.
- GAVIGLIO, J. 1987 Reynolds analogies and experimental study of heat transfer in the supersonic boundary layer. *Intl J. Heat Mass Transfer*. **30**, 911–926.
- GILES, M. B. 1989 Non-reflecting boundary conditions for Euler equation calculations. *AIAA* 89-1942-CP.
- GILES, M. B. 1990 Nonreflecting boundary conditions for Euler equation calculations. *AIAA J.* **28**, 2050–2058.
- GUARINI, S. 1998 Direct numerical simulation of supersonic turbulent boundary layers. PhD thesis, Stanford University.
- GUO, Y. & ADAMS, N. A. 1994 Numerical investigation of supersonic turbulent boundary layers with high wall temperature. In *Proc. 1994 Summer Program of the Center for Turbulence Research, Stanford University*, pp. 245–267.
- HATAY, F. F. & BIRINGEN, S. 1995 Direct numerical simulation of low-Reynolds number supersonic turbulent boundary layers. *AIAA Paper* 95-0581.
- HUANG, P. G., COLEMAN, G. N. & BRADSHAW, P. 1995 Compressible turbulent channel flows: DNS results and modeling. *J. Fluid Mech.* **305**, 185–218.
- JIMENEZ, J. & MOIN, P. 1991 The minimal flow unit in near-wall turbulence. *J. Fluid Mech.* **225**, 213–240.
- KIM, J., MOIN, P. & MOSER, R. 1987 Turbulence statistics in fully developed channel flow at low Reynolds number. *J. Fluid Mech.* **177**, 133–166.
- KISTLER, A. L. 1959 Fluctuation measurements in a supersonic turbulent boundary layer. *Phys. Fluids* **2**, 290–296.
- KRAVCHENKO, A. G., MOIN, P. & MOSER, R. D. 1996 Zonal embedded grids for numerical simulation of wall-bounded turbulent flows. *J. Comput. Phys.* **127**, 412–423.
- LAUFER, J. 1964 Some statistical properties of the pressure field radiated by a turbulent boundary layer. *Phys. Fluids* **7**, 1191–1197.
- LELE, S. K. 1994 Compressibility effects on turbulence. *Ann. Rev. Fluid Mech.* **26**, 211–254.
- LOULOU, P. 1996 Direct numerical simulation of incompressible pipe flow using a b-spline spectral method. PhD thesis, Stanford University.
- LUND, T. S., WU, X. & SQUIRES, K. D. 1998 Generation of turbulent inflow data for spatially-developing boundary layer simulations. *J. Comput. Phys.* **140**, 233–258.
- MORKOVIN, M. V. 1962 Effects of compressibility on turbulent flows. In *Mécanique de la Turbulence* (ed. A. Favre) CNRS, pp. 367–380.
- RAI, M. M., GATSKI, T. B. & ERLEBACHER, G. 1995 Direct simulation of spatially evolving compressible turbulent boundary layers. *AIAA Paper* 95-0583.

- RAO, R. 1997 Direct numerical simulation of turbulent supersonic jets. PhD thesis, University of Minnesota.
- REICHARDT, H. 1951 Complete representation of the turbulent velocity distribution in smooth pipes. *Z. Angew Math. Mech.* **31**, 208–219.
- RUBESIN, M. W. 1990 Extra compressibility terms for Favre-averaged two-equations models of inhomogeneous turbulent flows. *NASA CR-177556*.
- SARKAR, S. 1995 The stabilizing effect of compressibility in turbulent shear flow. *J. Fluid Mech.* **282**, 163–186.
- SARKAR, S., ERLEBACHER, G., HUSSAINI, M. Y. & KREISS, H. O. 1991 The analysis and modeling of dilatational terms in compressible turbulence. *J. Fluid Mech.* **227**, 473–493.
- SHARIFF, K. & MOSER, R. D. 1998 Two-dimensional mesh embedding for B-spline methods. *J. Comput. Phys.* **145**, 471–488.
- SMITH, D. R. & SMITS, A. J. 1993 Simultaneous measurement of velocity and temperature fluctuations in the boundary layer of a supersonic flow. *Exp. Thermal Fluid Sci.* **7**, 221–229.
- SMITS, A. J. & DUSSAUGE, J. P. 1996 *Turbulent Shear Layers in Supersonic Flow*. American Institute of Physics.
- SPALART, P. R. 1988 Direct simulation of a turbulent boundary layer up to $Re_\theta = 1410$. *J. Fluid Mech.* **187**, 61–98.
- SPALART, P. R. & LEONARD, A. 1987 Direct numerical simulation of equilibrium turbulent boundary layers. In *Turbulent Shear Flows 5* (ed. F. J. Durst *et al.*) Springer, pp. 234–252.
- SPALART, P. R., MOSER, R. D. & ROGERS, M. M. 1991 Spectral methods for the Navier–Stokes equations with one infinite and two periodic directions. *J. Comput. Phys.* **96**, 297–324.
- SPALART, P. R. & WATMUFF, J. H. 1993 Experimental and numerical study of a turbulent boundary layer with pressure gradients. *J. Fluid Mech.* **249**, 337–371.
- SPINA, E. F., DONOVAN, J. F. & SMITS, A. J. 1991 Convection velocity in supersonic turbulent boundary layers. *Phys. Fluids A* **3**, 3124–3126.
- SPINA, E. F., SMITS, A. J. & ROBINSON, S. K. 1994 The physics of supersonic turbulent boundary layers. *Ann. Rev. Fluid Mech.* **26**, 287–319.
- SUBRAMANIAN, C. S. & ANTONIA, R. A. 1981 Effect of Reynolds number on a slightly heated turbulent boundary layer. *Intl J. Heat Mass Transfer.* **24**, 1833–1846.
- VAN DRIEST, E. R. 1951 Turbulent boundary layer in compressible fluids. *J. Aero. Sci.* **18**, 145–160.
- VAN DRIEST, E. R. 1955 The turbulent boundary layer with variable prandtl number. In *50 Jahre Grenzschichtforschung* (ed. H. Görtler) Vieweg.
- VAN DRIEST, E. R. 1956 On turbulent flow near a wall. *J. Aero. Sci.* **23**, 1007–1011, 1036.
- YOUNG, A. D. 1953 Boundary layers. In *Modern Developments in Fluid Dynamics High Speed Flow, Vol. 1* (ed. L. Howarth *et al.*), pp. 375–475. Oxford University Press.
- ZEMAN, O. 1990 Dilatation dissipation: The concept and application in modeling compressible mixing layers. *Phys. Fluids A* **2**, 178–188.

APPENDIX B

Preprint of "The decomposition of compressible boundary layer turbulence into acoustic and variable density parts" by S. Borodai and R. D. Moser (2000). Under consideration for publication in *Theo. Comp. Fluid Mech.*

THE NUMERICAL DECOMPOSITION OF TURBULENT FLUCTUATIONS IN A COMPRESSIBLE BOUNDARY LAYER.

STANISLAV G. BORODAI AND ROBERT D. MOSER

ABSTRACT. In many flows the turbulence is weakly compressible even at large Mach number. For example, in a compressible boundary layer with $Ma < 5$, the differences relative to an incompressible boundary layer are understood as being caused by density variations that accompany variations in temperature across the layer. Turbulent fluctuations in a compressible boundary layer are therefore expected to be dominated by the effects of non-constant temperature, and low Mach number theories in which acoustic fluctuations are not dominant should be applicable to the fluctuating field. However, the analysis of compressible boundary layer DNS data reveals the presence of significant acoustic fluctuations. To distinguish between acoustic and thermal effects, a numerical decomposition procedure for compressible boundary layer fluctuations is applied to determine the acoustic and nonacoustic fluctuations. Except for very near the wall, where the decomposition procedure is not valid, it is found that the nonacoustic fluctuations are only weakly coupled to the acoustic fluctuations, at Mach numbers as high as 6.

1. INTRODUCTION.

Much of the effort in turbulence research has been directed towards incompressible turbulence, due to the simplifications the incompressible assumption provides and because of the belief that turbulence is primarily an incompressible phenomenon. However, many flows of technological interest are compressible, so it is of some importance to understand the effects of compressibility on turbulence. Fortunately, it is observed in many flows that turbulence is in fact only weakly compressible, even at large Mach number.

In this paper we consider the effects of compressibility on turbulent boundary layers. A manifestation of weak compressibility in the boundary layer is Morkovin's hypothesis [18], which suggests that the dynamics of a compressible boundary layer

is close to incompressible as long as the fluctuating Mach number Ma' is small. Based on this hypothesis, compressible boundary layers with free stream Ma up to 5 are considered weakly compressible and the differences relative to an incompressible boundary layer are understood as being caused by the mean density variation that accompanies the mean temperature variation across the layer. Morkovin's hypothesis and other weakly compressible assumptions, such as the Van Driest transformation [4] and Strong Reynolds Analogy [18] have been widely used in modeling turbulence in compressible boundary layers [26, 13]. Morkovin's hypothesis breaks down when the Mach number is so large that the temperature fluctuations are substantial [26]. However, the extent to which true compressibility effects (i.e. finite propagation speed of pressure signals) are playing a role in this breakdown is not clear. If acoustic effects are not important in this breakdown, then a formal low Mach number asymptotic treatment of the turbulence may be applicable to much higher Mach numbers.

1.1. Low Mach number asymptotic analysis. Recently, a number of papers on low Mach number asymptotic descriptions of compressible flows have been published. Rigorous proofs of convergence to the incompressible flow equations in the limit of low Mach number under certain conditions were given by Klainerman and Majda [10, 11] for Euler equations with polytropic equation of state and by Kreiss *et al.* [12] for Navier-Stokes equations. However, the use of a polytropic equation of state restricts the applicability of the analysis, by eliminating the heat transfer effects important in the dynamics of a compressible boundary layer. When relaxing this restriction, it was pointed out by Matthaeus *et al.* [28] and more generally by Bayly *et al.* [1] that a variety of low Mach number asymptotic limits are possible, depending on the relative scaling of the thermal and acoustic fluctuations. Such analyses yield low Mach number approximations to the compressible Navier-Stokes equations, which may or may not include acoustic effects, depending on the details of the scaling. These approximations were also extended to more complicated situations, such as magnetohydrodynamics [16]. A number of exact solutions for low Mach number limits of the Navier-Stokes equations were derived by Fedorchenko [6].

Also, the low Mach number limit of compressible flow without the assumption of incompressibility at the lowest order velocity was considered by Müller [19].

In applying low Mach number asymptotics to a particular problem, it is necessary to determine which of several Mach number scalings is appropriate. For the adiabatic wall boundary layer turbulence, thermal effects appear to dominate over acoustics since temperature fluctuations are generated due to the presence of mean temperature gradients. This is consistent with approximations such as Morkovin's hypothesis. The heat flux dominated hydrodynamics of Zank & Matthaeus [28] is one asymptotic system that appears appropriate for the boundary layer. The determination of an appropriate low Mach number asymptotic limit for boundary layer turbulence will provide a basis for compressible turbulence modeling in this flow, and would provide a more rigorous foundation for such models than the approximations embodied in the Morkovin hypothesis and Strong Reynolds Analogy.

1.2. Weakly compressible turbulence models. The idea of utilizing the results of weakly compressible analysis in turbulence modeling is not new. It was used extensively by a number of authors. For example, Erlebacher *et al.* [5] used a weakly compressible asymptotic approach to study the influence of initial conditions on the turbulent dynamics, Sarkar *et al.* [23] and later Ristorcelli [21] used it to model the dilatational terms in compressible Reynolds stress model, and Rubinstein and Erlebacher [22], used this idea to derive the transport coefficients in weakly compressible turbulence and, as a result of that, proposed a generalized eddy viscosity model of turbulence. However, application of low Mach number asymptotics to turbulence modeling is fraught with uncertainties. In particular, one does not know a priori what low Mach number scaling applies to the case at hand. Further, in some cases, the asymptotic equations are written in terms of distinct acoustic and nonacoustic variables. It is very difficult to check modeling assumptions involving these quantities, since they are not physically realized, and so cannot be directly measured.

1.3. Compressible flow decompositions. When both acoustic and thermal effects are present, the use of weakly compressible asymptotics in modeling and other

applications would be greatly facilitated if one could distinguish the acoustic fluctuations from the turbulence in a compressible flow field. The idea of representing a compressible flow as a sum of different components was introduced by Chu & Kovásznyai [3]. They identified vortical, entropic and acoustic components. However, in their analysis Chu & Kovásznyai did not pursue the question of how the flow variables can be actually decomposed. Later, the mathematical procedure of decomposition of the flow variables was developed for various flows. Examples include decomposition of disturbances about an arbitrary potential mean flow [8] and about transversely sheared mean flow [7]. The review paper by Lele [13] gives more details about these decompositions. The results of these decompositions may provide certain advantages for the analysis of compressible flows, since the equations for the individual flow components are less complicated [20].

To actually apply such a decomposition analysis to extract acoustic components of a flow, one needs the three-dimensional velocity, density and temperature (or pressure) fields. Currently, such data are only available from direct numerical simulation (DNS). Such simulation data was used by Blaisdell [2] to decompose turbulence pressure to aid in the study of the pressure strain correlation. But, in this case only homogeneous shear turbulence was considered.

1.4. Decomposition development. The research reported here was undertaken to facilitate the use of weakly compressible asymptotics for the analysis and modeling of turbulence in a compressible boundary layer. Fields obtained from the direct numerical simulations of Maeder *et al.* [14] at Mach numbers ranging from 3 to 6 were subjected to extensive analysis to evaluate the validity of the asymptotics and to characterize the compressibility effects.

A preliminary analysis (reported in section 3) of this data shows that the HFDH of Zank & Matthaeus [28] is an inadequate description because acoustic pressure and dilatation fluctuations are not negligible. Based on these observations, a more appropriate low Mach number scaling is determined, and governing equations for acoustic and nonacoustic parts of the flow are derived (section 4). These equations, extended to the case of weakly compressible fluctuations in the flow with supersonic

mean (appendix A), are used in section 5 to devise a numerical decomposition algorithm to separate the acoustic and nonacoustic fluctuations, and this decomposition is validated. Finally in section 6, the results of the decomposition are discussed, along with some concluding remarks.

2. PRELIMINARIES.

The research discussed here is based on analysis of the compressible Navier-Stokes equations, and the direct numerical simulation (DNS) of compressible flow.

2.1. Compressible Navier-Stokes equations. In nondimensional form the compressible Navier-Stokes equations are:

$$\frac{\partial \rho}{\partial t} + \frac{\partial \rho u_i}{\partial x_i} = 0, \quad (1)$$

$$\frac{\partial u_i}{\partial t} + u_j \frac{\partial u_i}{\partial x_j} = -\frac{1}{\gamma Ma^2} V \frac{\partial p}{\partial x_i} + \frac{2}{Re} V \frac{\partial \mu \dot{s}_{ij}}{\partial x_j}, \quad (2)$$

$$\frac{\partial p}{\partial t} + u_j \frac{\partial p}{\partial x_j} + \gamma p \frac{\partial u_k}{\partial x_k} = \frac{\gamma - 1}{Pr Re} \frac{\partial}{\partial x_k} \left(\mu \frac{\partial T}{\partial x_k} \right) + 2 \frac{(\gamma - 1) \gamma Ma^2}{Re} \mu \dot{s}_{ij} \dot{s}_{ij}, \quad (3)$$

$$p = \frac{\gamma - 1}{\gamma} \rho T. \quad (4)$$

Where

$$\dot{s}_{ij} = \frac{1}{2} \left(\frac{\partial u_i}{\partial x_j} + \frac{\partial u_j}{\partial x_i} \right) - \frac{1}{3} \delta_{ij} \frac{\partial u_k}{\partial x_k} \quad (5)$$

is the deviatoric part of the strain-rate tensor, $V = 1/\rho$ is the specific volume, $\gamma = c_p/c_v$ is the adiabatic index with specific heats c_p and c_v considered to be constants. The Fourier heat conduction law is used in (3) to express the heat flux. The second coefficient of viscosity is assumed to be zero, and the ideal gas law (4) is the equation of state. As is appropriate for boundary layer analysis, free stream values of stream-wise velocity (u_∞), density (ρ_∞) and pressure (p_∞), and the boundary layer thickness (δ) were chosen as reference quantities to nondimensionalize equations (1)–(4). The coefficients of viscosity μ and thermal conductivity λ were scaled with respect to their free stream values μ_∞ and λ_∞ , and the dimensionless parameters in (1)–(4) are the Mach number $Ma = u_\infty/c_\infty$ where $c_\infty = \sqrt{\gamma p_\infty/\rho_\infty}$ is the sound speed, the Reynolds number $Re = (\rho_\infty u_\infty \delta)/\mu_\infty$ and the Prandtl number

$Pr = (\mu_\infty c_p)/\lambda_\infty$. The Prandtl number is assumed to be constant. The dynamic coefficient of viscosity μ is dependent on temperature T only, according to the Sutherland law (see, for example, White [27]):

$$\mu = \left(\frac{T}{\alpha}\right)^{\frac{3}{2}} \frac{1 + T_{su}/T_\infty}{T/\alpha + T_{su}/T_\infty}, \quad (6)$$

where T_{su} is the Sutherland constant, T_∞ is the free stream temperature and the coefficient $\alpha = (T_\infty \rho_\infty c_p)/p_\infty = \gamma/(\gamma - 1)$ is a consequence of the way temperature was nondimensionalized ($T = T^* \rho_\infty c_p/p_\infty$, where T^* is dimensional temperature).

We use the geophysical coordinate system, so x is the streamwise, y is the spanwise and z is the wall-normal coordinate. The (+) superscript denotes the variables in wall units, and δ_{99} is used as the boundary layer thickness δ . Reynolds mean quantities are obtained by averaging over streamwise and spanwise directions. Profiles of various quantities presented in the figures are averages over time.

2.2. Governing equations for fluctuations. Turbulent fluctuations are the topic of primary interest. The equations for the fluctuations can be obtained from (1)–(4) by subtracting the equations for the Reynolds averaged mean in the usual way. The result is:

$$\frac{\partial p'}{\partial t} + \frac{\partial \bar{p}' u_i}{\partial x_i} + \frac{\partial \bar{p}' u_i'}{\partial x_i} + \left(\frac{\partial \bar{p}' u_i'}{\partial x_i}\right)' = 0, \quad (7)$$

$$\begin{aligned} \frac{\partial u_i'}{\partial t} + \bar{u}_j \frac{\partial u_i}{\partial x_j} + u_j' \frac{\partial \bar{u}_i}{\partial x_j} + \left(u_j' \frac{\partial u_i'}{\partial x_j}\right)' = \\ = -\frac{1}{\gamma Ma^2} \left(\bar{V} \frac{\partial p'}{\partial x_i} + V' \frac{\partial \bar{p}}{\partial x_i} + \left(V' \frac{\partial p'}{\partial x_i}\right)' \right) + \frac{2}{Re} \left(V \frac{\partial \mu_{ij}^{\circ}}{\partial x_j} \right)', \end{aligned} \quad (8)$$

$$\begin{aligned} \frac{\partial p'}{\partial t} + \bar{u}_j \frac{\partial p'}{\partial x_j} + u_j' \frac{\partial \bar{p}}{\partial x_j} + \left(u_j' \frac{\partial p'}{\partial x_j}\right)' + \gamma \bar{p} \frac{\partial u_k'}{\partial x_k} + \gamma p' \frac{\partial \bar{u}_k}{\partial x_k} + \left(\gamma p' \frac{\partial u_k'}{\partial x_k}\right)' = \\ = \frac{\gamma - 1}{Pr} \frac{\partial}{Re \partial x_k} \left(\mu \frac{\partial T}{\partial x_k} \right)' + 2 \frac{(\gamma - 1) \gamma Ma^2}{Re} \left(\mu_{ij}^{\circ} s_{ij}^{\circ} \right)', \end{aligned} \quad (9)$$

$$p' = \frac{\gamma - 1}{\gamma} \left(\bar{p} T' + \rho' \bar{T} + (\rho' T')' \right). \quad (10)$$

The overbar in the equations (7)–(10) denotes Reynolds average, prime denotes fluctuations. It is common to define the mean and fluctuations via the Favre average (for a given variable β , the Favre average is $\tilde{\beta} = \overline{\rho \beta} / \bar{\rho}$), since it makes the mean

equations simpler. However, the use of Favre average does not significantly simplify the fluctuating equations, and for the current analysis the Reynolds average was found to be more convenient. A similar analysis using the Favre average is also possible.

2.3. Properties of DNS data. In our research, data from the parallel boundary layer simulations of Maeder *et al.* [14] with free stream Mach numbers of 3, 4.5 and 6 were used. The grid and domain sizes for these simulations are shown in the table 1 (x, y and z are stream-wise, span-wise and wall-normal directions respectively), the physical parameters are provided in table 2.

Ma	Grid size ($N_x \times N_y \times N_z$)	Domain size ($L_x \times L_y \times L_z$)
3.0	$192 \times 144 \times 180$	$543^+ \times 310^+ \times 1163^+$
4.5	$432 \times 192 \times 200$	$1175^+ \times 282^+ \times 470^+$
6.0	$240 \times 160 \times 220$	$319^+ \times 193^+ \times 404^+$

TABLE 1. DNS grid and domain sizes.

Ma	Re_θ	T_w/T_∞	$C_f * 10^3$	H_{12}	u_τ
3.0	3028	2.50	2.02	5.86	0.0498
4.5	3196	4.38	1.46	9.22	0.0552
6.0	2945	6.98	1.14	17.20	0.0614

TABLE 2. DNS physical parameters.

In Maeder's simulations, the parallel boundary layer approximation is used, which is based on the assumption that the boundary layer is growing slowly in the stream-wise direction. This allows one to consider a boundary layer with parallel streamlines, while boundary layer growth is accounted for by extra terms introduced into governing equations through a two-scale asymptotic treatment. The homogenization technique used by Maeder is similar to that of Spalart [25] who also uses a two-scale asymptotic analysis in the boundary layer.

The horizontal domain size in Maeder's simulation is smaller than that used by other authors (e.g. Guarini [9]), so some of the flow details in Maeder's simulation may be affected by domain size. However, the Maeder's data is suitable for our

purposes since we are primarily interested in compressibility effects which can be investigated in small spatial domains.

In these simulations, the boundary conditions at the wall were no-slip and isothermal with temperature set to the adiabatic wall temperature. For the free-stream boundary, non-reflecting boundary conditions are used.

3. APPLICABILITY OF THE HFDH APPROXIMATION.

Compressibility effects observed in turbulent boundary layers are thought to be dominated by variable fluid property effects (density and viscosity) [26]. One would therefore expect the turbulence to be well described by a formulation in which acoustic effects play only a minor role in the flow evolution, being a higher order correction in the variable fluid properties governing equations. In particular, the Heat Flux Dominated Hydrodynamics (HFDH) description of Zank & Matthaeus [28] would be expected to be valid. To determine if this is in fact the case, the DNS data of Maeder is examined, as described in section 2.

In the HFDH limit, the energy equation expressed in terms of the pressure reduces to a compatibility condition relating velocity divergence to the divergence of heat flux:

$$\gamma P \frac{\partial u_k}{\partial x_k} = \frac{\gamma - 1}{Pr Re} \frac{\partial}{\partial x_k} \left(\mu \frac{\partial T}{\partial x_k} \right). \quad (11)$$

Applying a similar analysis to the turbulent fluctuating pressure equation (9), one obtains a relation for the fluctuating divergence:

$$\gamma P \frac{\partial u'_k}{\partial x_k} = \frac{\gamma - 1}{Pr Re} \frac{\partial}{\partial x_k} \left(\mu \frac{\partial T}{\partial x_k} \right)'. \quad (12)$$

This relationship was tested directly in the DNS data, and the results are shown in figure 1. Throughout the boundary layer, there is a significant error in the satisfaction of this equation; on the order of 50%. An examination of the remaining terms in the pressure equation shows that there are several other significant terms with magnitudes comparable to those in (12). The following relation represents equation (12) extended to include all of the most significant terms in the fluctuating

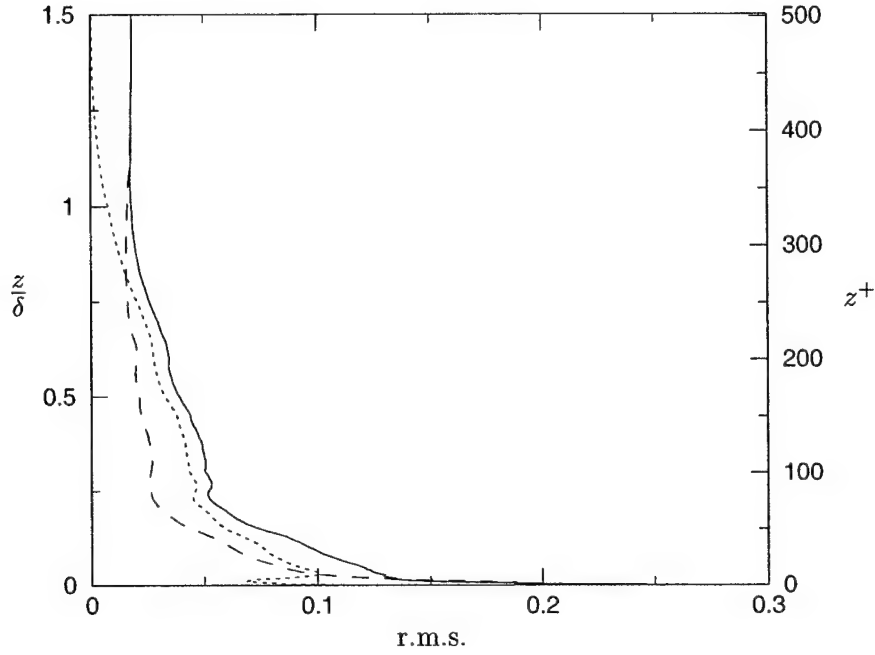


FIGURE 1. The r.m.s. profiles of the terms from relation (12): the divergence term $\gamma \bar{p} \frac{\partial u'_k}{\partial x_k}$ (—), the heat flux term $\frac{\gamma-1}{Pr Re} \frac{\partial}{\partial x_k} \left(\mu \frac{\partial T}{\partial x_k} \right)'$ (.....) and the difference $\gamma \bar{p} \frac{\partial u'_k}{\partial x_k} - \frac{\gamma-1}{Pr Re} \frac{\partial}{\partial x_k} \left(\mu \frac{\partial T}{\partial x_k} \right)'$ (- - -). The z on this figure is the wall-normal coordinate, $\delta = \delta_{99}$ is the boundary layer thickness ($Ma = 3$).

pressure equation:

$$\frac{\partial p'}{\partial t} + \bar{u}_j \frac{\partial p'}{\partial x_j} + \left(u'_j \frac{\partial p'}{\partial x_j} \right)' + \gamma \bar{p} \frac{\partial u'_k}{\partial x_k} = \frac{\gamma-1}{Pr Re} \frac{\partial}{\partial x_k} \left(\mu \frac{\partial T}{\partial x_k} \right)'; \quad (13)$$

r.m.s. profiles of these terms are presented in figure 2. The first three terms in (13) (which are the difference between (12) and (13)) are large and do not cancel each other, despite the fact that in the context of the HFDH asymptotics, these terms are higher order.

A clue to the nature of the discrepancy is provided in figure 1. Note that outside the boundary layer ($z/\delta \leq 1$), there is significant velocity divergence, but no heat-flux divergence. In this region the fluctuating divergence must then be attributable to acoustics. The magnitude of this acoustic component of fluctuating divergence

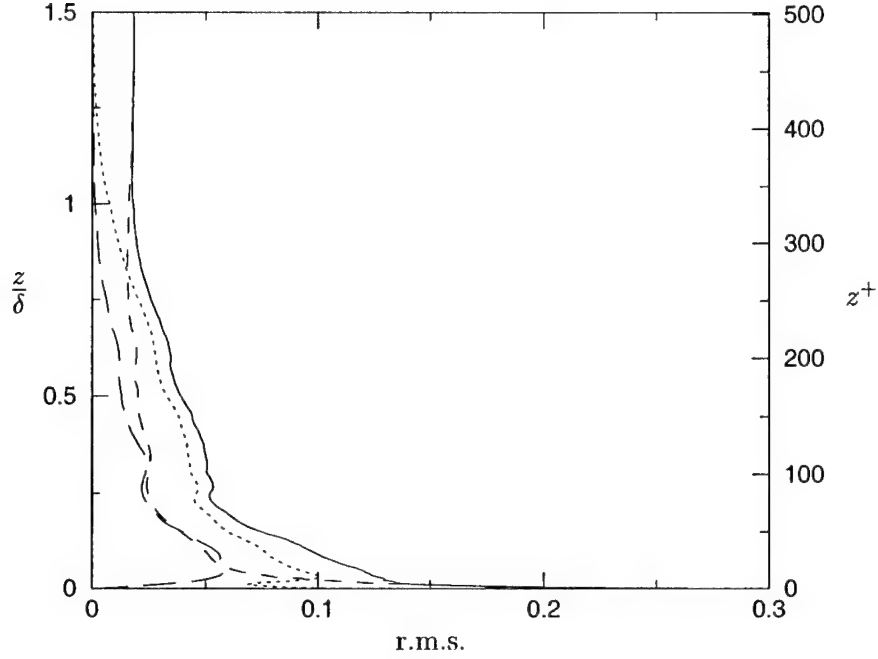


FIGURE 2. The r.m.s. profiles of the most significant terms in fluctuating pressure equation: the divergence term $\gamma \bar{p} \frac{\partial u'_k}{\partial x_k}$ (—), the heat flux term $\frac{\gamma-1}{Pr Re} \frac{\partial}{\partial x_k} \left(\mu \frac{\partial T}{\partial x_k} \right)'$ (.....), convective time derivative $\frac{Dp'}{Dt} = \frac{\partial p'}{\partial t} + \bar{u}_j \frac{\partial p'}{\partial x_j}$ (---), and convection with fluctuating velocity $\left(u'_j \frac{\partial p'}{\partial x_j} \right)'$ (- - -) ($Ma = 3$).

is likely to stay the same in the boundary layer, since there is nothing preventing acoustics from propagating into the boundary layer. Thus, there appears to be an acoustic component of the fluctuating divergence with a magnitude of the same order as the magnitude of the divergence generated by the heat flux, suggesting that the mismatch in the compatibility condition (12) is due to the acoustic fluctuations.

4. LOW MACH NUMBER ASYMPTOTIC ANALYSIS.

The goal of this research is to split compressible fluctuations into acoustic and nonacoustic parts. The governing equations for these parts can be obtained considering the limit of small turbulence Mach number. For simplicity, asymptotic analysis presented in this chapter deals with the case of low Mach number flow, the

extension to the case of low turbulence Mach number flow with supersonic mean is given in Appendix A. The resulting governing equations will be used in section 5 to perform the numerical decomposition of compressible fluctuations.

4.1. Asymptotic scaling. To begin the analysis, the leading order asymptotic behavior of the flow variables as the parameter $\varepsilon = \sqrt{\gamma}Ma \rightarrow 0$ should be postulated, since as described in section 1.1 there are several possible low Mach number asymptotic limits. Based on the observations of the DNS data described in section 3, the flow variables are assumed to be composed of incompressible (subscript 'I'), thermal (subscript 't') and acoustic (subscript 'a') parts, which scale with ε as follows:

$$\mathbf{u} = \mathbf{u}_I + \varepsilon(\mathbf{u}_t + \mathbf{u}_a), \quad (14)$$

$$p = 1 + \varepsilon^2(p_I + p_a), \quad (15)$$

$$T = \frac{\gamma}{\gamma - 1} + \varepsilon T_t + \varepsilon^2 T_a, \quad (16)$$

$$\rho = 1 + \varepsilon \rho_t + \varepsilon^2 \rho_a. \quad (17)$$

At zeroth order the flow variables are incompressible, with constant temperature and density (equal to $\frac{\gamma}{\gamma-1}$ and 1 respectively because of nondimensionalization (see section 2)), resulting in a constant zeroth order pressure (equal to 1 in this nondimensionalization). However, the incompressible pressure p_I , which appears in the incompressible Navier-Stokes equations, is of order $O(\varepsilon^2)$. Consistent with the observation (section 3) that the acoustic and nonacoustic divergence are of the same magnitude, the thermal and acoustic velocity parts are of the same order. This fixes the asymptotic scaling of the other thermal and acoustic quantities. Note that the acoustic pressure is then the same order as the incompressible pressure, although the acoustic density and temperature are of higher order than the corresponding thermal parts. The representation (14)–(17) is essentially an extension of the HFDH limit of Zank & Matthaeus [28] to include the acoustic component.

Since the viscosity depends only on temperature and specific volume is just the inverse of density, they can also be represented as:

$$\mu = 1 + \varepsilon \mu_t + \varepsilon^2 \mu_a, \quad (18)$$

$$V = 1 + \varepsilon V_t + \varepsilon^2 V_a. \quad (19)$$

In the limit of small Ma , there are two widely separated time scales: the incompressible convective time scale δ/u_∞ and acoustic time scale $\delta\sqrt{\gamma}/c_\infty$. The later time scale is smaller than the former by a factor of ε . So we can proceed as in multi-scale analysis and introduce two time variables, the incompressible (slow) time $t_I = u_\infty t^*/\delta = t$ and the acoustic (fast) time $t_a = c_\infty t^*/(\delta\sqrt{\gamma}) = t/\varepsilon$. The derivative with respect to t is then given by:

$$\frac{\partial}{\partial t} = \frac{1}{\varepsilon} \frac{\partial}{\partial t_a} + \frac{\partial}{\partial t_I}. \quad (20)$$

One can also formulate a low Mach number asymptotic analysis using multiple length scales. However, multiple length scale analysis is inappropriate in our case, since the results of this analysis will be applied to the DNS data, and this data does not support arbitrarily long wavelengths.

Note that in the current analysis we are not using a standard asymptotic expansion approach. In such an approach all the flow variables would be represented as power series of ε with order one coefficients, and then the necessary conditions for the coefficients would be derived. Instead, a consistent asymptotic behavior has been postulated through the leading order scalings in (14)–(19). Further, the coefficients in (14)–(19) (e.g. \mathbf{u}_t , \mathbf{u}_a , etc.) are order one, but they are not independent of ε , as would be the case in a standard asymptotic expansion. This means that there has been no higher order truncation of asymptotic expansion of the variables so far at this point in the analysis. The higher order terms in the expansions just got absorbed into the incompressible, thermal and acoustic variables.

The expansions (14)–(19) does not completely define what the incompressible, thermal and acoustic components of the flow are. It simply defines the leading order scaling of these components. So, other requirements must be imposed to uniquely

define the incompressible, thermal and acoustic components of a variable at a given order. These requirements are:

1. the incompressible velocity \mathbf{u}_I is divergence free, i.e.

$$\frac{\partial u_{Ij}}{\partial x_j} = 0; \quad (21)$$

2. the leading order variation of nonacoustic quantities on the acoustic time scale is only due to convection by the acoustic velocity, i.e. for a given variable β , the fast time derivative of its incompressible part β_I and thermal part β_t satisfy:

$$\frac{\partial \beta_{t,I}}{\partial t_a} + \varepsilon^2 u_{aj} \frac{\partial \beta_{t,I}}{\partial x_j} \sim o \left(\varepsilon^2 u_{aj} \frac{\partial \beta_{t,I}}{\partial x_j} \right), \quad (22)$$

where $\beta_{t,I}$ is either β_I or β_t ;

3. the slow time variation of the acoustic quantities is only due to their propagation through the slowly varying nonuniform medium.

It follows from (22), that the variation of nonacoustic parts $\beta_{t,I}$ on the fast time scale is two orders higher than the leading order of $\beta_{t,I}$, so at the lowest two orders, the nonacoustic parts $\beta_{t,I}$ can be distinguished from the acoustic part β_a by the fact that they only vary on the slow time scale. This definition becomes ambiguous at higher orders at which the nonacoustic parts have fast time scale variation by (22), therefore setting the maximum order that can be considered in the analysis. The highest order retained in the equations for a given variable β will be the order of the slow time derivative $\partial \beta_a / \partial t_I$ of the acoustic part of β .

Condition (1) specifies the distinction between the incompressible and the thermal variables, while conditions (2) and (3) distinguish the acoustic and non-acoustic (thermal and incompressible) quantities and provide a way of separating governing equations for these quantities at the orders of interest.

4.2. Derivation of acoustic and nonacoustic governing equations. Our goal is now to formally decompose the governing equations into separate equations for the acoustic and nonacoustic parts, as in Chu & Kováznay [3]. This is accomplished by separating the terms that involve only the slowly varying nonacoustic quantities, from those that involve acoustic quantities and are therefore rapidly varying. These

terms are decoupled on the fast time scale since the nonacoustic quantities do not vary on this time scale by item (2) above. They are decoupled on the slow time scale since the fast acoustic terms balance between themselves, even on the slow time scale (item 3 above). The fast time scale equation will be the acoustic governing equation, while the slow time scale equation will be the nonacoustic governing equation.

The representation (14)–(20) is substituted into (1)–(4), the terms of equal order in ε are collected up to the order of the slow derivative of the acoustic quantity, and the slow and fast terms are separated to obtain acoustic and nonacoustic governing equations.

For example, consider the expansion of the continuity equation (1) (using (21) and (22)):

$$\begin{aligned} & \frac{\partial \rho_t}{\partial t_a} + \varepsilon \left(\frac{\partial \rho_t}{\partial t_I} + \frac{\partial \rho_a}{\partial t_a} + u_{Ij} \frac{\partial \rho_t}{\partial x_j} + \frac{\partial u_{tj}}{\partial x_j} + \frac{\partial u_{aj}}{\partial x_j} \right) + \\ & \varepsilon^2 \left(\frac{\partial \rho_a}{\partial t_I} + u_{tj} \frac{\partial \rho_t}{\partial x_j} + u_{aj} \frac{\partial \rho_t}{\partial x_j} + u_{Ij} \frac{\partial \rho_a}{\partial x_j} + \rho_t \frac{\partial u_{tj}}{\partial x_j} + \rho_t \frac{\partial u_{aj}}{\partial x_j} \right) + O(\varepsilon^3) = 0. \end{aligned} \quad (23)$$

The fast terms in this equation yield the acoustic density equation:

$$\varepsilon \left(\frac{\partial \rho_a}{\partial t_a} + \frac{\partial u_{aj}}{\partial x_j} \right) + \varepsilon^2 \left(\frac{\partial \rho_a}{\partial t_I} + u_{Ij} \frac{\partial \rho_a}{\partial x_j} + \rho_t \frac{\partial u_{aj}}{\partial x_j} \right) + O(\varepsilon^3) = 0, \quad (24)$$

while the slow terms produce the nonacoustic density equation:

$$\varepsilon \left(\frac{\partial \rho_t}{\partial t_I} + u_{Ij} \frac{\partial \rho_t}{\partial x_j} + \frac{\partial u_{tj}}{\partial x_j} \right) + \varepsilon^2 \left(u_{tj} \frac{\partial \rho_t}{\partial x_j} + \rho_t \frac{\partial u_{tj}}{\partial x_j} \right) + O(\varepsilon^3) = 0. \quad (25)$$

Applying the same analysis to the the momentum equation (2), and keeping explicitly the terms up to the order of $\partial u_a / \partial t_I$, we get:

$$\begin{aligned} & \frac{1}{\varepsilon} \frac{\partial u_{Ii}}{\partial t_a} + \frac{\partial u_{Ii}}{\partial t_I} + u_{Ij} \frac{\partial u_{Ii}}{\partial x_j} + \frac{\partial u_{ti}}{\partial t_a} + \frac{\partial u_{ai}}{\partial t_a} + \\ & \varepsilon \left(\frac{\partial u_{ti}}{\partial t_I} + \frac{\partial u_{ai}}{\partial t_I} + u_{tj} \frac{\partial u_{Ii}}{\partial x_j} + u_{aj} \frac{\partial u_{Ii}}{\partial x_j} + u_{Ij} \frac{\partial u_{ti}}{\partial x_j} + u_{Ij} \frac{\partial u_{ai}}{\partial x_j} \right) = \\ & - \frac{\partial p_I}{\partial x_i} - \frac{\partial p_a}{\partial x_i} + \frac{2}{Re} \frac{\partial s_{Iij}}{\partial x_j} + \\ & \varepsilon \left(-V_t \frac{\partial p_I}{\partial x_i} - V_t \frac{\partial p_a}{\partial x_i} + \frac{2}{Re} \left(V_t \frac{\partial s_{Iij}^\circ}{\partial x_j} + \frac{\partial \mu_t s_{Iij}^\circ}{\partial x_j} + \frac{\partial s_{tij}^\circ}{\partial x_j} + \frac{\partial s_{aij}^\circ}{\partial x_j} \right) \right) + O(\varepsilon^2), \end{aligned} \quad (26)$$

where $\overset{\circ}{s}_{Iij} = \overset{\circ}{s}_{ij}(\mathbf{u} = \mathbf{u}_I)$, $\overset{\circ}{s}_{tij} = \overset{\circ}{s}_{ij}(\mathbf{u} = \mathbf{u}_t)$, and $\overset{\circ}{s}_{aij} = \overset{\circ}{s}_{ij}(\mathbf{u} = \mathbf{u}_a)$. Again, splitting (26) into acoustic and nonacoustic equations as discussed above, one obtains:

$$\frac{\partial u_{ai}}{\partial t_a} + \varepsilon \left(\frac{\partial u_{ai}}{\partial t_I} + u_{Ij} \frac{\partial u_{ai}}{\partial x_j} \right) = -\frac{\partial p_a}{\partial x_i} + \varepsilon \left(-V_t \frac{\partial p_a}{\partial x_i} + \frac{2}{Re} \frac{\partial \overset{\circ}{s}_{aij}}{\partial x_j} \right) + O(\varepsilon^2), \quad (27)$$

for the acoustic momentum equation and

$$\begin{aligned} \frac{\partial u_{Ii}}{\partial t_I} + u_{Ij} \frac{\partial u_{Ii}}{\partial x_j} + \varepsilon \left(\frac{\partial u_{ti}}{\partial t_I} + u_{tj} \frac{\partial u_{Ii}}{\partial x_j} + u_{Ij} \frac{\partial u_{ti}}{\partial x_j} \right) &= -\frac{\partial p_I}{\partial x_i} + \frac{2}{Re} \frac{\partial s_{Iij}}{\partial x_j} + \\ \varepsilon \left(-V_t \frac{\partial p_I}{\partial x_i} + \frac{2}{Re} \left(V_t \frac{\partial \overset{\circ}{s}_{Iij}}{\partial x_j} + \frac{\partial \mu_t \overset{\circ}{s}_{Iij}}{\partial x_j} + \frac{\partial \overset{\circ}{s}_{tij}}{\partial x_j} \right) \right) &+ O(\varepsilon^2). \end{aligned} \quad (28)$$

for the nonacoustic momentum equation. As may be expected, at lowest order the equation (28) is just the constant density incompressible Navier-Stokes equation governing \mathbf{u}_I .

Finally, the procedure is applied to the pressure equation (3)

$$\begin{aligned} \varepsilon \left(\frac{\partial p_I}{\partial t_a} + \frac{\partial p_a}{\partial t_a} + \gamma \frac{\partial u_{tj}}{\partial x_j} + \gamma \frac{\partial u_{aj}}{\partial x_j} \right) + \varepsilon^2 \left(\frac{\partial p_I}{\partial t_I} + \frac{\partial p_a}{\partial t_I} + u_{Ij} \frac{\partial p_I}{\partial x_j} + u_{Ij} \frac{\partial p_a}{\partial x_j} \right) &= \\ \varepsilon \frac{\gamma - 1}{Pr} \frac{\partial^2 T_t}{Re \partial x_k \partial x_k} + & \\ \varepsilon^2 \left(\frac{\gamma - 1}{Pr} \frac{\partial}{\partial x_k} \left(\mu_t \frac{\partial T_t}{\partial x_k} \right) + \frac{\partial^2 T_a}{\partial x_k \partial x_k} \right) + \frac{2(\gamma - 1)}{Re} \overset{\circ}{s}_{Iij} \overset{\circ}{s}_{Iij} &+ O(\varepsilon^3). \end{aligned} \quad (29)$$

yielding the acoustic pressure equation:

$$\varepsilon \left(\frac{\partial p_a}{\partial t_a} + \gamma \frac{\partial u_{aj}}{\partial x_j} \right) + \varepsilon^2 \left(\frac{\partial p_a}{\partial t_I} + u_{Ij} \frac{\partial p_a}{\partial x_j} \right) = \varepsilon^2 \frac{\gamma - 1}{Pr} \frac{\partial^2 T_a}{Re \partial x_k \partial x_k} + O(\varepsilon^3), \quad (30)$$

and nonacoustic pressure equation:

$$\begin{aligned} \varepsilon \gamma \frac{\partial u_{tj}}{\partial x_j} + \varepsilon^2 \left(\frac{\partial p_I}{\partial t_I} + u_{Ij} \frac{\partial p_I}{\partial x_j} \right) &= \varepsilon \frac{\gamma - 1}{Pr} \frac{\partial^2 T_t}{Re \partial x_k \partial x_k} + \\ \varepsilon^2 \left(\frac{\gamma - 1}{Pr} \frac{\partial}{\partial x_k} \left(\mu_t \frac{\partial T_t}{\partial x_k} \right) + \frac{2(\gamma - 1)}{Re} \overset{\circ}{s}_{Iij} \overset{\circ}{s}_{Iij} \right) &+ O(\varepsilon^3). \end{aligned} \quad (31)$$

At leading order, the equation (31) is the analog of the compatibility condition (11) for the nonacoustic part of governing equations.

The leading order terms of (24), (27) and (30) constitute the equations of linear acoustics. Further, by combining equations (24) and (30) one obtains:

$$\varepsilon \frac{\partial p_a}{\partial t_a} = \varepsilon \gamma \frac{\partial \rho_a}{\partial t_a} + O(\varepsilon^2), \quad (32)$$

which implies that

$$\varepsilon^2 p_a = \varepsilon^2 \gamma \rho_a + O(\varepsilon^3), \quad (33)$$

which is just the linearized isentropic relation between pressure and density. In (33), the additive $O(\varepsilon^2)$ function $f(t_I, x)$ arising from time integration of (32) was neglected by our assumption that there is no contribution from nonacoustic terms varying on the slow time scale to the acoustic equations at the orders of interest.

Now, for the sake of completeness, consider the equation of state (4). The two lowest nontrivial orders are:

$$\begin{aligned} \varepsilon^2(p_I + p_a) &= \frac{\varepsilon(\gamma - 1)}{\gamma} \left(\frac{\gamma}{\gamma - 1} \rho_t + T_t \right) + \\ &\frac{\varepsilon^2(\gamma - 1)}{\gamma} \left(\rho_t T_t + \rho_a \frac{\gamma}{\gamma - 1} + T_a \right) + O(\varepsilon^3), \end{aligned} \quad (34)$$

Again, using the same splitting procedure, one obtains the acoustic equation of state:

$$\varepsilon^2 p_a = \varepsilon^2 \left(\rho_a + \frac{(\gamma - 1)}{\gamma} T_a \right) + O(\varepsilon^3), \quad (35)$$

and nonacoustic equation of state:

$$\varepsilon^2 p_I = \varepsilon \left(\rho_t + \frac{(\gamma - 1)}{\gamma} T_t \right) + \frac{\varepsilon^2(\gamma - 1)}{\gamma} \rho_t T_t + O(\varepsilon^3). \quad (36)$$

The leading order part of nonacoustic equation of state (36) is just a Boussinesq relation. Substituting for ρ_a in (35) from (33):

$$\varepsilon^2 p_a = \varepsilon^2 T_a + O(\varepsilon^3), \quad (37)$$

which is a linearized isentropic relation between pressure and temperature. The relations (33) and (37) suggest that order ε^2 acoustic density and temperature should not be neglected in the corresponding asymptotic expansions, if one is interested in identification of the acoustic effects in compressible heat flux dominated flow.

It is instructive to contrast the above development with the HFDH limit of Zank & Matthaeus [28]. Even though the acoustic pressure p_a is included in the HFDH analysis, pressure fluctuations do not propagate at the first nontrivial order. The

reason is that ρ_a is neglected in HFDH in (23). If ρ_a is neglected, then from (23) it follows:

$$\frac{\partial}{\partial t_a} \left(\frac{\partial u_{tj}}{\partial x_j} + \frac{\partial u_{aj}}{\partial x_j} \right) + O(\varepsilon) = 0, \quad (38)$$

since Zank & Matthaeus assumed that ρ_t and \mathbf{u}_I do not vary on the fast time scale and that \mathbf{u}_I is divergence free. If one now takes the time derivative of the equation (29) noting that T_t and p_I do not vary on the acoustic time scale in HFDH, at leading order one gets (using (38)):

$$\frac{\partial^2 p_a}{\partial t_a^2} + O(\varepsilon) = 0 \quad (39)$$

rather than the wave equation for p_a . On the other hand, in the current analysis, the wave equation for acoustic pressure can be obtained by applying a similar procedure to the equations (27) and (30).

4.3. Consolidated equations. The decomposed equations derived in subsection 4.2 can be rewritten in a more useful form. In particular, we are interested in the nonacoustic components of the variables, which include both incompressible and thermal fluctuations. The nonacoustic parts of variables are therefore defined as follows:

$$\mathbf{u}_n = \mathbf{u}_I + \varepsilon \mathbf{u}_t, \quad (40)$$

$$p_n = 1 + \varepsilon^2 p_I, \quad (41)$$

$$T_n = \frac{\gamma}{\gamma - 1} + \varepsilon T_t, \quad (42)$$

$$\rho_n = 1 + \varepsilon \rho_t; \quad (43)$$

where subscript 'n' denotes the nonacoustic part. The nonacoustic equations are then:

$$\frac{\partial \rho_n}{\partial t} + \frac{\partial \rho_n u_{nj}}{\partial x_j} + O(\varepsilon^2) = 0, \quad (44)$$

$$\frac{\partial u_{ni}}{\partial t} + u_{nj} \frac{\partial u_{ni}}{\partial x_j} = -\frac{1}{\varepsilon^2 \rho_n} \frac{\partial p_n}{\partial x_i} + \frac{2}{Re \rho_n} \frac{\partial \mu_n s_{nij}}{\partial x_j} + O(\varepsilon^2), \quad (45)$$

$$\gamma \frac{\partial u_{nj}}{\partial x_j} = \frac{\gamma - 1}{Pr Re} \frac{\partial}{\partial x_k} \left(\mu_n \frac{\partial T_n}{\partial x_k} \right) + O(\varepsilon^2), \quad (46)$$

$$\rho_n T_n = \frac{\gamma}{\gamma - 1} + O(\varepsilon^2). \quad (47)$$

We would like to stress here that all the terms in the equations (44)–(47) vary on the slow time scale only. In particular, the time derivatives in (44) and (45) are slow derivatives. Also, it should be noted that there is an $O(\varepsilon^2)$ contribution to nonacoustic temperature and density, as a result of the linear response to the $O(\varepsilon^2)$ incompressible pressure. Such temperature and density variation is commonly referred to as pseudosound [17]. The incompressible pressure is not dynamic, and so pseudosound temperature and density do not play an important role in the dynamics of the nonacoustic part of the flow. They were therefore neglected in the system (44)–(47). That’s why equation (44) is written as valid to the order $O(\varepsilon^2)$. Note that the nonacoustic equations (44)–(47) closely resemble the equations of zero Mach number combustion (see, for example [15]).

Now, for convenience, the notation for the acoustic quantities is changed to be just the total quantity minus the corresponding nonacoustic parts, i.e.:

$$\mathbf{u}_s = \mathbf{u} - \mathbf{u}_n = \varepsilon \mathbf{u}_a, \quad (48)$$

$$p_s = p - p_n = \varepsilon^2 p_a, \quad (49)$$

$$T_s = T - T_n = \varepsilon^2 T_a, \quad (50)$$

$$\rho_s = \rho - \rho_n = \varepsilon^2 \rho_a; \quad (51)$$

where subscript ‘s’ denotes the acoustic part in the new notation. The corresponding set of governing equations for this acoustic part is:

$$\frac{\partial u_{si}}{\partial t} + u_{nj} \frac{\partial u_{si}}{\partial x_j} = -\frac{1}{\varepsilon^2 \rho_n} \frac{\partial p_s}{\partial x_i} + \frac{2}{Re \rho_n} \frac{\partial \mu_n^{\circ} s_{sij}}{\partial x_j} + O(\varepsilon^2), \quad (52)$$

$$\frac{\partial p_s}{\partial t} + u_{nj} \frac{\partial p_s}{\partial x_j} + \gamma p_n \frac{\partial u_{sj}}{\partial x_j} = \frac{\gamma - 1}{Pr Re} \frac{\partial}{\partial x_k} \left(\mu_n \frac{\partial T_s}{\partial x_k} \right) + O(\varepsilon^3), \quad (53)$$

$$p_s = \gamma \rho_s + O(\varepsilon^3), \quad (54)$$

$$p_s = T_s + O(\varepsilon^3). \quad (55)$$

The equations (52)–(55) are the equations for acoustic waves in the convective variable density medium defined by the nonacoustic field.

4.4. Governing equations in the case of a flow with a supersonic mean.

To study the compressibility effects in supersonic boundary layers, the acoustic and nonacoustic equations, derived above, must be extended to the case of a flow with a supersonic mean. The extension relies on the observation that the turbulence Mach number can be small even when the mean Mach number is large. A low Mach number asymptotic truncation can therefore be fruitfully applied to the turbulent fluctuations, even when it cannot be accurately applied to the mean. The details of this extended analysis are given in the Appendix A. The resulting equations for nonacoustic fluctuations are given by:

$$\frac{\partial \rho'_n}{\partial t} + \left(\frac{\partial \rho_n u_{nj}}{\partial x_j} \right)' + O(\varepsilon_t^2) = 0, \quad (56)$$

$$\frac{\partial u'_{ni}}{\partial t} + \left(u_{nj} \frac{\partial u_{ni}}{\partial x_j} \right)' = -\frac{1}{\varepsilon^2} \left(V_n \frac{\partial p_n}{\partial x_i} \right)' + \frac{2}{Re} \left(V_n \frac{\partial \mu_n \dot{s}_{nij}}{\partial x_j} \right)' + O(\varepsilon_t^2), \quad (57)$$

$$\begin{aligned} \gamma \bar{p} \frac{\partial u'_{nj}}{\partial x_j} &= \frac{\gamma - 1}{Pr Re} \frac{\partial}{\partial x_k} \left(\mu_n \frac{\partial T_n}{\partial x_k} \right)' + \\ &\frac{2(\gamma - 1)\varepsilon^2}{Re} \left(\mu'_n \bar{s}_{ij} \bar{s}_{ij} + 2\bar{\mu} \bar{s}_{ij} \dot{s}'_{nij} \right) + O(\varepsilon_t^2), \end{aligned} \quad (58)$$

$$\rho_n T_n = \frac{\gamma}{\gamma - 1} \bar{p} + O(\varepsilon_t^2). \quad (59)$$

For the acoustic fluctuations, we obtain:

$$\frac{\partial u'_{si}}{\partial t} + \left(u_{nj} \frac{\partial u'_{si}}{\partial x_j} \right)' = -\frac{1}{\varepsilon^2} \left(V_n \frac{\partial p_s}{\partial x_i} \right)' + O(\varepsilon_t^2), \quad (60)$$

$$\frac{\partial p'_s}{\partial t} + \left(u_{nj} \frac{\partial p'_s}{\partial x_j} \right)' + \gamma \left(p_n \frac{\partial u'_{sj}}{\partial x_j} \right)' = O(\varepsilon_t^3), \quad (61)$$

$$\rho'_s = \frac{p'_s}{(\gamma - 1)\bar{T}} + O(\varepsilon_t^3), \quad (62)$$

$$T'_s = \frac{p'_s}{\bar{\rho}} + O(\varepsilon_t^3). \quad (63)$$

These equations derived serve as the basis for the numerical decomposition of compressible boundary layer fluctuations discussed in the section 5.

5. NUMERICAL DECOMPOSITION.

To assist in the evaluation and characterization of compressibility effects in turbulent boundary layers, a numerical decomposition of turbulent fluctuations into

acoustic and nonacoustic parts is developed. The algorithm is based on low turbulence Mach number analysis discussed in A, and it allows the decomposed quantities to be determined from a compressible flow field. The description of the algorithm and its application to the boundary layer DNS data of Maeder *et al.* [14] with Ma equal to 3, 4.5 and 6 are described in this section.

One of the main goals of this decomposition is also to directly evaluate the ability of nonacoustic equations (56)–(59) to describe the dynamics of the nonacoustic fluctuating field in the compressible turbulent boundary layer. These equations are autonomous, i.e. they do not depend on the acoustic field, which depends on the details of the acoustic environment in which the boundary layer exists. So, if these equations apply, they are a valuable tool for the numerical modeling of compressible boundary layers.

It was noted when the governing equations (56)–(59) for nonacoustic fluctuations were derived in appendix A, that the time derivatives in these equations are slow time derivatives. However, by our assertion that the fast time derivative of the nonacoustic quantity is caused by acoustic convection and that these terms cancel at the orders of interest (see section A.1), these two terms can be included in the corresponding acoustic or nonacoustic governing equations and the validity of these equations will not change. This will eliminate the problem of acoustic convection term being unaccounted for later, during the verification of decomposition procedure in section 5.4. If these terms are included in the acoustic equations, as is usually done in acoustics, they will increase the error in the acoustic velocity equations by increasing the vortical part of the acoustic velocity time derivative (see section 5.5 for details). Alternatively, they are included in the nonacoustic governing equations. This has the effect of introducing a fast time derivative to the nonacoustic equations. In most cases (e.g. turbulence model development) we are only interested in the equations on the slow time scale, when (56)–(59) are valid. However, when verifying the decomposition in section 5.4, the total time derivative will be evaluated, making it important that the fast component is included. Resulting equations will be the same as (56)–(59) with acoustic convection terms added.

The derived governing equations for acoustic and nonacoustic fluctuations are only valid and decoupled to a finite order, because the assumptions made to separate them are invalid at higher orders. Consequently, there is no information about the higher order coupling terms, except that their magnitudes are small relatively to the magnitudes of the leading terms in the equations. No attempt will be made to assign these higher order coupling terms to either acoustic or nonacoustic equations. After the decomposition has been performed, these terms can be computed explicitly and their magnitudes can be compared to the magnitudes of the corresponding leading order terms to validate the consistency of the approach, and to assess the strength of the coupling.

The numerical decomposition is accomplished in stages, using the governing equations for acoustic and nonacoustic fluctuations. The approach is to construct fluctuating fields that will satisfy the acoustic and nonacoustic equations as closely as possible. The chain of calculations used for the decomposition is outlined below.

5.1. Temperature and density decomposition. The starting point of the decomposition is the determination of nonacoustic parts of temperature and density fluctuations. Since the pseudosound contribution to temperature and density was neglected in the equations (56)–(59), the nonacoustic temperature and density fluctuations for which (56)–(59) are valid are given by:

$$T'_n = T' - T'_s - T'_{ps}, \quad (64)$$

$$\rho'_n = \rho' - \rho'_s - \rho'_{ps}; \quad (65)$$

where subscript 'ps' denotes pseudosound fluctuations. Pseudosound fluctuations are defined to satisfy the linearized isentropic relations:

$$\rho'_{ps} = \frac{p'_I}{(\gamma - 1)\bar{T}} + O(\epsilon_t^3), \quad (66)$$

$$T'_{ps} = \frac{p'_I}{\bar{p}} + O(\epsilon_t^3); \quad (67)$$

analogous to the isentropic relations (62)–(63) for acoustic fluctuations, with the difference being that pseudosound fluctuations are just the linear response to the non-propagating incompressible pressure p'_I . Substituting for pseudosound and acoustic

fluctuations using (66)–(67) and (62)–(63) from (64) the final expressions for nonacoustic density and temperature fluctuations are obtained:

$$\rho'_n = \rho' - \frac{p'}{(\gamma - 1)\bar{T}}, \quad (68)$$

$$T'_n = T' - \frac{p'}{\bar{\rho}}. \quad (69)$$

So defined, nonacoustic temperature and density satisfy the nonacoustic equation of state (59) to the order required, by construction. The nonacoustic viscosity fluctuations may be obtained from Sutherland law (6) with $T_n = \bar{T} + T'_n$ as an argument:

$$\mu'_n = \left(\left(\frac{T_n}{\alpha} \right)^{\frac{3}{2}} \frac{1 + T_{su}/T_\infty}{T_n/\alpha + T_{su}/T_\infty} \right)'. \quad (70)$$

The nonacoustic specific volume fluctuations are defined as:

$$V'_n = \left(\frac{1}{\rho_n} \right)', \quad (71)$$

where $\rho_n = \bar{\rho} + \rho'_n$. Finally, the corresponding acoustic parts of density, temperature, viscosity and specific volume can be obtained by subtracting nonacoustic parts from the total fluctuations. This will include the pseudosound component of the fluctuations into the acoustic part. The pseudosound component can be separated from the acoustic part later, after the decomposition has been performed, if desired.

5.2. Velocity decomposition. The leading order nonacoustic pressure equation (58):

$$\gamma \bar{p} \frac{\partial u'_{nj}}{\partial x_j} = \frac{\gamma - 1}{Pr} \frac{\partial}{Re} \left(\mu_n \frac{\partial T_n}{\partial x_k} \right)' + \frac{2(\gamma - 1)\varepsilon^2}{Re} \left(\mu'_n \bar{s}_{ij} \bar{s}_{ij} + 2\bar{\mu} \bar{s}_{ij} s'_{nij} \right) \quad (72)$$

is just a relation between nonacoustic divergence, nonacoustic heat flux and leading order dissipation. Assuming that acoustic dissipation is negligible, the expression for nonacoustic divergence is:

$$\frac{\partial u'_{nj}}{\partial x_j} = \frac{\gamma - 1}{\gamma \bar{p} Pr} \frac{\partial}{Re} \left(\mu_n \frac{\partial T_n}{\partial x_k} \right)' + \frac{2(\gamma - 1)\varepsilon^2}{\gamma \bar{p} Re} \left(\mu'_n \bar{s}_{ij} \bar{s}_{ij} + 2\bar{\mu} \bar{s}_{ij} s'_{ij} \right), \quad (73)$$

where $T_n = \bar{T} + T'_n$, $\mu_n = \bar{\mu} + \mu'_n$, and nonacoustic temperature and viscosity fluctuations are obtained in 5.1. This allows the divergence of the nonacoustic

fluctuations to be determined. Since the divergence of nonacoustic fluctuating velocity is known, the acoustic divergence can be obtained by difference:

$$\frac{\partial u'_{sk}}{\partial x_k} = \frac{\partial u'_k}{\partial x_k} - \frac{\partial u'_{nk}}{\partial x_k}. \quad (74)$$

Now, apply the curl to the leading order part of the acoustic velocity equation (60), neglect mean gradients and note that the terms varying on the slow time scale don't contribute to the acoustic equations at the orders of interest. The result is:

$$\left(\frac{\partial}{\partial t} + (\bar{\mathbf{u}} \cdot \nabla) \right) (\nabla \times \mathbf{u}'_s) = 0, \quad (75)$$

which is the statement that leading order acoustic vorticity is preserved in a frame moving with the mean flow. So, the leading order acoustic velocity is irrotational at all times, given that it was irrotational at time $t = 0$. An acoustic velocity potential φ_s can therefore be introduced to obtain a Poisson equation for φ_s from (74):

$$\Delta \varphi_s = \frac{\partial u'_{sk}}{\partial x_k}. \quad (76)$$

Note that in the presence of strong mean gradients the acoustic velocity will not be irrotational, so (76) will not be valid close to the wall in the boundary layer.

One also needs to specify boundary conditions for φ_s . Only the boundary conditions at the wall and outer boundary are needed, since in the simulation data being decomposed, periodic boundary conditions are imposed in stream-wise and span-wise directions. At the wall and outer boundary ($z = 0$ and z_{max}):

$$\left. \frac{\partial \varphi_s}{\partial z} \right|_{z=0, z_{max}} = u'_3 \Big|_{z=0, z_{max}}. \quad (77)$$

At the outer boundary, (77) reflects the fact that only acoustic velocity fluctuations are expected outside the boundary layer. At the wall, (77) is just the no flow through condition for acoustic and, consequently, for nonacoustic velocity fluctuations. Since diffusion of the acoustic field is neglected in the acoustic equations, the no-slip condition cannot be imposed on the acoustic velocity at the wall. This implies that the tangential nonacoustic velocity will also be nonzero at the wall. After solving (76) with (77) for φ_s , one may calculate acoustic fluctuating velocity from its potential and nonacoustic velocity fluctuations by difference, thus completing the decomposition of the velocity.

5.3. Pressure decomposition. To decompose the pressure fluctuations we will seek nonacoustic pressure that satisfies the divergence constraint, as is done in incompressible hydrodynamics, the difference being that in our case the divergence is not zero, but given by (73). Taking the divergence of the nonacoustic velocity equation (57) one obtains:

$$\begin{aligned} \frac{\partial^2 p'_n}{\partial x_i \partial x_i} + \frac{1}{\bar{V}} \frac{\partial \bar{V}}{\partial x_i} \frac{\partial p'_n}{\partial x_i} = \\ - \frac{\gamma Ma^2}{\bar{V}} \left(\frac{\partial}{\partial t} \frac{\partial u'_{ni}}{\partial x_i} + \frac{\partial}{\partial x_i} \left(u_j \frac{\partial u'_{ni}}{\partial x_j} - \frac{1}{\gamma Ma^2} \left(V'_n \frac{\partial \bar{p}}{\partial x_i} + V'_n \frac{\partial p'_n}{\partial x_i} \right) \right) \right)'. \end{aligned} \quad (78)$$

The equation (78) is nonlinear and can be solved by iteration. At each iteration, essentially a Poisson equation for p'_n is solved with nonacoustic specific volume on the right hand side of (78) computed with p'_n from previous iteration, starting with total pressure fluctuations p' as initial guess for nonacoustic pressure. To compute the time derivative of the nonacoustic divergence, which is part of the right hand side of (78), we take the time derivative of (73) noting that the nonacoustic viscosity μ_n is a function of T_n only when computing the time derivative of viscosity. The Poisson equation (78), when solved with appropriate boundary conditions, gives the nonacoustic pressure fluctuation field.

The most straightforward boundary condition for p'_n at the wall is obtained in the same way that pressure boundary conditions are obtained for incompressible hydrodynamics; by evaluating the wall-normal nonacoustic fluctuating velocity equation given by (from (57)):

$$\frac{\partial u'_{n3}}{\partial t} + \left(u_j \frac{\partial u'_{n3}}{\partial x_j} \right)' = - \frac{1}{\gamma Ma^2} \left(V'_n \frac{\partial p'_n}{\partial x_3} \right)' + \frac{2}{Re} \left(V'_n \frac{\partial \mu_n \hat{s}_{n3j}}{\partial x_j} \right)' \quad (79)$$

at the wall. The first term of the left hand side of (79) is zero at the wall because of the boundary condition (77), and the second term is zero at the wall since the velocity is zero at the wall. The boundary condition for nonacoustic pressure at the wall is given by:

$$\left. \frac{\partial p'_n}{\partial z} \right|_{z=0} = \frac{2}{Re} \left(\frac{\partial \mu_n \hat{s}_{n3j}}{\partial x_j} \right)' \Big|_{z=0}. \quad (80)$$

This boundary condition is valid provided the wall-normal momentum equation is satisfied at the wall. Analytically, it is, but in the numerical simulations, the governing equations are not imposed on the boundaries, instead, the boundary conditions are imposed. This leads to an anomaly, which is discussed in detail in subsection 5.5.

The outer boundary condition is easier, because p'_n is exponentially small there:

$$p'_n \Big|_{z=z_{max}} = 0. \quad (81)$$

After p'_n has been obtained, it can be subtracted from total pressure fluctuations to get acoustic pressure fluctuations. Pseudosound part of temperature and density can now be separated from the acoustic part using the isentropic relations discussed in section 5.1 if desired.

This step completes the procedure used for the decomposition of a turbulent fluctuating field into nonacoustic and acoustic part. It should be noted that in the homogeneous case, by imposing the vorticity free and isentropy conditions described above on the acoustic quantities, one obtains fields that do indeed propagate as acoustic waves.

5.4. Verification of decomposition.

5.4.1. Acoustic-nonacoustic pressure correlation check. Asymptotically, acoustic and nonacoustic pressure fluctuations are of the same leading order. So, in principle, they can be strongly correlated. To check that this is not the case, acoustic-nonacoustic pressure correlation coefficient is computed and presented in figure 3. The correlation between acoustic and nonacoustic pressure fluctuations is weak, so from this point of view the decomposition is producing meaningful results.

5.4.2. Weakly compressible nonacoustic governing equations check. While developing the decomposition procedure, our goal was to obtain nonacoustic variables satisfying derived weakly compressible governing equations (56)–(57) as close as possible. The last two of these equations are satisfied by construction, so the validity of the remaining two can be checked. We can compute the time derivative of a given nonacoustic variable β_n from the nonacoustic governing equation. Also, this

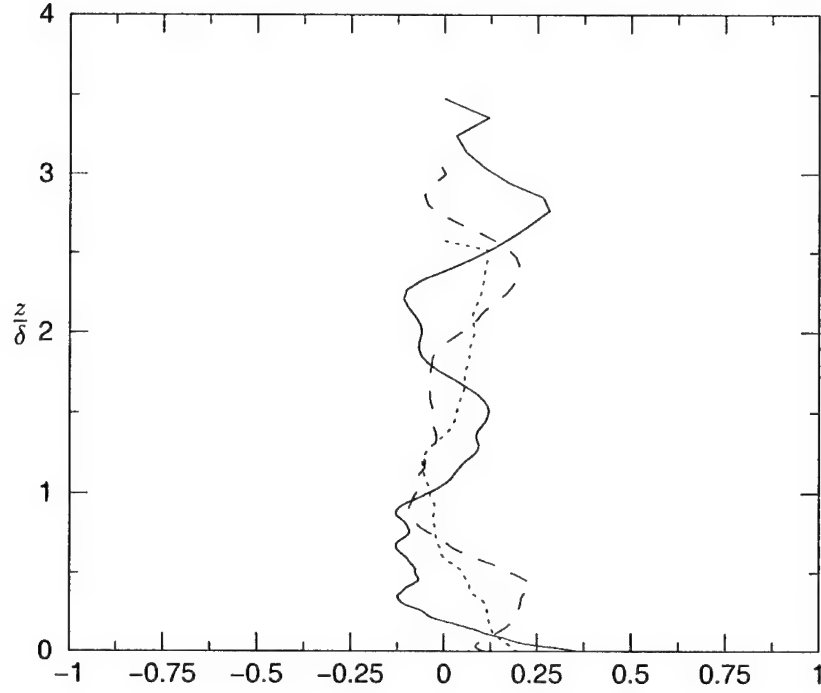


FIGURE 3. The profiles of acoustic-nonacoustic pressure correlation coefficient $R_{p'_n, p'_n}$ for: $Ma = 3$ (—), $Ma = 4.5$ (·····), $Ma = 6$ (---).

time derivative can be determined by decomposing two fields separated in time by small Δt and computing the time derivative as $(\beta_n(t + \Delta t) - \beta_n(t))/\Delta t$. When the time derivative of nonacoustic variables is computed this way, it includes the effect of convection by acoustic velocity (see section 5). Therefore, this time derivative will be compared to the one from the governing equation with the acoustic convection included. If the decomposition is valid, then the difference between these two estimates of the time derivative of β_n will be small.

The governing equations for acoustic and nonacoustic fluctuations are only valid to a certain order. For the velocity equation this is the order of coupling terms, at which the assumptions made to separate the acoustic and nonacoustic equations are no longer valid (see section 5). For the density equation, this is the order of the explicitly neglected pseudosound terms. The sum of the terms at these orders have been computed to provide an estimate of the error committed by neglecting them.

The magnitude of these terms can also serve as a measure of how well the nonacoustic equations can predict the evolution of turbulent flow. Of course, the higher order terms are computed from the variables obtained by the decomposition, so this measure will also depend on the validity of the decomposition. The performance of the derived nonacoustic equations can be assessed independently by performing a DNS simulation of the flow governed by these equations and comparing the results to the DNS of a fully compressible flow. This validation, however, is beyond the scope of the current paper.

The r.m.s. profiles of the time derivatives of nonacoustic velocity u'_n computed both ways, the difference between them (error), the relative error and the sum of higher order terms in this equation are presented in figure 4. The error is of the same order as the sum of higher order terms, i.e. the error caused by the approximations made in the decomposition is of the same magnitude as the intrinsic error present in the equations due to the neglect of higher order terms. The relative error is very small except very close to the wall ($z^+ < 30$), where it becomes as large as 20 percent at the wall. This is expected, since the assumptions made during the decomposition become invalid close to the wall.

The r.m.s. profiles of the time derivatives for nonacoustic density ρ'_n and the errors are presented in figure 5. The behavior of the error in the nonacoustic density equation is completely analogous to that of the nonacoustic velocity.

It can also be relevant to compare the errors in the time derivatives to the mean convective time derivatives $D/Dt = d/dt + \bar{u}_j d/dx_j$. The mean convective time derivatives in our case are factor of 15 smaller than corresponding time derivatives. The errors in the nonacoustic equations, when compared to mean convective derivatives, are still relatively small.

5.4.3. Acoustic velocity governing equation check. Here the errors in the acoustic velocity equation (60) are presented. The order of validity of the acoustic velocity equation is the same as that for the nonacoustic velocity and it is not influenced directly by the neglect of pseudosound. The profiles of time derivatives and errors for acoustic equation are presented in figure 6. The relative error in this equation

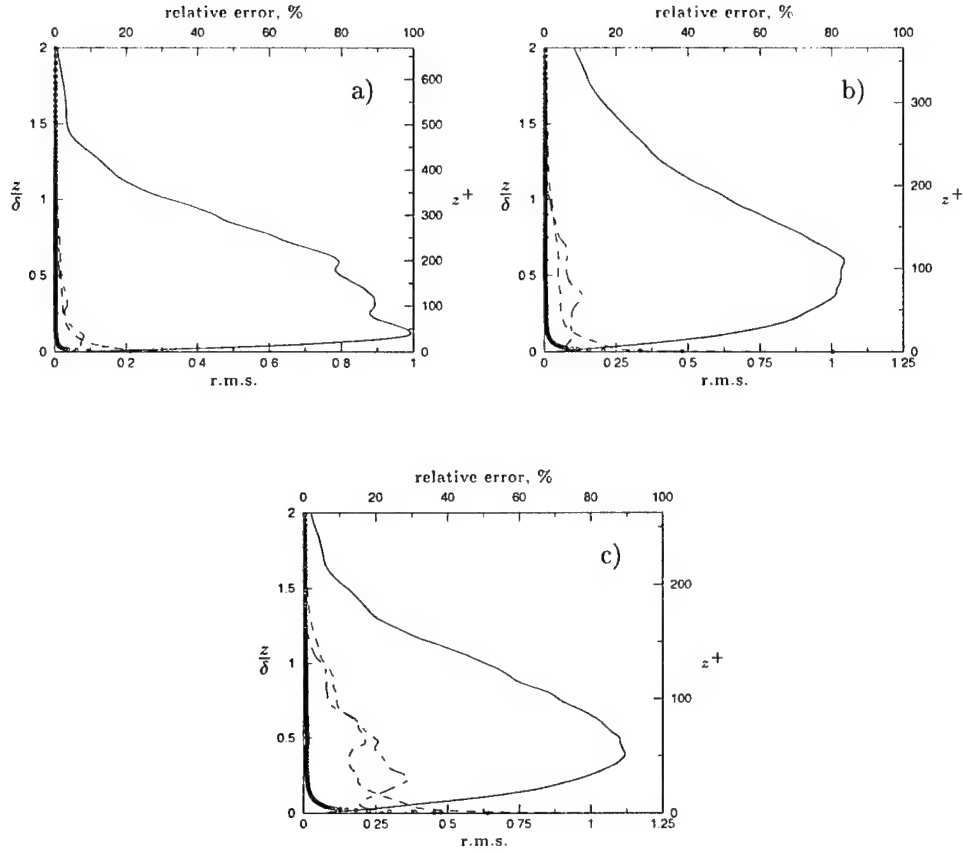


FIGURE 4. The r.m.s. profiles of magnitudes of the time derivatives of nonacoustic velocity fluctuations u'_n calculated from: the governing equation (—), two subsequent in time data fields (·····), difference between them $\times 20$ (---), magnitude of higher order terms $\times 20$ (-·-·-) and relative error ($\circ \circ \circ \circ$) for: a) $Ma = 3$, b) $Ma = 4.5$, c) $Ma = 6$.

is about 20–30% in the boundary layer, but it is very close to the sum of the higher order terms throughout most of the boundary layer. The error is also approximately the same as the error in the nonacoustic equation. Relative error in the acoustic equation is so large simply because the acoustic time derivative is factor 10 to 20 smaller than the nonacoustic time derivative. Through most of the boundary layer, the errors in both the acoustic and nonacoustic equations appear to be inherent

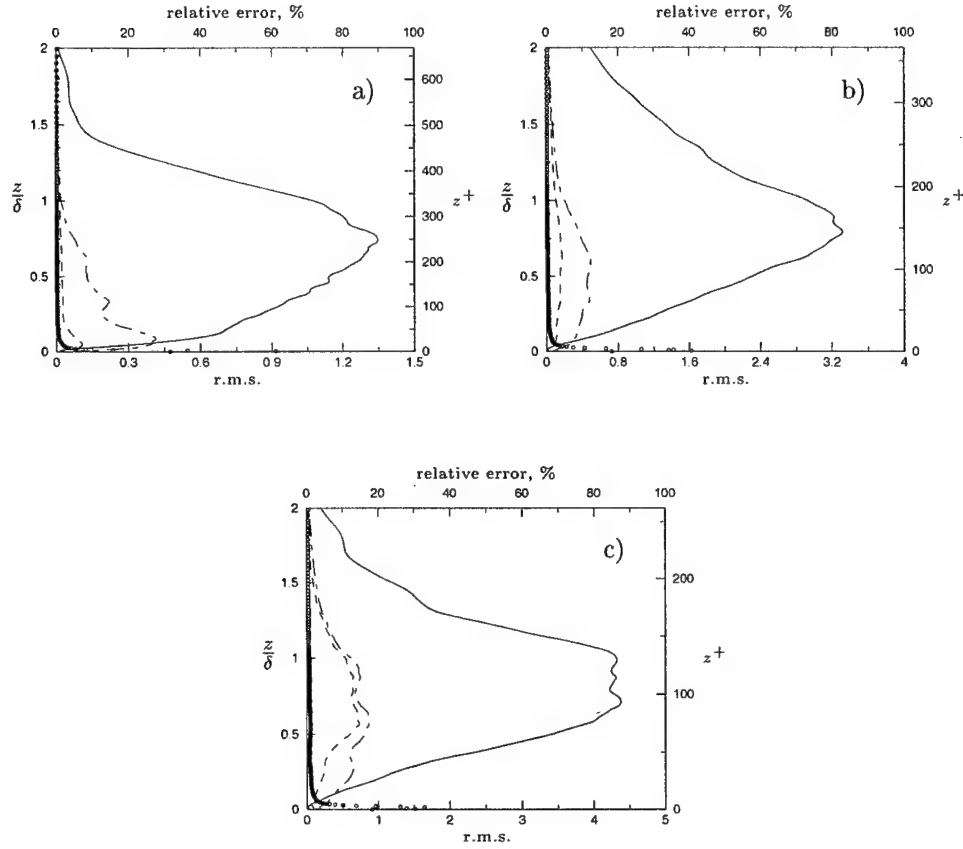


FIGURE 5. The r.m.s. profiles of the time derivatives of nonacoustic density fluctuations ρ'_n calculated from: the governing equation (—), two subsequent in time data fields (.....), difference between them $\times 20$ (---), magnitude of higher order terms $\times 20$ (-.-.-) and relative error (oooo) for: a) $Ma = 3$, b) $Ma = 4.5$, c) $Ma = 6$.

to the splitting of the equation, rather than shortcomings of the decomposition procedure, since these errors are nearly the same as the neglected higher order terms.

5.5. Sources of error in the decomposition. In summary, there are two major sources of error in the decomposition. The first, and probably the most important,

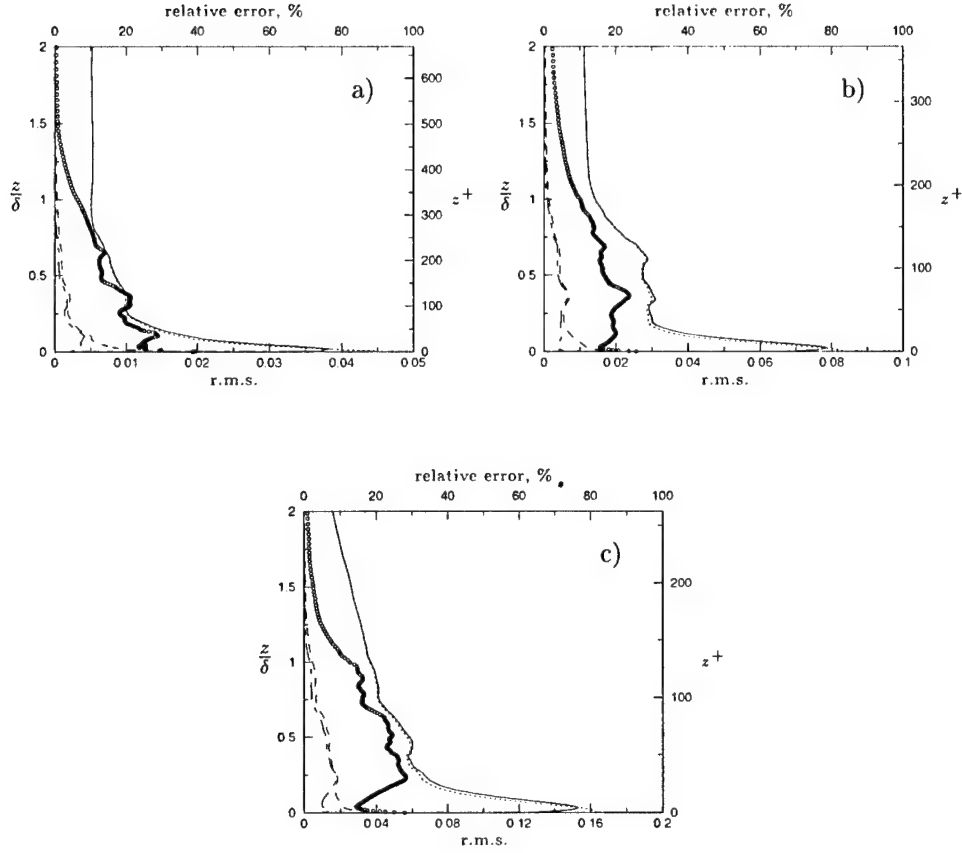


FIGURE 6. The r.m.s. profiles of magnitudes of the time derivatives of acoustic velocity fluctuations u'_s calculated from: the governing equation (—), two subsequent in time data fields (·····), difference between them (---), magnitude of higher order terms (-·-·-) and relative error (○○○○) for: a) $Ma = 3$, b) $Ma = 4.5$, c) $Ma = 6$.

is the neglect of the mean flow gradients when asserting that acoustic velocity is irrotational, and acoustic fluctuations are isentropic. Because of this, the time derivative of acoustic velocity u_s obtained from two decomposed consequent in time data fields will be irrotational as well. It is clear, however, that the time derivative of u_s as determined from the governing equation (60) is not irrotational. Vorticity is generated by interaction of the acoustic fluctuations with the mean gradients, and

this is not accounted for in the decomposition. This inconsistency is responsible for the elevated error in both the acoustic and nonacoustic velocity equations near the wall.

The second main source of decomposition error is an anomaly in the DNS data arising from the imposition of boundary conditions in the simulations. The decomposition described above poses strict requirements on the DNS data used. In particular, to avoid erroneous boundary conditions for the nonacoustic pressure p'_n at the wall, which is obtained from the governing equation for the wall-normal component of fluctuating nonacoustic velocity, we require that the flow variables satisfy the boundary conditions used in the simulations, as well as the governing equations at the wall.

However, because of the nature of the numerical methods used to generate the data and the way the boundary conditions were posed in the simulations, the governing equations are not satisfied at the wall in the DNS data. To overcome this problem, temperature, pressure and density were adjusted slightly to satisfy the governing equations at the wall. The boundary values of pressure, temperature and density were left unchanged by this data correction, only the values at the point next to the boundary were modified. A detailed description of the data adjustment procedure is given in appendix B.

The efficacy of the data adjustment can be evaluated by examining the time derivatives of the nonacoustic pressure (figure 7). The $Ma = 4.5$ case is presented since it has the biggest x-y computational domain, which will make the impact of errors in determining the pressure at the wall the largest. Here the r.m.s. of the p'_n time derivative is shown as determined by decomposing two fields separated by a small time increment. When the anomaly is not removed by the data adjustment, there is a large difference between this time evolution and that obtained from the p'_n governing equation, but the data adjustment eliminates most of this discrepancy. Note however, that a data adjustment of this sort is undesirable; first because it is artificial and will affect the subsequent evolution of the field, and second, because even after the data adjustment there is no guarantee that the anomaly has

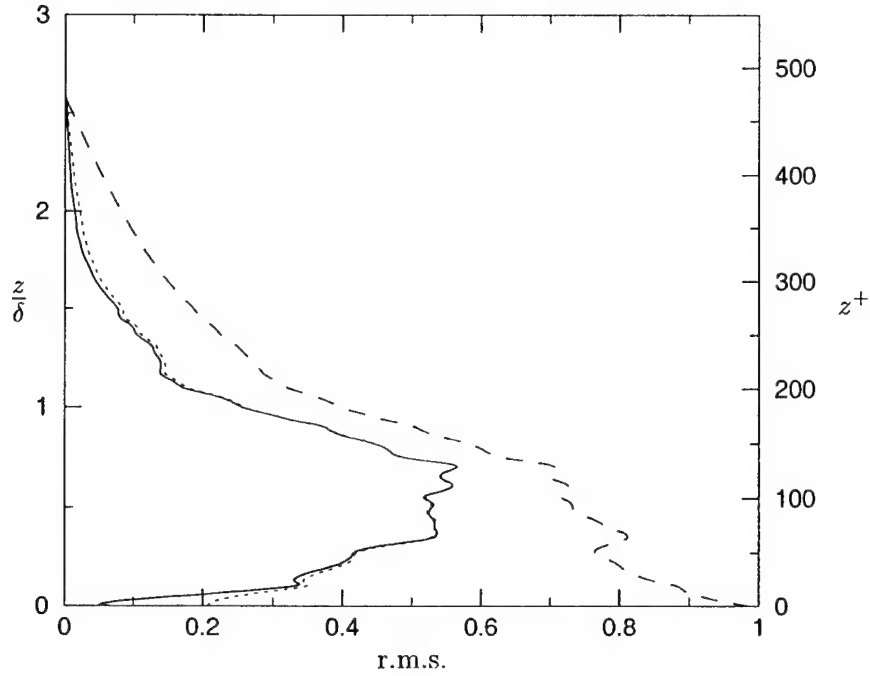


FIGURE 7. The r.m.s. profiles of time derivatives of nonacoustic pressure p'_n computed from governing equation (—) (provided for reference) and from two subsequent in time data fields before (---) and after (·····) the data adjustment ($Ma = 4.5$).

been eliminated completely. So, DNS data that doesn't suffer from this problem is needed.

The nonacoustic fluctuations defined by the decomposition satisfy the prescribed governing equations. Also, the magnitude of higher order terms, reflecting the intrinsic level of error introduced by use of weakly compressible equations, is small. This supports the claim that the nonacoustic flow evolution is autonomous, i.e. it does not depend on the acoustic field, and that weakly compressible governing equations predict well the evolution of turbulent nonacoustic field. The elevated error near the wall in the governing equation for acoustic velocity is primarily due to the decomposition deficiencies discussed above, not the higher order terms, or the equation itself. Efforts are under way to improve the decomposition.

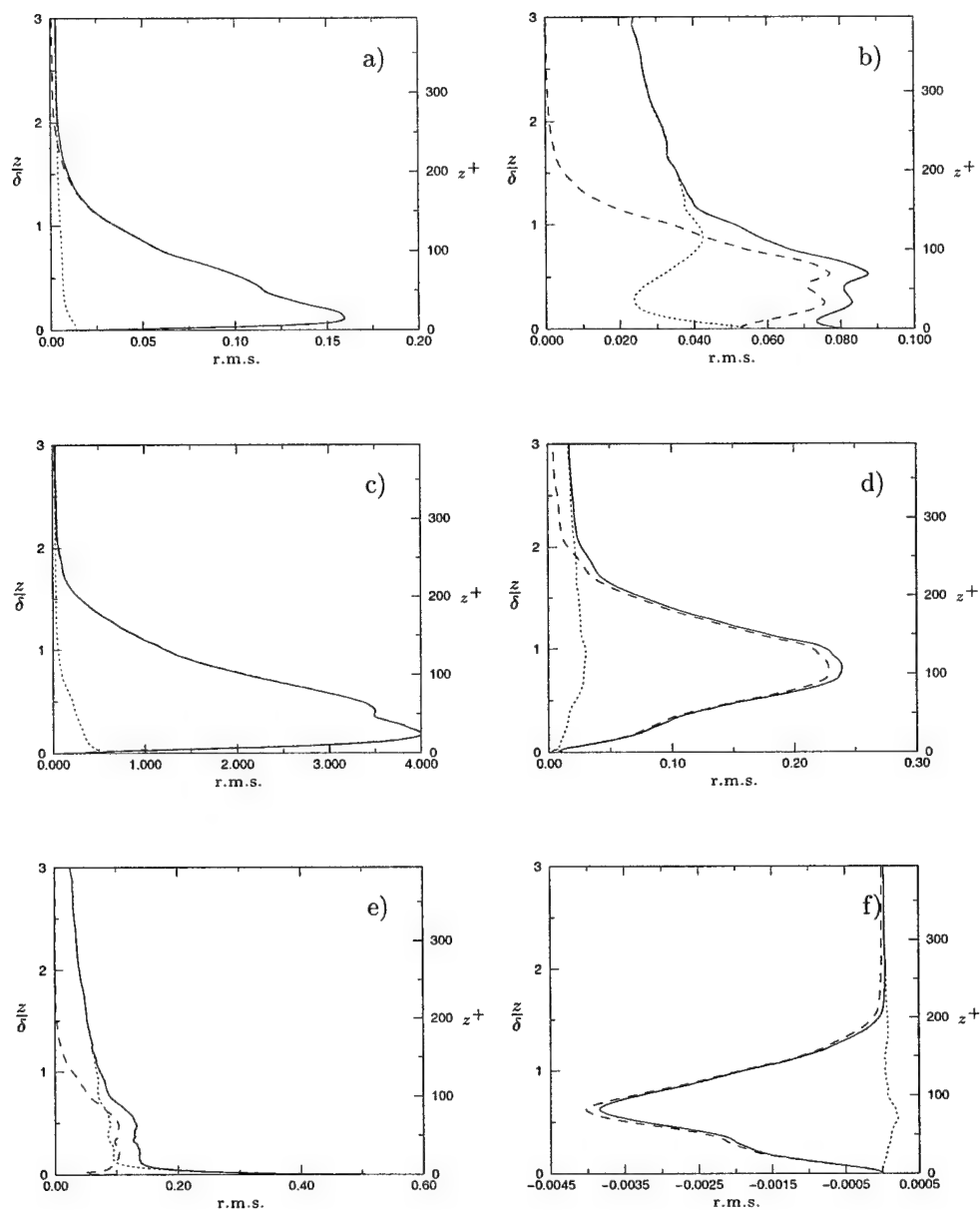


FIGURE 8. The r.m.s. profiles of the total (—), acoustic (·····) and nonacoustic (---) fluctuations of: a) velocity, b) pressure, c) temperature, d) density, e) velocity divergence. In f) the total (—), acoustic (·····) and nonacoustic (---) Reynolds shear stress is shown ($Ma = 6$).

6. DISCUSSION AND CONCLUSIONS.

The numerical investigation of the DNS data of Maeder *et al.* [14] revealed the presence of substantial acoustic fluctuations when an application of HFDH asymptotics derived by Zank & Matthaeus [28] to the compressible turbulent boundary layer fluctuations was attempted. To study the role these acoustic fluctuations play in the evolution of the nonacoustic field, the governing equations for the acoustic and nonacoustic parts of the flow were derived in the limit of small Mach number. These equations were then adapted to the case of small turbulence Mach number; to serve as a basis of the numerical decomposition proposed for splitting the turbulent boundary layer fluctuations into nonacoustic and acoustic parts. The numerical decomposition procedure is consistent, in the sense that the resulting acoustic fields satisfy the properties assumed for their derivation, to the order expected.

6.1. Decomposed quantities. The r.m.s. profiles of the acoustic and nonacoustic fluctuations obtained by applying the decomposition procedure to the DNS data are shown in figure 8.

Recall the ordering of acoustic and nonacoustic fluctuations postulated in subsection 4.1 (equations (14)–(17)), in which acoustic fluctuations are an order smaller than the nonacoustic fluctuations, except for the pressure and dilatation. The r.m.s. profiles shown in figure 8 are consistent with this ordering throughout the boundary layer. But, outside the boundary layer ($z/\delta > 2$), acoustic fluctuations dominate as expected. It is remarkable that this ordering appears valid even at $Ma = 6$, which is beyond the accepted limits of validity for weakly compressible approximations such as Morkovin’s hypothesis. The total $(\overline{\rho u w} - \bar{\rho} \bar{u} \bar{w})$, nonacoustic $(\overline{\rho_n u_n w_n} - \bar{\rho} \bar{u} \bar{w})$ Reynolds shear stress and the difference between them associated with acoustics are also shown in figure 8, part f). The acoustic contribution to Reynolds shear stress is very small, even at $Ma = 6$. So using the nonacoustic equations to predict Reynolds stress in a turbulence model (say) is a viable approach.

6.2. Nonacoustic flow governing equations. The equations for nonacoustic fluctuations (56)–(59) closely resemble the equations derived in HFDH limit, however in this case these equations govern only the evolution of the nonacoustic part

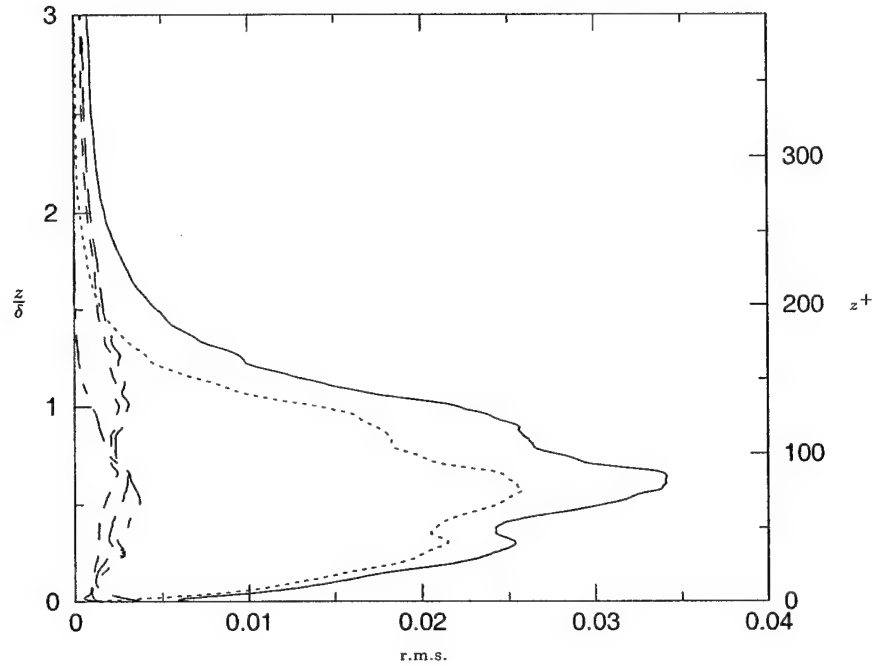


FIGURE 9. The a) r.m.s. profiles of the sum of higher order terms (—) and of the most significant of the higher order terms in density equation: $u'_{nj} \frac{\partial \rho'_s}{\partial x_j}$ (.....), $u'_{sj} \frac{\partial \rho'_s}{\partial x_j}$ (----), $\rho'_s \frac{\partial u'_{sk}}{\partial x_k}$ (---) and $\rho'_s \frac{\partial u'_{nk}}{\partial x_k}$ (-.-.-) ($Ma = 6$).

of the flow. Of these equations, the compatibility condition (58) and the equation of state (59) are satisfied by construction of decomposition procedure (see subsections 5.2 and 5.1), while the validity of the velocity and density equations (56) and (57) was checked (see 5.4.2). The results indicate that these equations predict the evolution of the nonacoustic field very well, except near the wall, where the error appears to be caused by the deficiencies of the decomposition procedure for strong inhomogeneities. The validity of these equations at high Ma is of great interest since they can be used in turbulence model development.

6.3. Higher order terms. The sums of higher order terms in the fluctuating velocity and density equations were presented in figures 4, 5 and 6. They are also shown in figures 9 and 10 for the highest Ma data studied ($Ma = 6$), along with the largest contributing terms. There are three classes of higher order terms in

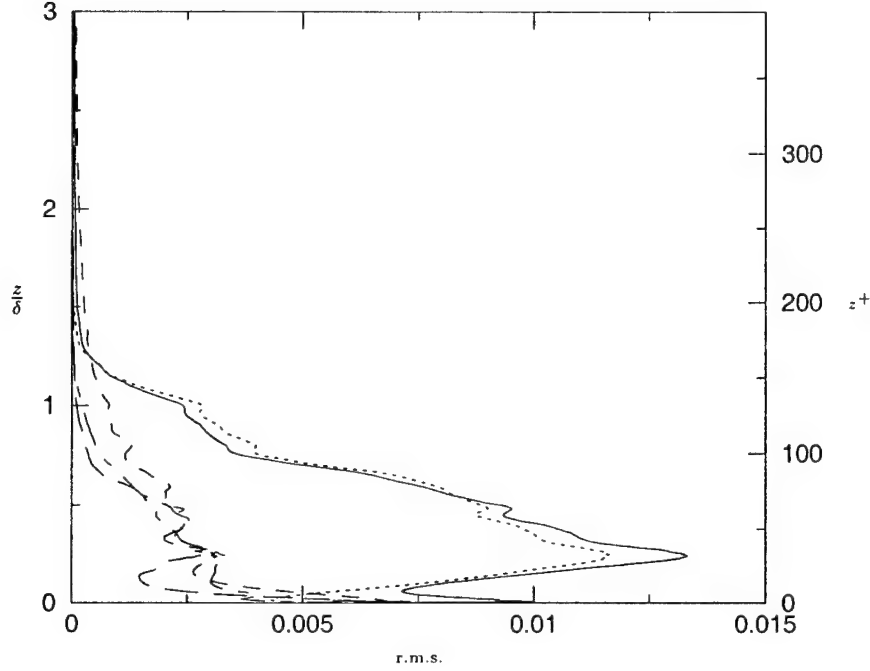


FIGURE 10. The a) r.m.s. profiles of the sum of higher order terms (—) and of the most significant of the higher order terms in velocity equation: $V'_s \frac{\partial p'_n}{\partial x_i}$ (.....), $V'_s \frac{\partial p'_s}{\partial x_i}$ (---), $\frac{2}{Re} V_n \frac{\partial}{\partial x_j} (\mu_n s'_{sij})$ (— · —) and $\frac{2}{Re} V'_s \frac{\partial}{\partial x_j} (\mu_n s_{nij})$ (- · - · -) ($Ma = 6$).

the fluctuating equations, which were not included in either the acoustic or the nonacoustic governing equations. They are:

1. **The neglected terms:** The convection of acoustic density with nonacoustic velocity $u'_{nj} \frac{\partial \rho_s}{\partial x_j}$ in the density equation and the viscous diffusion of acoustic velocity $\frac{2}{Re} V_n \frac{\partial}{\partial x_j} (\mu_n s'_{sij})$ in the velocity equation belong to this class. Asymptotically, these terms are the most significant of the higher order terms, so they should dominate the sum of higher order terms. This is the case for density equation. The viscous diffusion term, however is smaller than other higher order terms in the velocity equation, which is consistent with

the assumption of acoustic diffusion being negligible. Also, since the governing equations are decoupled at this order, these terms clearly belong to the acoustic equations and do not directly effect the nonacoustic fluctuations.

2. **Nonlinear acoustic terms:** There are relatively significant higher order nonlinear acoustic terms $u'_{sj} \frac{\partial \rho'_s}{\partial x_j}$ and $\rho'_s \frac{\partial u'_{sk}}{\partial x_k}$ in the density equation and $V'_s \frac{\partial p'_s}{\partial x_i}$ in the velocity equation. Asymptotically, these are the same order as the coupling terms discussed below and their actual magnitudes are smaller than the dominant terms.
3. **Coupling terms:** These are the higher order terms involving acoustic and nonacoustic variables that are present at the order where the governing equations are no longer decoupled. As mentioned in subsection 5, there is no information about these higher order terms, except for the fact that their magnitudes are small relatively to the magnitudes of the leading terms in the equations. They cannot be assigned to either nonacoustic or acoustic equations. These are the true coupling terms that couple the acoustic and nonacoustic equations. In the density equation, the most significant coupling term is the interaction of acoustic density with nonacoustic divergence $\rho'_s \frac{\partial u'_{nk}}{\partial x_k}$, which is of the same magnitude as the nonlinear acoustic terms discussed in item 2, and smaller than the dominant term.

In the velocity equation, there are two coupling terms that are most significant: the nonacoustic pressure gradient term $V'_s \frac{\partial p'_n}{\partial x}$ and the viscous diffusion term $\frac{2}{Re} V'_s \frac{\partial}{\partial x_j} (\mu_n s_{nij})$, both caused by acoustic density variation. The nonacoustic pressure gradient term is asymptotically of the same order as the nonlinear term involving acoustic pressure, discussed in item 2. Its actual magnitude is larger than one of the nonlinear term. This is caused by the difference in the magnitude of acoustic and nonacoustic pressure in the boundary layer. The nonacoustic pressure gradient term is dominating the sum of higher order terms in the velocity equation, and its relative magnitude is about 20–30% of acoustic velocity time derivative (see figure 6).

In judging the importance of the neglected terms plotted in figures 9 and 10, it is important to recall the magnitudes of the lowest order terms in the equations as shown in figures 4 and 5. Particularly, the true coupling terms representing interaction of acoustics with nonacoustic field as discussed in item 3 above are quite small indeed.

6.4. Conclusions. The results presented in this paper suggest that the nonacoustic equations (56)–(59) are a valid description of the evolution of nonacoustic fluctuations in a turbulent boundary layer, up to at least $Ma = 6$. Since these equations are autonomous (i.e. do not include acoustic terms) they could be used as a surrogate for the compressible Navier-Stokes equations, either for model development or as a basis for numerical simulation. This would yield a very good description of the turbulent fluctuations and their effect on the boundary layer (e.g. through the Reynolds stress). Another important implication is that the nonacoustic (i.e. turbulent) fluctuations are insensitive to the acoustic fields present in the flow under consideration. The details of these acoustic fields depend on the acoustic environment in which the boundary layer exists. Insensitivity of turbulence to acoustics is necessary if boundary layer turbulence at this Mach number is to have a meaningful canonical state. Otherwise, the structure of the turbulence will depend on the details of the acoustic environment, that is the characteristics of the flow or geometry far from the boundary layer.

Our understanding of the lack of coupling between acoustic and non-acoustic fields in the boundary layer must be qualified by the break-down of the analysis very near the wall where the mean gradients are large. Also, there is a potential coupling mechanism right at the wall since the no-slip boundary condition applies to the sum of nonacoustic and acoustic fields, but not necessarily to the fields individually.

This research was supported by AFOSR under grant F49620-97-1-0089. The authors are grateful to Drs. T. Maeder and N. Adams for their generosity and assistance in the use of their boundary layer data, and to Prof. M. Short for insightful comments on a draft of this paper.

APPENDIX A. EXTENSION OF LOW MACH NUMBER ASYMPTOTIC ANALYSIS TO A FLOW WITH SUPERSONIC MEAN.

In this appendix, the extension of the low Mach number asymptotic analysis of section 4 to the case of the supersonic boundary layer with moderately large free stream Mach number (up to say $Ma = 6$) is discussed. Despite the supersonic free stream Mach number, if the characteristic turbulence Mach number $Ma_t = u_f/c_\infty$ (where u_f is characteristic fluctuating velocity) of this flow is relatively small, the turbulent fluctuations can fruitfully be considered to be weakly compressible. In such a case, an analysis analogous to that of section 4 can be applied to the fluctuating equations, with the small parameter based on the turbulence Mach number.

There is a subtlety associated with the application of the asymptotic analysis of section 4 to the fluctuations in a turbulent boundary layer. The difficulty occurs in defining the zero Mach number limit being considered. The parameter describing mean flow compressibility is the free stream Mach number, while the compressibility of turbulence is parametrized by the turbulence Mach number. So, the question arises as to which of the two Mach numbers, or both of them should be used as a small parameter in the asymptotic analysis for weakly compressible turbulence.

In a flow with nonzero mean velocity, such as a boundary layer, the ratio of characteristic turbulence Mach number to the characteristic mean flow Mach number is equal to the ratio of characteristic velocities, i.e. $Ma_t/Ma = u_f/U_\infty$. Therefore, considering the limit as the turbulence Mach number going to zero, while the free stream Mach number is finite (as in Ristorcelli [21]), will require turbulent fluctuations themselves to go to zero. However, the only meaningful limit is when ratio u_f/U_∞ stays finite, requiring both free stream and turbulence Mach numbers to go to zero together.

For the case under consideration, the mean flow is supersonic, while the turbulence Mach number is much less the one. In this case we may expect an asymptotic truncation to be still a good approximation for the fluctuations, but not for the mean. Alternatively, we could dispense with formal asymptotics and consider the

development to be an order of magnitude analysis based on the observed magnitudes of fluctuations in the DNS data.

One more point worth discussing here is the dependence of the temperature on the small parameter. It is known that for a boundary layer with an adiabatic wall (or an isothermal wall with temperature set to the adiabatic recovery temperature as in the data of Maeder [14]), the mean temperature variation and the temperature fluctuations go to zero like Ma^2 (see [24]). This is inconsistent with the temperature scaling postulated for thermal fluctuations in 4.1, and with the observations of relative magnitudes in the DNS data (see section 3). One way to overcome this inconsistency is to consider a different limit in which both free stream and fluctuating Mach numbers go to zero, but in which the mean temperature and density variations across the boundary layer scale like Ma rather than Ma^2 . For example, the wall thermal boundary condition could vary with Ma to accomplish this, so that the wall is adiabatic or at the recovery temperature only for the Mach number being analyzed.

Regardless of the interpretation of the asymptotic limit, the analysis analogous to that of section 4 can be applied to the turbulent fluctuations, with small parameter being the turbulence Mach number. No scaling assumptions will be made regarding the mean quantities, since the applicability of an asymptotic analysis to the supersonic mean flow is questionable for the Mach numbers of interest. Instead, the mean quantities will be considered order one. To perform the analysis, the governing equations (7)–(10) for turbulent fluctuations need to be rescaled with u_f as characteristic velocity.

A.1. Scaling. As in section 4.1 the analysis is begun by postulating the scaling of the flow variables with the parameter $\varepsilon_t = \sqrt{\gamma}Ma_t$:

$$\mathbf{u} = \frac{\varepsilon}{\varepsilon_t} \bar{\mathbf{u}} + \mathbf{u}'_I + \varepsilon_t(\mathbf{u}'_t + \mathbf{u}'_a), \quad (82)$$

$$p = \bar{p} + \varepsilon_t^2(p'_I + p'_a), \quad (83)$$

$$T = \bar{T} + \varepsilon_t T'_I + \varepsilon_t^2 T'_a, \quad (84)$$

$$\rho = \bar{\rho} + \varepsilon_t \rho'_I + \varepsilon_t^2 \rho'_a; \quad (85)$$

The mean velocity scale is kept u_∞ , so a factor $\varepsilon/\varepsilon_t = Ma/Ma_t = u_\infty/u_f$ appears in front of \bar{u} in (82). Note that in this analysis $\varepsilon = \sqrt{\gamma}Ma$ is not a small parameter, it is of order one. The fluctuations are treated analogous to section 4.1, i.e. only the leading order scaling is specified. The viscosity and specific volume can be written similarly:

$$\mu = \bar{\mu} + \varepsilon_t \mu'_t + \varepsilon_t^2 \mu'_a, \quad (86)$$

$$V = \bar{V} + \varepsilon_t V'_t + \varepsilon_t^2 V'_a; \quad (87)$$

and the derivative with respect to t is given by:

$$\frac{\partial}{\partial t} = \frac{1}{\varepsilon_t} \frac{\partial}{\partial t_a} + \frac{\partial}{\partial t_I}, \quad (88)$$

where $t_I = u_f t^*/\delta = t$ and $t_a = c_\infty t^*/(\delta\sqrt{\gamma}) = t/\varepsilon_t$.

Thermal, acoustic and incompressible parts of the fluctuations are defined to have the properties described in section 4.1. The only modification is that (22) is modified to account for the presence of the mean. Thus for any quantity β , its nonacoustic parts $\beta_{t,I}$ satisfy:

$$\frac{\partial \beta'_{t,I}}{\partial t_a} + \varepsilon_t^2 \left(u'_{aj} \frac{\partial (\bar{\beta} + \beta'_{t,I})}{\partial x_j} \right)' \sim o \left(\varepsilon_t^2 \left(u'_{aj} \frac{\partial (\bar{\beta} + \beta'_{t,I})}{\partial x_j} \right)' \right). \quad (89)$$

Therefore, fast time scale variation of the nonacoustic parts $\beta'_{t,I}$ is primarily due to convection of $\bar{\beta}$ and $\beta'_{t,I}$ by fluctuating acoustic velocity.

A.2. Derivation of acoustic and nonacoustic governing equations. Now, by analogy with section 4.2, we substitute (82)–(88) into (7)–(10), collect the terms of equal order in ε_t and using the properties defined in section A.1 derive the governing equations for acoustic and nonacoustic parts of fluctuations. So, the acoustic equations for density, velocity and pressure fluctuations, and the acoustic equation of state are then:

$$\begin{aligned} & \varepsilon_t \left(\frac{\partial \rho'_a}{\partial t_a} + \varepsilon \bar{u}_j \frac{\partial \rho'_a}{\partial x_j} + \varepsilon \rho'_a \frac{\partial \bar{u}_j}{\partial x_j} + \bar{\rho} \frac{\partial u'_{aj}}{\partial x_j} \right) + \\ & \varepsilon_t^2 \left(\frac{\partial \rho'_a}{\partial t_I} + \left(u'_{Ij} \frac{\partial \rho'_a}{\partial x_j} \right)' + \left(\rho'_t \frac{\partial u'_{aj}}{\partial x_j} \right)' \right) + O(\varepsilon_t^3) = 0, \\ & \frac{\partial u'_{ai}}{\partial t_a} + \varepsilon \bar{u}_j \frac{\partial u'_{ai}}{\partial x_j} + \bar{V} \frac{\partial \rho'_a}{\partial x_i} + V'_a \frac{\partial \bar{p}}{\partial x_i} + \end{aligned} \quad (90)$$

$$\varepsilon_t \left(\frac{\partial u'_{ai}}{\partial t_I} + \left(u'_{Ij} \frac{\partial u'_{ai}}{\partial x_j} \right)' + \left(V'_t \frac{\partial p'_a}{\partial x_j} \right)' - \right. \quad (91)$$

$$\left. \frac{2}{Re_t} \left(\varepsilon \bar{V} \frac{\partial \mu'_a \bar{s}_{ij}}{\partial x_j} + \varepsilon V'_a \frac{\partial \bar{\mu} \bar{s}_{ij}}{\partial x_j} + \bar{V} \frac{\partial \bar{\mu} \bar{s}'_{aij}}{\partial x_j} \right) \right) + O(\varepsilon_t^2) = 0,$$

$$\varepsilon_t \left(\frac{\partial p'_a}{\partial t_a} + \varepsilon \bar{u}_j \frac{\partial p'_a}{\partial x_j} + \varepsilon \gamma p'_a \frac{\partial \bar{u}_j}{\partial x_j} + \gamma \bar{p} \frac{\partial u'_{aj}}{\partial x_j} \right) +$$

$$\varepsilon_t^2 \left(\frac{\partial p'_a}{\partial t_I} + \left(u'_{Ij} \frac{\partial p'_a}{\partial x_j} \right)' - \frac{\gamma - 1}{Pr} \frac{\partial}{\partial x_k} \left(\bar{\mu} \frac{\partial T'_a}{\partial x_k} + \mu'_a \frac{\partial \bar{T}}{\partial x_k} \right) - \right. \quad (92)$$

$$\left. \frac{2(\gamma - 1)}{Re_t} \left(\varepsilon^2 \mu'_a \bar{s}_{ij} \bar{s}_{ij} + 2\varepsilon \bar{\mu} \bar{s}_{ij} \bar{s}'_{aij} \right) \right) + O(\varepsilon_t^3) = 0,$$

$$\varepsilon_t^2 \left(-p'_a + \frac{\gamma - 1}{\gamma} (\bar{p} T'_a + \bar{T} p'_a) \right) + O(\varepsilon_t^3) = 0; \quad (93)$$

and the nonacoustic equations are:

$$\varepsilon \bar{u}_j \frac{\partial \rho'_t}{\partial x_j} + \varepsilon \rho'_t \frac{\partial \bar{u}_j}{\partial x_j} + u'_{Ij} \frac{\partial \bar{\rho}}{\partial x_j} +$$

$$\varepsilon_t \left(\frac{\partial \rho'_t}{\partial t_I} + \left(u'_{Ij} \frac{\partial \rho'_t}{\partial x_j} \right)' + u'_{Ij} \frac{\partial \bar{\rho}}{\partial x_j} + \bar{\rho} \frac{\partial u'_{Ij}}{\partial x_j} \right) + \quad (94)$$

$$\varepsilon_t^2 \left(\left(u'_{Ij} \frac{\partial \rho'_t}{\partial x_j} \right)' + \left(\rho'_t \frac{\partial u'_{Ij}}{\partial x_j} \right)' \right) + O(\varepsilon^3) = 0.$$

$$\frac{1}{\varepsilon_t} \left(\varepsilon \bar{u}_j \frac{\partial u'_{Ii}}{\partial x_j} + \varepsilon u'_{Ij} \frac{\partial \bar{u}_i}{\partial x_j} + V'_t \frac{\partial \bar{p}}{\partial x_i} \right) + \frac{\partial u'_{Ii}}{\partial t_I} + \left(u'_{Ij} \frac{\partial u'_{Ii}}{\partial x_j} \right)' +$$

$$\varepsilon \bar{u}_j \frac{\partial u'_{ti}}{\partial x_j} + \varepsilon u'_{tj} \frac{\partial \bar{u}_i}{\partial x_j} + \bar{V} \frac{\partial p'_I}{\partial x_i} - \frac{2}{Re_t} \left(\varepsilon \bar{V} \frac{\partial \mu'_t \bar{s}_{ij}}{\partial x_j} + \varepsilon V'_t \frac{\partial \bar{\mu} \bar{s}_{ij}}{\partial x_j} + \bar{V} \frac{\partial \bar{\mu} \bar{s}'_{Iij}}{\partial x_j} \right) + \quad (95)$$

$$\varepsilon_t \left(\frac{\partial u'_{ti}}{\partial t_I} + \left(u'_{tj} \frac{\partial u'_{Ii}}{\partial x_j} \right)' + \left(u'_{Ij} \frac{\partial u'_{ti}}{\partial x_j} \right)' + \left(V'_t \frac{\partial p'_I}{\partial x_i} \right)' - \frac{2}{Re_t} \left(\left(\varepsilon V'_t \frac{\partial \mu'_t \bar{s}_{ij}}{\partial x_j} \right)' + \right.$$

$$\left. \bar{V} \frac{\partial \bar{\mu} \bar{s}'_{Iij}}{\partial x_j} + \left(V'_t \frac{\partial \bar{\mu} \bar{s}'_{Iij}}{\partial x_j} \right)' + \left(\bar{V} \frac{\partial \mu'_t \bar{s}'_{Iij}}{\partial x_j} \right)' \right) \right) + O(\varepsilon_t^2) = 0,$$

$$u'_{Ij} \frac{\partial \bar{p}}{\partial x_j} + \varepsilon_t \left(u'_{Ij} \frac{\partial \bar{p}}{\partial x_j} + \varepsilon \gamma p'_I \frac{\partial \bar{u}_j}{\partial x_j} + \gamma \bar{p} \frac{\partial u'_{Ij}}{\partial x_j} - \right.$$

$$\left. \frac{\gamma - 1}{Pr} \frac{\partial}{\partial x_k} \left(\bar{\mu} \frac{\partial T'_t}{\partial x_k} + \mu'_t \frac{\partial \bar{T}}{\partial x_k} \right) - \frac{2(\gamma - 1)}{Re_t} \left(\varepsilon^2 \mu'_t \bar{s}_{ij} \bar{s}_{ij} + 2\varepsilon \bar{\mu} \bar{s}_{ij} \bar{s}'_{Iij} \right) \right) + \quad (96)$$

$$\varepsilon_t^2 \left(\left[\frac{\partial p'_I}{\partial t_I} + \frac{\varepsilon}{\varepsilon_t} \bar{u}_j \frac{\partial p'_I}{\partial x_j} + \left(u'_{Ij} \frac{\partial p'_I}{\partial x_j} \right) \right] - \frac{\gamma - 1}{Pr} \frac{\partial}{\partial x_k} \left(\mu'_t \frac{\partial T'_t}{\partial x_k} \right)' - \right.$$

$$\begin{aligned} & \frac{2(\gamma-1)}{Re_t} \left(2\varepsilon \bar{\mu} \bar{s}_{ij} s'_{tij} + \left(2\varepsilon \mu'_t \bar{s}_{ij} s'_{tij} \right)' + \left(\bar{\mu} s'_{ij} s'_{tij} \right)' \right) + O(\varepsilon_t^3) = 0, \\ & \varepsilon_t \frac{\gamma-1}{\gamma} (\bar{T} \rho'_t + \bar{\rho} T'_t) + \varepsilon_t^2 \frac{\gamma-1}{\gamma} \left(-p'_I + (\rho'_t T'_t)' \right) + O(\varepsilon_t^3) = 0. \end{aligned} \quad (97)$$

The leading order terms of (90), (91) and (92) constitute the equations for acoustic fluctuations, linearized about the mean flow. Further, by combining equations (90) and (92) one obtains:

$$\begin{aligned} & \varepsilon_t \left(\varepsilon \bar{u}_j \frac{\partial}{\partial x_j} + \frac{\partial}{\partial t_a} + \varepsilon \frac{\partial \bar{u}_j}{\partial x_j} \right) \left(\frac{\rho'_a}{\bar{\rho}} - \frac{p'_a}{\gamma \bar{p}} \right) = \\ & \varepsilon_t \varepsilon \bar{u}_j \left(-\frac{p'_a}{\gamma \bar{p}^2} \frac{\partial \bar{p}}{\partial x_j} + \frac{\rho'_a}{\bar{\rho}^2} \frac{\partial \bar{\rho}}{\partial x_j} \right) + O(\varepsilon_t^2). \end{aligned} \quad (98)$$

For boundary layer flow, the right hand side of (98) can be neglected except very close to the wall, where mean density gradients may be significant. So, from (98) it follows:

$$\varepsilon_t^2 \rho'_a = \varepsilon_t^2 \frac{\bar{p} p'_a}{\gamma \bar{p}} + O(\varepsilon_t^3) = \varepsilon_t^2 \frac{p'_a}{(\gamma-1) \bar{T}} + O(\varepsilon_t^3), \quad (99)$$

which is just the isentropic relation between pressure and density fluctuations, linearized about the mean. Substituting for ρ'_a in (93) from (99) one obtains:

$$\varepsilon_t^2 T'_a = \varepsilon_t^2 \frac{p'_a}{\bar{p}} + O(\varepsilon_t^3), \quad (100)$$

which is the isentropic relation between pressure and temperature fluctuations, linearized about the mean.

A.3. Consolidated equations. Finally, the decomposed equations derived above can be rewritten in a form that will be more useful in the numerical decomposition discussed in section 5. They are rescaled with u_∞ , and as in section 4.3, the nonacoustic parts of fluctuations are introduced (combined incompressible and thermal fluctuations). For convenience, mean quantities are included in the nonacoustic variables, i.e. nonacoustic variables consist of the mean and nonacoustic parts of the fluctuations. Also, as in section 4.3, the pseudosound contribution to nonacoustic temperature, density and divergence fluctuations is neglected. The nonacoustic equations are then (56)–(59), presented in section 4.4 for convenience. Note that the convective time derivative of incompressible pressure p'_I (terms in

square brackets in (96)), was assumed negligible in (58). This derivative is assumed to be responsible for generation of $O(\varepsilon_t^2)$ pseudosound divergence, analogous to the way pseudosound divergence is defined by Ristorcelli [21], and should not affect the dynamics of the flow dominated by thermal effects. Also, again, as in section 4.3, the time derivatives in (56)–(57) are slow derivatives.

The governing equations for acoustic fluctuations in the new notation are then (60)–(63), presented along with nonacoustic equations in section 4.4. These equations are the equations for acoustic waves in the convective variable density medium defined by the nonacoustic field. The acoustic and nonacoustic equations derived in this section will serve as a basis for development of the numerical decomposition procedure for boundary layer fluctuations discussed in the section 5.

APPENDIX B. DATA ADJUSTMENT PROCEDURE.

As discussed in section 5.5, in order for our decomposition to produce meaningful results, the DNS data must satisfy the governing equations at the wall as well as the boundary conditions. This is not the case in simulations of Maeder *et al.* [14] and many other DNS, because the governing equations at the wall are usually discarded in favor of imposition of the boundary conditions. The boundary conditions used in the simulation of Maeder *et al.* [14] are no-slip and isothermal, so the governing equations evaluated at the wall yield the following relations for temperature and pressure:

$$\left. \frac{\partial}{\partial z} \left(\mu \frac{\partial T}{\partial z} \right) \right|_{z=0} = Pr \, Re \, p \frac{\partial u_k}{\partial x_k} - 2\gamma Ma^2 Pr \mu \overset{\circ}{s}_{ij} \overset{\circ}{s}_{ij} \Big|_{z=0}, \quad (101)$$

$$\left. \frac{\partial p}{\partial z} \right|_{z=0} = \frac{2\gamma Ma^2}{Re} \left. \frac{\partial \mu \overset{\circ}{s}_{3j}}{\partial x_j} \right|_{z=0}. \quad (102)$$

The relations (101) and (102) are obtained from the thermal transport and the wall-normal velocity governing equations respectively. In this appendix, the procedure used to adjust the DNS data to satisfy (101)–(102) is briefly discussed.

In making the adjustment, the temperature at the wall must remain unchanged, since it is restricted by a boundary condition. This also means that the viscosity at the wall will remain unchanged. To impose (101) then, the temperature at the

first point from the wall is adjusted. Even though there is no boundary condition for the pressure at the wall, the value of pressure at the wall was also chosen to remain unchanged, so the pressure is also adjusted at the first point from the wall, analogous to temperature, to satisfy (102). Given the difference scheme used to approximate the derivative at the wall, (101) and (102) become equations for the temperature and pressure at the first point from the wall. These equations are coupled due to the presence of μ in the derivative on the right hand side of (102). Also, the equation (101) is nonlinear due to the presence of μ in the derivative on the left hand side. So, (101) is solved iteratively for the temperature at the first point from the wall, and then pressure at the first point from the wall is determined from (102). With new values of pressure and temperature, the density at this point is determined from the equation of state.

When this adjustment is applied to the data of Maeder *et al.* [14], the changes made to the temperature and pressure are relatively small. In the $Ma = 4.5$ case, which is impacted the most by the data adjustment procedure, since it has the biggest computational domain, the r.m.s. temperature change is 5% of the r.m.s. temperature at the first point from the wall, and the r.m.s. pressure change is less than 1% of the r.m.s. pressure at the first point from the wall.

It should also be mentioned here that the pressure, temperature and density time derivatives were also adjusted in a similar manner using time derivatives of conditions (101)–(102), while advancing the DNS field in time, to keep the governing equations satisfied at the wall at the next time step. This was done because, as discussed in subsection 5.4, the decomposition verification relies on two decomposed subsequent in time data fields to obtain the time derivatives of decomposed quantities.

December 4, 2000

REFERENCES

- [1] B. J. Bayly, C. D. Levermore, and T. Passot. Density variations in weakly compressible flows. *Physics of Fluids A*, 4(5):945–954, May 1992.

- [2] G. A. Blaisdell and S. Sarkar. Investigation of the pressure strain correlation in compressible homogeneous turbulent shear flow. In *Transitional and turbulent compressible flows*, pages 133–138. ASME, 1993.
- [3] B. T. Chu and L. S. G. Kovásznyai. Non-linear interactions in a viscous heat-conducting compressible gas. *Journal of Fluid Mechanics*, 3:494–514, 1958.
- [4] Van Driest. Turbulent boundary layer in compressible fluids. *Journal of aeronautical sciences*, 18(3):145–160, 216, March 1951.
- [5] G. Erlebacher, M. Y. Hussaini, H. O. Kreiss, and S. Sarkar. The analysis and simulation of compressible turbulence. *Theoretical and computational fluid dynamics*, 2:73–95, 1990.
- [6] A. T. Fedorchenko. A model of unsteady subsonic flow with acoustics excluded. *Journal of fluid mechanics*, 334:135–155, 1997.
- [7] M. E. Goldstein. Characteristics of the unsteady motion on transversely sheared mean flows. *Journal of fluid mechanics*, 84:305–329, 1978.
- [8] M. E. Goldstein. Unsteady vortical and entropic distortions of potential flows round arbitrary obstacles. *Journal of fluid mechanics*, 89:433–468, 1978.
- [9] S. Guarini. *Direct numerical simulation of supersonic turbulent boundary layers*. PhD thesis, Stanford University, 1998.
- [10] S. Klainerman and A. Majda. Singular limits of quasilinear hyperbolic systems with large parameters and the incompressible limit of compressible fluids. *Communications on pure and applied mathematics*, 34:481–524, 1981.
- [11] S. Klainerman and A. Majda. Compressible and incompressible fluids. *Communications on pure and applied mathematics*, 35:629–651, 1982.
- [12] H.-O. Kreiss, J. Lorenz, and M. J. Naughton. Convergence of the solutions of the compressible to the solutions of the incompressible Navier-Stokes equations. *Advances in applied mathematics*, 12:187–214, 1991.
- [13] S. K. Lele. Compressibility effects on turbulence. *Annual Review of Fluid Mechanics*, 26:211–254, 1994.
- [14] T. Maeder, N. A. Adams, and L. Kleiser. Direct simulation of turbulent supersonic boundary layers by an extended temporal approach. *Submitted for publication at Journal of Fluid Mechanics*.
- [15] A. Majda and J. Sethian. The derivation and numerical solution of the equations for zero mach number combustion. *Combustion science and technology*, 42:185–205, 1985.
- [16] W. H. Matthaeus and M. R. Brown. Nearly incompressible magnetohydrodynamics at low mach number. *Physics of Fluids*, 31(12):3634–3644, December 1988.
- [17] W. H. Matthaeus, L. W. Klein, S. Ghosh, and S. M. Brown. Nearly incompressible magnetohydrodynamics, pseudosound and solar wind fluctuations. *Journal of Geophysical Research*, 96:5421–5435, 1991.

- [18] M. V. Morkovin. Effects of compressibility on turbulent flows. In A. Favre, editor, *Mechanique de la Turbulence*, pages 367–380. CNRS, 1962.
- [19] B. Müller. Low-mach-number asymptotics of the Navier-Stokes equations. *Journal of engineering mathematics*, 34:97–109, 1998.
- [20] A. Novotny and K. Pileckas. Steady compressible Navier-Stokes equations with large potential forces via a method of decomposition. *Mathematical methods in applied sciences*, 21:665–684, 1998.
- [21] Ristorcelli J. R. A pseudo-sound constitutive relationship for the dilatational covariances in compressible turbulence. *Journal of Fluid Mechanics*, 347:37–70, 1997.
- [22] Rubinstein R. and Erlebacher G. Transport coefficients in weakly compressible turbulence. *Physics of Fluids A*, 9(10):3037–3057, October 1997.
- [23] S. Sarkar, G. Erlebacher, M. Y. Hussaini, and H. O. Kreiss. The analysis and modeling of dilatational terms in compressible turbulence. *Journal of fluid mechanics*, 227:473–493, 1991.
- [24] A. J. Smits and J.-P. Dussauge. *Turbulent shear layers in supersonic flow*. AIP Press, 1996.
- [25] P. R. Spalart. Direct simulation of a turbulent boundary layer up to $Re_\theta = 1440$. *Journal of Fluid Mechanics*, 187:61–98, 1988.
- [26] E. F. Spina, A. J. Smits, and S. K. Robinson. The physics of supersonic turbulent boundary layers. *Annual Review of Fluid Mechanics*, 26:287–319, 1994.
- [27] F. M. White. *Viscous fluid flow*. McGraw-Hill, 1991.
- [28] G. P. Zank and W. H. Matthaeus. The equations of nearly incompressible fluids. I. Hydrodynamics, turbulence and waves. *Physics of Fluids A*, 3(1):69–82, January 1991.

DEPARTMENT OF THEORETICAL AND APPLIED MECHANICS, UNIVERSITY OF ILLINOIS, URBANA,
IL 61801, USA

APPENDIX C

Preprint of "A critical evaluation of the resolution properties of B-spline and compact finite difference methods" by W. Y. Kwok, R. D. Moser and J. Jimenez (1999). Under consideration for publication in *J. Comput. Physics*.

A Critical Evaluation of the Resolution Properties of B-spline and Compact Finite Difference Methods

Wai Yip Kwok and Robert D. Moser

Department of Theoretical and Applied Mechanics, University of Illinois at Urbana-Champaign, Urbana, IL 61801, USA

and

Javier Jiménez

School of Aeronautics, 28040 Madrid, Spain

Resolution properties of B-spline and compact finite difference schemes are compared using Fourier analysis in periodic domains, and tests based on solution of the wave and heat equations in finite domains, with uniform and non-uniform grids. Results show that compact finite difference schemes have a higher convergence rate and in some cases better resolution. However, B-spline schemes have a more straightforward and robust formulation, particularly near boundaries on non-uniform meshes.

Key Words: resolution; B-spline methods; compact finite difference methods; 65M06; 65M60; 76F65

1. INTRODUCTION

Many physical phenomena involve a broad range of spatial scales. One example is turbulent fluid flows, which have a wide and continuous spectrum of length scales describing its composition of eddies of different sizes [2]. Simulation of these physical phenomena requires spatial discretization schemes with high resolution, or in other words, schemes that can produce accurate numerical results over as broad a range of length scales as possible for a given discretization.

In numerical simulation of turbulent fluid flows, spectral methods are attractive spatial discretization schemes due to their very good resolution properties. As a result, many direct numerical simulations (DNS) have been performed with spectral methods in Cartesian coordinates with various boundary conditions ([4] and [14]). These include simulations of simple fundamental flows such as isotropic turbulence, turbulent channel flows [20] and turbulent boundary layer [33]. One distinctive feature of spectral methods is that they use infinitely differentiable global basis functions [4]. Two common choices are Fourier series expansions and polynomial basis functions, with the first being applied to simulations with periodic boundary conditions and the second to simulations in finite intervals ([20] and [28]). However, the global character of the basis functions also limits spectral methods to simple geometries and boundary conditions [23] and there

is a great need for simulations in complex geometries. This is very important for turbulence simulations to contribute to many engineering applications such as external aerodynamics and propulsion systems. Such simulations would require spatial discretization schemes that not only retain the good resolution properties of spectral methods, but can also provide flexibility with respect to geometries, boundary conditions and grid distribution.

Local numerical representations, such as finite difference and finite element schemes, have much greater flexibility in discretizing complex geometries, so high resolution schemes of these types would be of great interest. For example, Lele has studied compact finite difference schemes for use in problems with a broad range of spatial scales [23], using Fourier analysis to investigate how well the schemes represent a range of wave numbers. There has also been a trend to combine local discretization algorithms and spectral methods. A typical example of such a confluence of numerical algorithms is the spectral element method which is based on finite element and spectral methods [18],[19],[27].

Another choice for local numerical representation is to use splines. Unlike finite difference methods, spline methods are functional expansion methods that make use of a set of local basis functions. This property provides us with a straight-forward way to implement boundary conditions. Spline methods are similar to finite element methods as they both use piecewise polynomial representations. However, spline methods use basis functions that retain a higher degree of continuity. In short, spline methods have much of the flexibility afforded by the use of local expansions, as in finite elements, and have the resolution advantage afforded by highly continuous expansions, as in spectral methods.

In the research reported here, we investigate the properties of spline methods, in particular spline collocation methods, and their relation to finite difference and finite element methods. Section 2 introduces the basic properties of spline, compact finite difference, finite element methods and their different formulation. The basic resolution properties of these spatial discretization schemes are presented in Section 3 using Fourier analysis in periodic domains. Of particular interest is the approximation to the first and second derivative operator, which are common in equations describing many physical phenomena. In Section 4 and Section 5, the wave equation and heat equation are solved with spline collocation and compact finite difference schemes in bounded domains, in both uniform and non-uniform grids. Concluding remarks are given in Sections 6.

2. NUMERICAL REPRESENTATIONS

The resolution properties of the numerical methods discussed here are most easily understood in one spatial dimension. Thus, the methods to be evaluated are introduced here in their one-dimensional form. Spline methods, compact finite difference methods and finite element methods will be discussed.

2.1. Spline Methods

Consider a domain divided into N intervals, a one-dimensional spline is defined to be a polynomial of degree d in each interval that is continuously differentiable $d - 1$ times at the interval boundaries. The boundaries of the intervals are called knots.

Spline methods have been used before to solve differential equations and fluid mechanics problems ([13], [29] and [30]). The work of Kasi Viswanadham and Koneru [37] and Davies [6],[7] used B-splines as basis functions and the Galerkin formulation. Most of the research, however, is confined to cubic splines ($d = 3$). More recently, Kravchenko *et al.* [21] and Shariff and Moser [32] used the basis functions of splines to solve partial differential equations and simulate turbulent

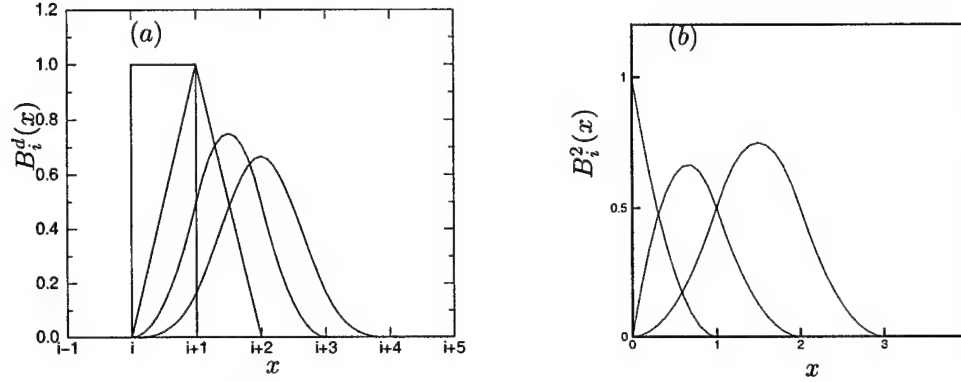


FIG. 1. B-splines $B_i^d(x)$ on uniform knots with knot spacing $\Delta x = 1$, with (a) $d = 0, 1, 2$ and 3 ; and with (b) $d = 2$ and $i = 1, 2$ and 3 .

fluid flows. In particular, mesh embedding techniques are developed to make basis spline methods very effective in solving physical problems in complex geometries.

To use splines as a representation for the solution of a partial differential equation, it is necessary to have a convenient basis for the space of spline functions under consideration. Here the so called basis splines or "B-splines" as described in [8] and [16] are used. A B-spline is defined as a normalized spline which has support over the minimum possible number of intervals. In fact, it has support on only $d + 1$ intervals. As an example, the B-splines B_i^d for uniformly spaced knots are plotted in figure 1 (a) for d up to 3. By using a basis with support on the minimum possible number of intervals, minimum bandwidth of the resulting matrices is ensured.

Near a boundary, the basis splines are different than those in figure 1(a) since the presence of the boundary removes the constraint that the B-splines have $d - 1$ zero derivatives at the edge of its interval of supports. An example of the quadratic B-splines near the boundary is shown in figure 1(b).

To use the B-splines in a practical computation, one needs to evaluate them and their derivatives at points in the domain. This will be sufficient to compute the various matrices representing different linear operators. An efficient and stable technique to evaluate the B-splines and their derivatives is the recurrence relation described in [8]. Both interior and boundary splines are generated this way by formally introducing a multiplicity of knots at the boundary (see [8]).

Consider the B-spline representation of a possibly non-linear spatial operator \mathcal{F} operating on ϕ . We first postulate an expansion for ϕ in terms of B-splines of order d on a selected knot set:

$$\phi(x) \approx \tilde{\phi}(x) = \sum_i \alpha_i B_i^d(x) \quad (1)$$

An approximation $\tilde{\mathcal{F}}$ to the operator \mathcal{F} is sought that maps splines in S_d (i.e. $\tilde{\phi}$) to splines in S_d , where S_d is the space of splines of order d for the selected knot set. That is

$$\mathcal{F}(\tilde{\phi}) \approx \tilde{\mathcal{F}}(\tilde{\phi}) = \tilde{\gamma} = \sum_i \beta_i B_i^d(x) \quad (2)$$

There are several ways to generate such an approximation. Two will be considered here, namely Galerkin and collocation methods.

2.1.1. B-spline Galerkin Methods

In the Galerkin formulation, the approximation of the linear differential operator \mathcal{D} on $\tilde{\phi}$ is given by

$$(B_j^d, \tilde{\gamma}) = (B_j^d, \mathcal{D}\tilde{\phi}), \quad j = 1, 2, \dots, N_\zeta \quad (3)$$

where (f, g) denotes the L_2 inner product $\int f g dx$ in the domain and N_ζ is the number of B-splines. This forces the error in $\tilde{\gamma}$ to be orthogonal to S_d , thus minimizing the L_2 error in this space. Given the linearity of \mathcal{D} and the representations of $\tilde{\mathcal{D}}$, $\tilde{\phi}$ and $\tilde{\gamma}$, the above equation can be written

$$\sum_{i=1}^{N_\zeta} \beta_i (B_j^d, B_i^d) = \sum_{i=1}^{N_\zeta} \alpha_i (B_j^d, \mathcal{D}(B_i^d)) \quad , \quad j = 1, 2, \dots, N_\zeta \quad (4)$$

The inner products of equation (4) are the elements of matrices M and D , with $M_{ij} = (B_j^d, B_i^d)$ and $D_{ij} = (B_j^d, \mathcal{D}(B_i^d))$. The matrix M is called the “mass” matrix and D the operator matrix. To obtain $\tilde{\gamma}$ given $\tilde{\phi}$ one solves the linear system $M\beta = D\alpha$. Note that both M and D are banded matrices since individual B-splines have only local support. The bandwidth w of the matrices is given by $w = 2d + 1$.

2.1.2. B-spline Collocation methods

The collocation formulation imposes different requirements to obtain the coefficients β_i . Here the approximation $\tilde{\gamma} = \sum_i \beta_i B_i^d$ of the operator \mathcal{D} on $\tilde{\phi}$ must satisfy

$$\tilde{\gamma} = \mathcal{D}\tilde{\phi} \quad \text{at } x = \zeta_j, \quad j = 1, 2, \dots, N_\zeta \quad (5)$$

which implies

$$\sum_{i=1}^{N_\zeta} \beta_i B_i^d = \sum_{i=1}^{N_\zeta} \alpha_i \mathcal{D}(B_i^d) \quad \text{at } x = \zeta_j, \quad j = 1, 2, \dots, N_\zeta \quad (6)$$

The values of the b-splines and their derivatives are the elements of the matrices M and D respectively, with $M_{ij} = B_i^d(\zeta_j)$ and $D_{ij} = [\mathcal{D}(B_i^d)](\zeta_j)$. Again, given $\tilde{\phi}$, $\tilde{\gamma}$ is found by solving the linear system $M\beta = D\alpha$. Using the collocation formulation, the matrix bandwidth w is given by $w = d$.

2.1.3. Selection of Knots and Collocation Points

To use B-splines in a computation, one first needs to determine the location of the knot points and for the collocation method the collocation points. In a periodic domain with N uniform width intervals, there are N knots and N splines spanning the spline space. Therefore, N collocation points are needed in a collocation scheme. There are only two locations for the collocation points that preserve the spatial symmetry of the operators : collocation points at the knots, and collocation points at the center of the intervals. The former is appropriate for odd-order splines, the later for even (see below).

In a non-periodic domain, it is more complicated. There are N intervals, $N + 1$ distinct knots and $N + d$ collocation points are needed. There are two basic ways to select knots and collocation points in a finite domain. The first is that $N + d$ collocation points can be selected by whatever resolution criteria are appropriate and then $N + 1$ of these points can be chosen to be the knots.

Generally those collocation points that are not knots are near the boundary, though the knot at the boundary is retained. This is referred to as a "not-a-knot" condition, which is commonly used in spline interpolation.

The alternative is to start by selecting the knots according to some resolution criteria. This is more natural since the knots directly determine the spline space and therefore are more closely related to resolution than the collocation points. Furthermore, in a Galerkin scheme all one selects are the knots, so direct comparison of Galerkin and collocation is only possible if one starts by selecting the knots. Selecting the collocation points can then be done in several ways, but there are two choices that seem particularly appropriate : place a collocation point at the maximum of each B-spline function or place it at the centroid of each B-spline function. These prescriptions have the advantage that they are applicable throughout the domain (nothing special about the boundary), and they associate a collocation point directly with each B-spline function. This latter property is useful for applications in multidimensional embedded grids of the type described by Shariff and Moser [32]. Note that with uniform knots away from the boundary, the symmetry of the B-splines places the maxima and centroid at the same location : at the knots or at the center of the intervals for odd and even splines respectively. In the current paper, collocation points at the B-spline maxima are selected, because this naturally places a collocation point at the boundary, which is useful for imposing boundary conditions. Two knot distributions are used : uniformly spaced knots and non-uniform knots distribution according to :

$$x = 0.5 \left\{ 1 - \frac{\cos[\pi \frac{(N-1)\xi+1}{N+1}]}{\cos[\pi \frac{1}{N+1}]} \right\} \quad (7)$$

where $\xi = j/N$ for $j = 0, 1, \dots, N$. This non-uniform grid is basically a Chebyshev grid with the boundary singularities removed. It is denser near the boundary.

2.2. Compact Finite Difference Methods

Compact finite difference schemes have long been applied to fluid mechanics and other physics problems [17],[22], [31]. Recently, higher order compact finite difference schemes have seen increasing use in the direct numerical simulation of complex fluid flows ([12] and [26]). Lele presented a comprehensive study on the compact finite difference methods [23]. Consider a uniform mesh where the nodes are indexed by i . The independent variable at the nodes is x_i and the function values at the nodes $v_i = v(x_i)$ are given. The compact schemes are derived by writing approximations of the form :

$$\beta v'_{i-2} + \alpha v'_{i-1} + v'_i + \alpha v'_{i+1} + \beta v'_{i+2} = c \frac{v_{i+3} - v_{i-3}}{6\Delta x} + b \frac{v_{i+2} - v_{i-2}}{4\Delta x} + a \frac{v_{i+1} - v_{i-1}}{2\Delta x} \quad (8)$$

Similarly, approximations to the second derivative operator are derived by the following relationship :

$$\beta v''_{i-2} + \alpha v''_{i-1} + v''_i + \alpha v''_{i+1} + \beta v''_{i+2} = c \frac{v_{i+3} - 2v_i + v_{i-3}}{9(\Delta x)^2} + b \frac{v_{i+2} - 2v_i + v_{i-2}}{4(\Delta x)^2} + a \frac{v_{i+1} - 2v_i + v_{i-1}}{(\Delta x)^2} \quad (9)$$

TABLE 1

Table of coefficients for discretized first derivative operators using compact finite difference schemes. The approximations have the form $\sum_j \alpha_j (f'_{i+j} + f'_{i-j}) + f'_i = \sum_j a_j \frac{f_{i+j} - f_{i-j}}{2j\Delta x}$

Band-width	Order	α_1	α_2	α_3	α_4	α_5	a_1	a_2	a_3	a_4	a_5
3	4	$\frac{1}{4}$	0	0	0	0	$\frac{3}{2}$	0	0	0	0
5	8	$\frac{4}{9}$	$\frac{1}{36}$	0	0	0	$\frac{40}{27}$	$\frac{25}{54}$	0	0	0
7	12	$\frac{9}{16}$	$\frac{100}{16}$	$\frac{1}{400}$	0	0	$\frac{21}{16}$	$\frac{231}{250}$	$\frac{147}{2000}$	0	0
9	16	$\frac{16}{25}$	$\frac{4}{25}$	$\frac{1}{1225}$	$\frac{1}{4900}$	0	$\frac{144}{125}$	$\frac{152}{125}$	$\frac{10704}{42875}$	$\frac{761}{85750}$	0
11	20	$\frac{25}{36}$	$\frac{100}{441}$	$\frac{25}{784}$	$\frac{1}{15876}$	$\frac{1}{63504}$	$\frac{55}{54}$	$\frac{12760}{9261}$	$\frac{5115}{10976}$	$\frac{23045}{500094}$	$\frac{7381}{8001504}$

The relations between the coefficients a, b, c and α, β are obtained by matching the Taylor series coefficients of various orders. Higher orders can be obtained by including more nodes in the above two equations.

In this study, compact schemes with the same stencil size on both sides of the equations are selected ($c = 0$ in equations (8) and (9) for example). This is because mass and operator matrices with the same bandwidth is a property shared by B-spline methods. All the coefficients then are used to match the Taylor series to as high an order as possible. The value of the coefficients are listed in tables 1 and 2 for schemes with matrix bandwidth w up to 11. Note that since no restriction is imposed on the coefficients other than those from Taylor series matching, mass matrices associated with the first, second and higher derivatives are all different. This issue will be addressed in more detail in Section 6.

2.3. Finite Element Methods

Most of the finite element applications in fluid dynamics use the Galerkin finite element formulation [11]. The application of the traditional finite element method to fluid mechanics is treated by Thomasset [35] and Baker [1].

In this study, the standard one-dimensional C_0 finite elements are used. As with B-splines, the finite elements are polynomials on a series of knots (element boundaries). However, because only C_0 continuity is imposed, there are many more degrees of freedom per interval (element). If there are N intervals then there would be dN degrees of freedom, where d is the degree of the polynomials. In this paper, only finite element Galerkin methods are considered, though collocation methods are also possible. Note that this method of increasing the local degree of the polynomial shapefunction is very similar to the “ p ” finite element method [10], in which an element may neighbor an element having different polynomial order. The main advantage of finite element methods is flexibility with respect to geometry. Its weakness is resolution. In most applications of finite element methods, elements are typically chosen to be at most quadratic ([3], [9]), and consequently, great accuracy is usually difficult to achieve. This is exactly opposite to the characteristics of spectral methods. The intention to combine these two methods comprehensively leads to the development of spectral element methods [19],[27]. Spectral element methods are basically variational domain decomposition techniques. The computational domain is broken up into macro- elements within which variables are represented as high-order

TABLE 2

Table of coefficients for discretized second derivative operators using compact finite difference schemes. The approximations have the form $\sum_j \alpha_j (f''_{i+j} +$

$$f''_{i-j}) + f''_i = \sum_j a_j \frac{f_{i+j} - 2f_i + f_{i-j}}{j^2 h^2}$$

Band-width	Order	α_1	α_2	α_3	α_4	α_5
3	4	0.1	0	0	0	0
5	8	2.91773×10^{-1}	9.75403×10^{-3}	0	0	0
7	12	4.54859×10^{-1}	5.07012×10^{-2}	8.53431×10^{-4}	0	0
9	16	5.70136×10^{-1}	1.12742×10^{-1}	6.74436×10^{-3}	6.85946×10^{-5}	0
11	20	6.48365×10^{-1}	1.80383×10^{-1}	2.03536×10^{-2}	7.63768×10^{-4}	5.21170×10^{-6}

Band-width	Order	a_1	a_2	a_3	a_4	a_5
3	4	1.2	0	0	0	0
5	8	8.14249×10^{-1}	7.88804×10^{-1}	0	0	0
7	12	3.63508×10^{-1}	1.44465	2.04670×10^{-1}	0	0
9	16	7.96376×10^{-2}	1.60567	6.58960×10^{-1}	3.51163×10^{-2}	0
11	20	-7.02859×10^{-2}	1.47231	1.12003	1.72919×10^{-1}	4.77013×10^{-3}

polynomial expansions [18]. The work of Patera [27], Karniadakis [18] and their co-workers illustrates the application of spectral element methods in partial differential equations and fluid mechanics problems.

2.4. Basis for Comparison

To compare the resolution properties of the several spatial discretization schemes discussed above, it is necessary to define the basis of comparison. The question is : comparing B-spline, finite element and finite difference methods, what characteristics of these methods (i.e. what degree polynomials, or what stencil size) should be compared. In this paper we take the view that comparison should be done between schemes with matrices that have the same bandwidth. The bandwidth of the matrices is an indicator of the computational cost of the scheme, so methods with the same cost are compared.

3. FOURIER ANALYSIS

In this section, a Fourier analysis of the errors associated with the approximation of differential operators by the several spatial discretization schemes discussed in section 2 is presented. The resolution properties of the numerical schemes are most directly investigated using a Fourier analysis ([23], [24], [25], [34], ([36]), in which the approximations of the operators in a periodic domain with a uniform grid are compared.

3.1. Effective Wave Number and Eigenfunctions

One common measure of how well a differential operator is approximated is the effective wavenumber. In a periodic domain, the eigenfunctions of derivative operators are the complex exponentials, and the eigenvalues of the n^{th} derivative are $(ik)^n$ where k is the wavenumber of the complex exponential and $i = \sqrt{-1}$. The effective wavenumbers \tilde{k} are obtained from the eigenvalues of the approximate derivative operators $M^{-1}D$ as $\tilde{k}_j = \sqrt[n]{\frac{\lambda_j}{i^n}}$, where λ_j is the j^{th} eigenvalue of the approximate operators. For central schemes like those studied in this section, \tilde{k} is real. Perhaps more important than the effective wavenumber is the error in the eigenvalue $|\lambda - (ik)^n|$. Also of interest is how closely the eigenfunctions of the approximate operator correspond with the exact eigenfunctions (the complex exponentials).

While the effective wave number has been widely studied as an indicator of the accuracy and resolution of approximate derivative operators, the accuracy with which the eigenfunctions of the operators (the complex exponentials) are represented has not generally been considered. One reason is that in finite difference methods, the circulant nature of the operator matrices assures that the eigenfunctions of the operators exactly represent the values of e^{ikx} at the finite difference grid points. However, with methods based on functional representations, one can measure the L_2 errors $\|e^{ikx} - \psi_j(x)\|$, where $\psi_j(x)$ are the approximate eigenfunctions. Again since the matrices M and D are circulant, regardless of what derivative is being approximated, the approximate operator has the same eigenfunctions for all derivatives. It can be shown that these approximate eigenfunctions are also the same as those obtained by directly approximating the complex exponential, using the method under considerations (spline or finite element, Galerkin or collocation).

3.2. Comparison of Accuracy and Resolution

The numerical schemes tested using Fourier analysis include B-spline collocation and Galerkin formulations, finite element Galerkin formulations, and compact finite difference methods. Effective wavenumbers associated with the first and second derivatives for the four methods discussed here are shown in figures 2 and 3 respectively. Notice that the wavenumber is normalized by the maximum wavenumber k_{max} representable with the numerical method. For the spline and finite difference methods $k_{\text{max}} = \frac{\pi}{\Delta x}$, where Δx is the grid or knot spacing. For the finite element schemes, $k_{\text{max}} = \frac{d\pi}{\Delta x}$, since there are d degrees of freedom per element.

There are several things to note about the effective wavenumbers. First, for a given matrix bandwidth w , \tilde{k} is identical for B-spline collocation and Galerkin methods. This is despite the fact that for collocation the order of the splines is higher ($d = w$) than for the Galerkin ($d = \frac{w-1}{2}$). This identity had been noted before by Swartz & Wendroff[34]. Second, for a tridiagonal matrix, the finite element scheme (linear elements) is identical to the spline Galerkin method (linear splines). For first derivatives, the effective wavenumber is also the same as that for compact finite difference, which is the 4th order Pade scheme. For the second derivative, however, they are different. Finally, the high-order (large bandwidth) finite element effective wavenumbers depart suddenly from the exact result, effectively limiting the range of wavenumbers for which \tilde{k} is a good approximation of k .

The errors in the eigenvalues $|\lambda - (ik)^n|$ for the first and second derivatives, and those in the eigenfunctions are plotted in figures 4, 5 and 6 respectively. In comparing the different methods, the most obvious difference is the rate of convergence at small k : these curves asymptotically approach zero according to their theoretical convergence rate as shown in table 3.

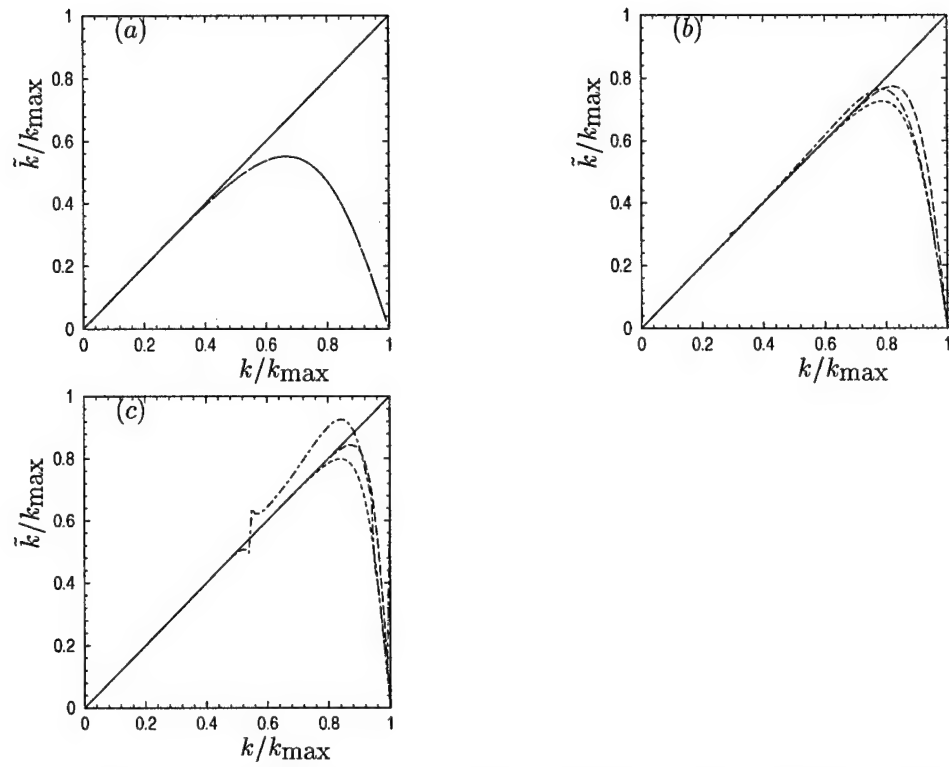


FIG. 2. Effective wavenumber \tilde{k} of the first derivative operators for matrix bandwidth (a)3, (b)7, (c)11: ---, b-spline; ---, compact finite difference; - · - · -, finite element Galerkin; —, exact differentiation. For bandwidth equals 3, the three schemes yield the same result.

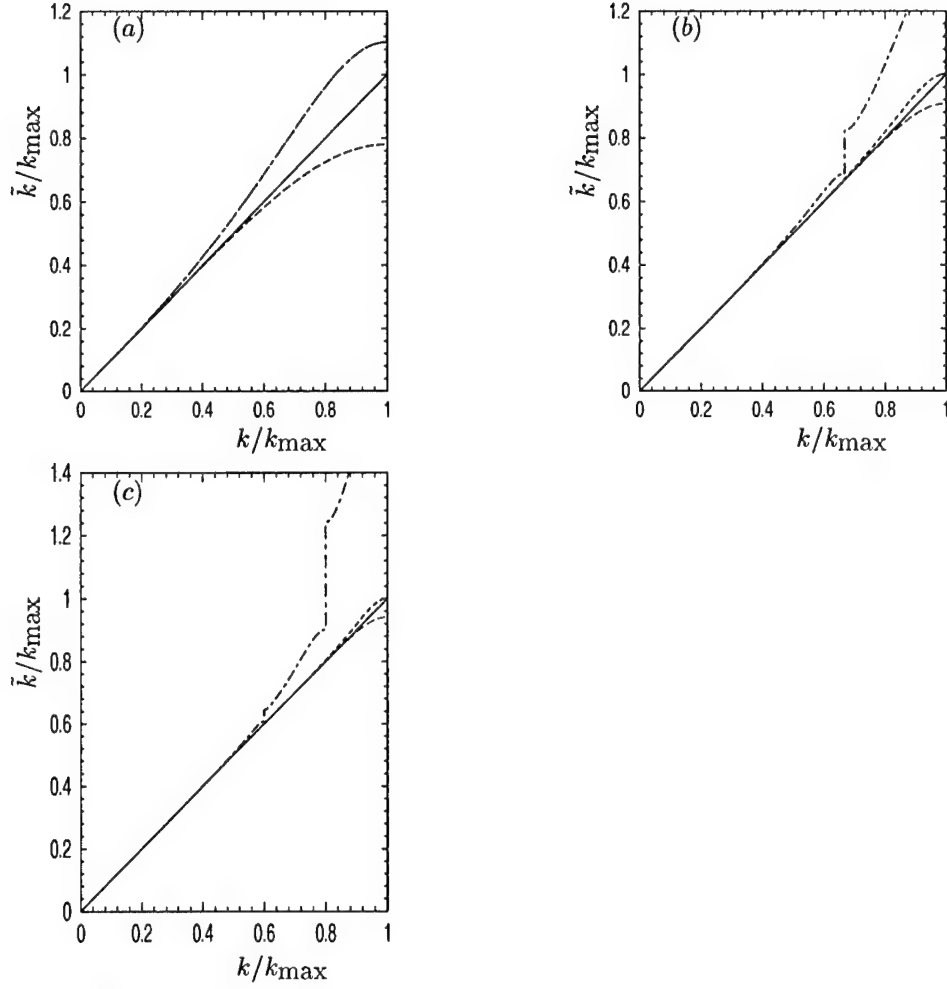


FIG. 3. Effective wavenumber \tilde{k} of the second derivative operators for matrix bandwidth (a)3, (b)7, (c)11: ---, b-spline; - - -, compact finite difference; - · - · -, finite element Galerkin; —, exact differentiation. For bandwidth equals 3, b-spline and finite element yields the same result.

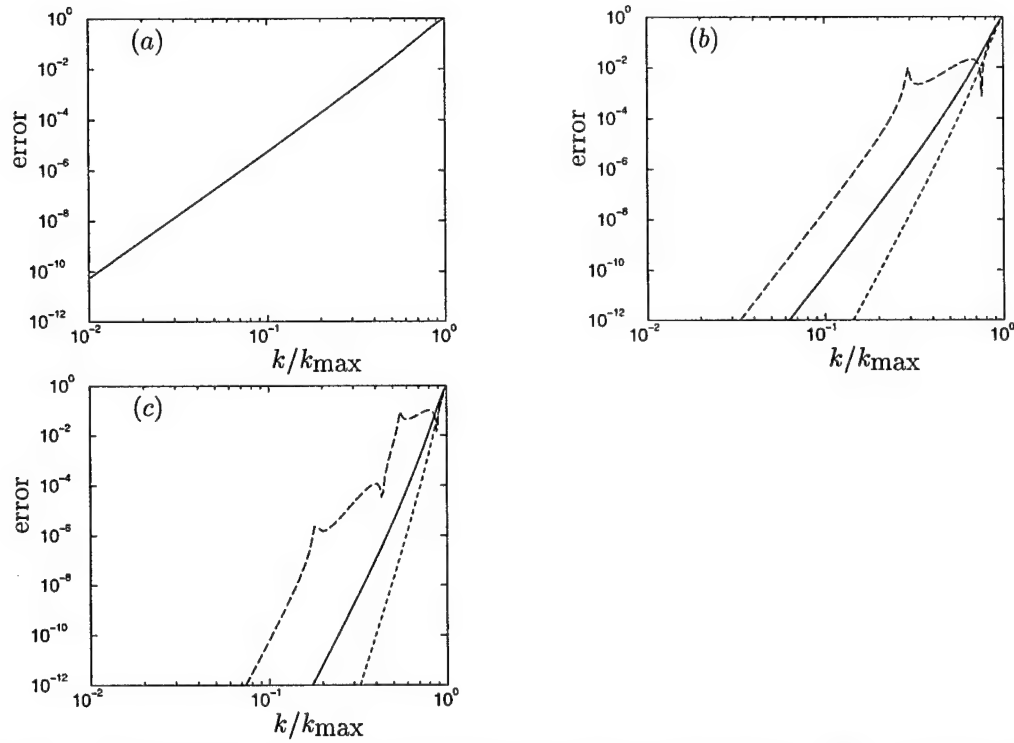


FIG. 4. Error in the eigenvalue of first derivative operators for matrix bandwidth (a)3, (b)7, (c)11: —, b-spline; ---, compact finite difference; - · -, finite element Galerkin. For bandwidth equals 3, all schemes yield the same result.

Note that the compact finite difference convergence rate is significantly faster for large w . This is possible because in the finite difference method, the "mass" matrix can be different for each order derivative. In contrast, by the nature of functional expansion methods, the mass matrix is the same for all derivatives that can be determined from the representation. If this restriction were imposed on the compact finite difference methods, the same order of convergence as the spline and finite element methods would be obtained.

TABLE 3
Order of convergence of the errors of eigenvalues and eigenfunctions. w is the matrix bandwidth.

Numerical Scheme	Eigenvalue of the first derivative operator	Eigenvalue of the second derivative operator	Eigenfunction
finite element Galerkin	k^{w+2}	k^{w+1}	$k^{\frac{w+1}{2}}$
B-spline Galerkin	k^{w+2}	k^{w+1}	$k^{\frac{w+1}{2}}$
B-spline collocation	k^{w+2}	k^{w+1}	k^{w+1}
compact finite difference	k^{2w-1}	k^{2w}	N.A.

The other property of the approximate operators is the behavior of the error at large k . This is important because it determines the range of spatial scales that can be resolved by the numerical

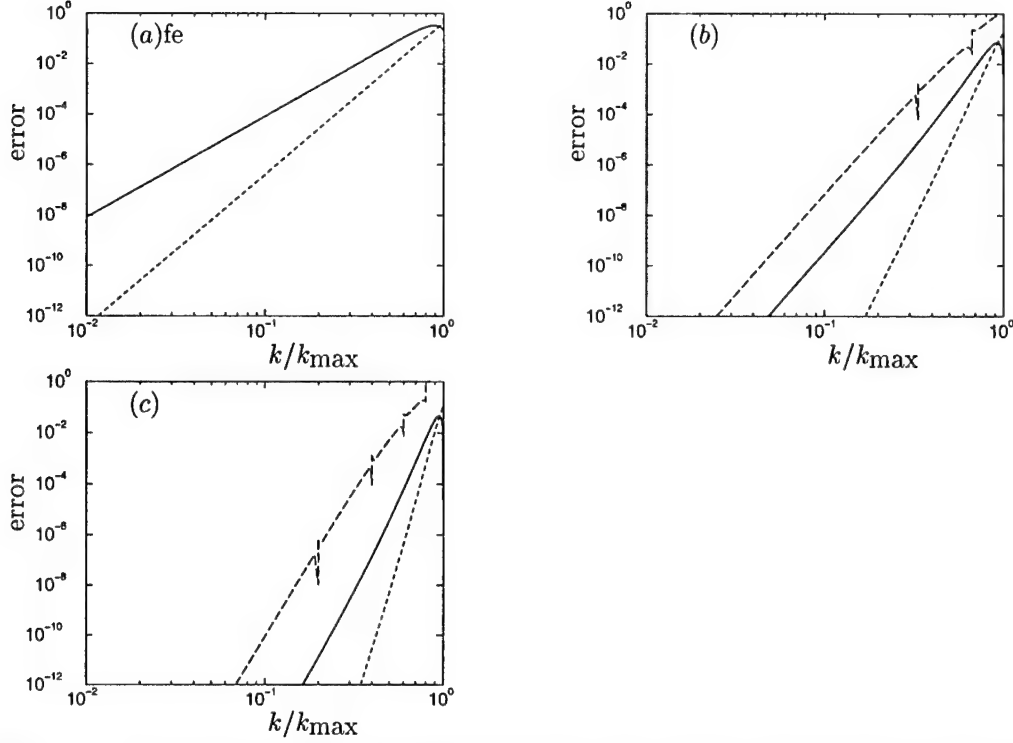


FIG. 5. Error in the eigenvalue of second derivative operators for matrix bandwidth (a)3, (b)7, (c)11: —, b-spline; ---, compact finite difference; - · -, finite element Galerkin. For bandwidth equals 3, b-spline and finite element yields the same result.

method. There is no commonly used measure of this resolution property of numerical methods. One measure proposed by Lele [23] is the lowest wavenumber (k/k_{max}) at which the error crosses some arbitrary threshold (say 0.1), giving the fraction of the maximum wavenumber range that is represented to this accuracy or better. In table 4, this resolved fraction for 10 % error in the eigenvalues and eigenfunctions is listed for the numerical schemes discussed.

Despite the fact that the order of convergence for the finite element and spline effective wave numbers is the same, the errors in the spline methods are much lower at any given k . In essence, the spline methods have better resolution. This is indicated by Lele's resolution measure as shown in table 4. The reason for the relatively poor resolution of the finite element is the low (C_0) continuity at the element boundary. One way to understand this (for the first derivative) is to imagine a high order finite element function u evolving according to the scalar wave equation: $\frac{\partial u}{\partial t} + c \frac{\partial u}{\partial x} = 0$. At the initial time there are discontinuities in first derivative at the element boundaries. The exact solution would have these discontinuities propagate into the middle of the element, where they cannot be well represented, leading to relatively large errors. This scenario suggests that maximum possible continuity at the knots, that is splines, is desirable.

The uniform grid periodic analysis is informative, but it does not address two key issues commonly encountered in numerical simulations, that is nonuniform grids and boundaries. The behavior of finite difference methods in particular is at issue since the formulation discussed in section 2.2 does not apply directly in these cases. Also, the result that the eigenfunctions of the derivative operators are recovered exactly (section 3.1) will not hold. It is thus of interest to consider model problems in finite domains. Two such problems are discussed here, namely the

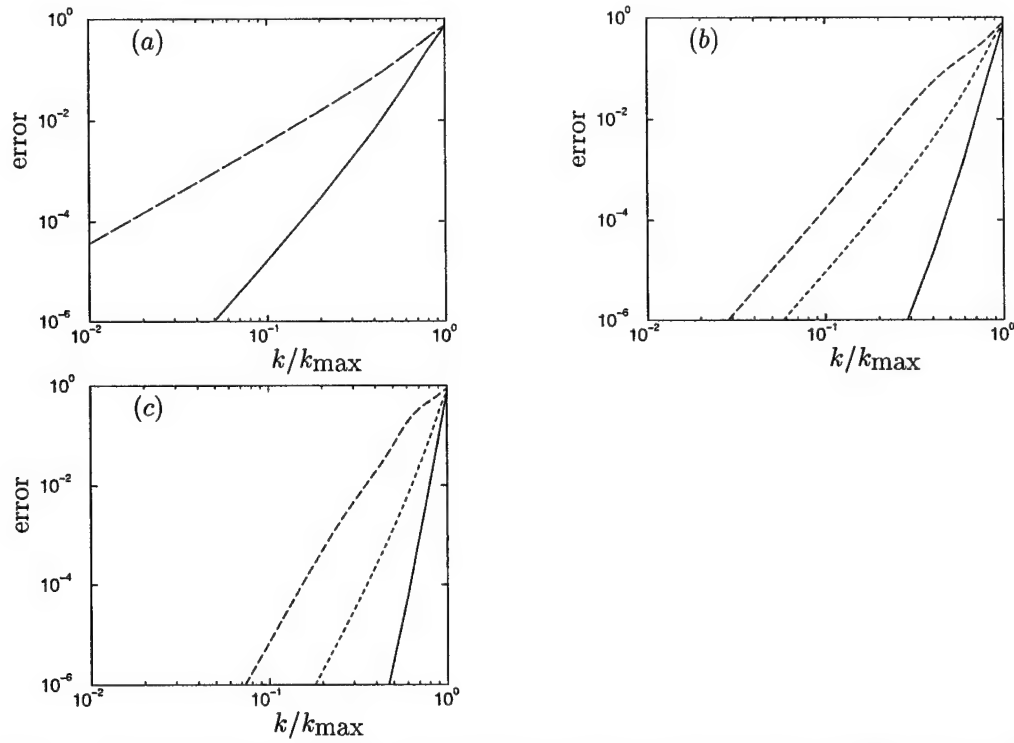


FIG. 6. L_2 error in the representation of the complex exponential with wavenumber k for matrix bandwidth (a)3, (b)7, (c)11: —, b-spline collocation; ---, b-spline Galerkin; - - -, finite element Galerkin. For bandwidth equals 3, b-spline Galerkin and finite element Galerkin yields the same result.

TABLE 4
10 % resolved fraction for eigenvalues of first and second derivative operators,
and eigenfunction representation.

Band- width	d/dx			Band- width	d^2/dx^2		
	B-spline	Compact finite difference	Finite element Galerkin		B-spline	Compact finite difference	Finite element Galerkin
3	0.59	0.59	0.59	3	0.34	0.68	0.34
7	0.80	0.84	0.82	7	1.00	0.94	0.57
11	0.87	0.90	0.54	11	1.00	0.99	0.59

Band- width	Eigenfunction		
	B-spline collocation	B-spline Galerkin	Finite element Galerkin
3	0.68	0.46	0.46
7	0.84	0.72	0.48
11	0.89	0.81	0.53

wave and heat equation. They will only be applied to the B-spline collocation and compact finite difference schemes, the two best methods discussed above.

4. WAVE EQUATION IN BOUNDED DOMAINS

In this section, B-spline collocation methods and compact finite difference methods are used to solve the wave equation in non-periodic domains. The problem is defined as

$$\begin{aligned} u_t + u_x &= 0 & \text{for } 0 < x < 1, \\ u(0, t) &= \exp(-ikt) \end{aligned} \quad (10)$$

The exact solution assuming periodicity in time is

$$u(x, t) = \exp(ik(x - t)) \quad (11)$$

For numerical solution, it is assumed that $u(x, t)$ takes the form $u(x, t) = v(x)\exp(-ikt)$ and solve the following equations for $v(x)$:

$$\begin{aligned} ikv &= \frac{dv}{dx}, \\ v(0) &= 1 \end{aligned} \quad (12)$$

The equation is discretized with B-spline collocation and compact finite difference schemes on both uniform and non-uniform grids.

4.1. B-spline Collocation Formulation

As mentioned in section 2.1.3, collocation points at the B-spline maxima are selected. In general, using this “B-spline maxima” collocation formulation with splines of order d , matrices with $d + 1$ non-zero diagonals will be obtained. In the case of uniform grids away from the boundary, there are only d non-zero diagonals as the maxima of splines coincide with the knot points. After discretization, a matrix equation $i\omega M\alpha = D_1\alpha$ is obtained, where M and D_1 are the mass and first derivative operator matrix, and α is the B-spline coefficient vector.

The boundary condition is implemented by replacing the operator at the boundary collocation point with $v_0 = 1$.

4.2. Compact Finite Difference Formulation

Lele presents a comprehensive study of high resolution finite difference schemes [23]. In his paper, the effective wavenumber in a periodic domain is investigated. For domains with non-periodic boundaries, the same analysis is used to obtain the effective wavenumbers both for the interior and the special boundary schemes. The effective wavenumbers for the boundary schemes are in general complex, with the real part associated with the dispersive error and the imaginary part associated with the dissipative error. The conservative formulation, eigenvalue analysis and stability limits for explicit schemes are also presented. For the details, the reader is directed to [23].

In this section, two issues are addressed. The first is an alternative approach to studying the boundary formulation, instead of the effective wavenumber analysis of Lele. The second is the formulation of schemes with non-uniform grids. The same problem is then solved which offers direct comparison with the B-spline collocation method.

4.2.1. Boundary formulation

To discretize the hyperbolic equation, the numerical schemes need to resolve the traveling waves in the domain. The boundary formulation is studied using normal modal analysis. Normal modal

analysis is also used by Carpenter *et al* [5] to investigate the stability of boundary treatments for compact finite difference schemes. The similarities of these two analyses will be pointed out after the description of the current boundary formulation.

In the interior, the compact finite difference approximation of the first derivative is derived from equation (8), which can be rewritten more generally as :

$$v'_i + \sum_{j=1}^m \alpha_j (v'_{i+j} + v'_{i-j}) = \sum_{j=1}^m a_j \frac{v_{i+j} - v_{i-j}}{2j\Delta x} \quad (13)$$

where m is related to the matrix bandwidth w by $m = \frac{w-1}{2}$. Knowing that $v' = ikv$, the following expression is obtained :

$$\sum_{j=1}^m c_j v_{i-j} + ikv_i - \sum_{j=1}^m c_j^* v_{i+j} = 0 \quad (14)$$

where $c_j = \frac{a_j}{2j} + i\alpha_j k\Delta x$ and c_j^* is the conjugate of c_j . This can be interpreted as a linear recursion relation for v_i . Such a recursion has solutions Λ^j , where Λ is a function of k . Substituting $v_j = \Lambda^j$ into equation (14), the characteristic polynomial is obtained :

$$\sum_{j=1}^m c_j \Lambda^{-j} + ik - \sum_{j=1}^m c_j^* \Lambda^j = 0 \quad (15)$$

which has $2m$ roots. In general, if Λ_+ is a root, then $\Lambda_- = \Lambda_+^{*-1}$ is also a root. These root pairs are denoted as type I root pairs. If $|\Lambda| = 1$, $\Lambda = \Lambda^*^{-1}$. In this case there can be two independent roots. These roots are denoted as type II roots. In the limit $k \rightarrow 0$, equation (15) has the form

$$\sum_{j=1}^m \frac{a_j}{2j} (\Lambda^{-j} - \Lambda^j) = 0 \quad (16)$$

which always has the solutions

$$\Lambda - \Lambda^{-1} = 0 \Rightarrow \Lambda = \pm 1 \quad (17)$$

Changing notation to that of effective wavenumbers,

$$\Lambda = \exp(i\tilde{k}\Delta x) \Rightarrow u(x, t) = \exp\left(i\tilde{k}\left(x - \frac{k}{\tilde{k}}t\right)\right) \quad (18)$$

type I root pairs correspond to conjugate pairs of complex effective wavenumbers \tilde{k} and \tilde{k}^* , while type II roots yield real \tilde{k} . Conjugate pairs of complex effective wavenumbers represent a pair of solutions, one of which grows exponentially in amplitude to the right, the other to the left. Also, for $k = 0$, the two solutions yield $\tilde{k} = 0$ and $\tilde{k} = k_{max}$. Clearly, of the $2m$ solutions, only one solution with real \tilde{k} can be a valid approximation to the exact solution. The remainder are spurious. When equation (13) is used to solve equation (12), the coefficients of the various solutions are determined by the boundary conditions and special differencing schemes used near the boundaries. Clearly, the boundary schemes should be chosen to make the amplitudes of spurious solutions as small as possible.

To see how this works, consider the tridiagonal and pentadiagonal interior scheme (see table 1). For these two cases, the coefficients in the characteristic polynomials and their corresponding roots are given in table 5. Λ_2 and Λ_3 are complex conjugate pairs while Λ_0 and Λ_1 have magnitude 1. Λ_0 represents the approximation to the exact solution $\exp(ik\Delta x)$ to the order associated with the scheme and it has a positive group velocity. Λ_1 is a spurious wave with a negative group velocity. Λ_2 and Λ_3 are spurious waves growing exponentially in magnitude to the right and left respectively. For the spurious waves that grow exponentially to the right, the magnitude of the waves is largest at the right boundary. Thus, by arranging the right boundary schemes to make the Λ_2 wave (for example) small at the right boundary, the Λ_2 solution is small everywhere, regardless of the length of the domain. Similarly waves growing to the left (e.g. Λ_3), should be controlled at the left boundary. For waves with $|\Lambda| = 1$, or equivalently real \tilde{k} , the “group velocity” $v_g = d\tilde{k}/dk$ determines which boundary should control the wave. With positive group velocity, the left boundary controls the wave because when solving the transient problem (10), information from the boundary will propagate into the domain from the left. Similarly, waves with negative group velocity are controlled at the right boundary. Thus the spurious solution Λ_1 will be controlled by the right boundary scheme, while the physical boundary conditions at the left boundary will control the physical solution Λ_0 .

To determine the appropriate inflow boundary schemes, consider the general solution, which near the inflow boundary can be written as

$$v_j = p_0 \Lambda_0^j + p_3 \Lambda_3^j + O((k\Delta x)^n) \quad (19)$$

where n is the order of the error in the interior scheme (5 or 9 for tridiagonal and pentadiagonal schemes respectively). Note that for the tridiagonal scheme, Λ_2 and Λ_3 can be considered to be zero. The $O((k\Delta x)^n)$ term is the contribution of the Λ_1 and Λ_2 waves, which will be this small by construction of the right boundary schemes. Using this expression, the left boundary schemes are constructed to make $p_0 = 1 + O((k\Delta x)^n)$ and $p_3 = O((k\Delta x)^n)$ (for the pentadiagonal scheme). This is accomplished using schemes of the form

$$\sum_{j=0}^{m+i} \alpha_{ij} v_j' = \frac{1}{\Delta x} \sum_{j=0}^{3m-i} a_{ij} v_j \quad \text{for } 0 \leq i \leq m-1 \quad (20)$$

for the first $m = \frac{w-1}{2}$ points, except for the boundary point ($i = 0$) which is replaced by the boundary condition $v_0 = 1$. The coefficients for bandwidth 3 and 5 ($m = 1$ and 2) are shown in table 6. A Taylor series analysis of these schemes shows them to be of the same order as the interior scheme, and indeed this is how they were derived. This appears to be a sufficient condition for the suppression of the spurious waves to the desired order, though the theory of Gustafsson ([15] and [5]) implies that boundary schemes one order lower than the interior should be adequate.

Near the outflow boundary, the general solution can be written similarly to (19)

$$v_{N-l} = p_0' \Lambda_0^{-l} + p_1' \Lambda_1^{-l} + p_2' \Lambda_2^{-l} + O((k\Delta x)^n) \quad (21)$$

where $p_i' = p_i \Lambda_i^N$ and N is the grid number of the right boundary. Boundary schemes that are “mirror images” of the left boundary scheme result in $p_1' = p_1$ and $p_2' = O((k\Delta x)^n)$ (pentadiagonal

TABLE 5
Coefficients and roots of characteristic polynomials. The various coefficients in the expressions for Λ are given to four digit accuracy.

TABLE 5a
Coefficients of characteristic polynomials

Band-width	c_1	c_2
3	$\frac{3}{4} + \frac{1}{4}ik\Delta x$	N.A.
5	$\frac{20}{27} + \frac{4}{9}ik\Delta x$	$\frac{25}{216} + \frac{1}{36}ik\Delta x$

TABLE 5b
Roots of characteristic polynomials

Band-width	Λ_0	Λ_1	Λ_2	Λ_3
3	$\exp(ik\Delta x)$ $+O((k\Delta x)^5)$	-1.0000 $+0.3333 ik\Delta x$ $+0.0555(k\Delta x)^2 + \dots$	N.A.	N.A.
5	$\exp(ik\Delta x)$ $+O((k\Delta x)^9)$	-1.0000 $+0.1636 ik\Delta x$ $+0.0134(k\Delta x)^2 + \dots$	-6.2397 $+1.1118 ik\Delta x$ $-0.0733(k\Delta x)^2 + \dots$	-0.1603 $+0.0286 ik\Delta x$ $+0.0070(k\Delta x)^2 + \dots$

scheme). Thus we have

$$\sum_{j=0}^{m+N-i} \alpha_{N-i-j} v'_{N-j} = \frac{1}{\Delta x} \sum_{j=0}^{3m-N+i} -a_{N-i-j} v_{N-j} \quad \text{for } N \geq i \geq N-m+1 \quad (22)$$

where again the coefficients are given in table 6.

The boundary scheme analysis presented here is similar to the GKS stability analysis of boundary treatments in Carpenter *et al* [5], in which a similar model problem is used and in which the same spurious waves are treated. However, in Carpenter *et al*, the assumed temporal form of the solution is more general in that the frequency k (in our notation, see (10)) is allowed to be complex. The concern is then whether the time-periodic solutions of (10) of the form used here are stable. For the fourth order tridiagonal scheme, Carpenter *et al* show the combined interior and boundary schemes to be GKS stable, but they do not treat the eighth order pentadiagonal scheme discussed here. It seems plausible that interior and boundary schemes that consistently suppress the spurious waves as discussed here will be GKS stable. But this remains to be seen.

4.2.2. Non-uniform grids

Another issue that needs to be addressed is the formulation of the compact finite difference scheme with non-uniform grids. The approach is to apply a mapping which uses the uniform mesh scheme in the mapped coordinate. The mesh mapping is given in equation (7). The discretization

TABLE 6
Coefficients of the boundary formulation for the first derivative.

Band-width	i	α_{i0}	α_{i1}	α_{i2}	α_{i3}
3	0	1	3	0	0
5	0	1	12	15	0
5	1	$\frac{1}{15}$	1	2	$\frac{2}{3}$

Band-width	i	a_{i0}	a_{i1}	a_{i2}	a_{i3}	a_{i4}	a_{i5}	a_{i6}
3	0	$-\frac{17}{6}$	$\frac{3}{2}$	$\frac{3}{2}$	$-\frac{1}{6}$	0	0	0
5	0	$-\frac{79}{20}$	$-\frac{77}{5}$	$\frac{55}{4}$	$\frac{20}{3}$	$-\frac{5}{4}$	$\frac{1}{5}$	$-\frac{1}{60}$
5	1	$-\frac{247}{900}$	$-\frac{19}{12}$	$\frac{1}{3}$	$\frac{13}{9}$	$\frac{1}{12}$	$-\frac{1}{300}$	0

equations (8),(20) and (22) are modified by the mesh mapping

$$\left. \frac{dv}{dx} \right|_i = \left. \frac{dv}{d\xi} \right|_i \left. \frac{d\xi}{dx} \right|_i \quad (23)$$

Thus the equation to be solved is $\frac{dv}{d\xi} \frac{d\xi}{dx} = ikv$. The same interior and boundary scheme are then used in ξ .

4.3. Comparison

Tests based on the solution of the wave equation were carried out with $N = 100$. Before discussing the results, however, it should be noted that different from the effective wavenumbers, the accuracy of the solution of the wave equation is dependent of the number of intervals N apart from the wavenumber. In this sense the results here are less general than those of the effective wavenumber. Nevertheless, using the same N for both schemes allows us to compare their order of convergence and resolution.

The results on uniform grids are discussed first. The L_2 errors in the representation of the solution of the wave problem using B-spline collocation and compact finite difference methods are shown in figure 7. For B-spline collocation methods, the errors vary with k like k^{w+2} . Notice that in periodic domains, the convergence rates of the eigenvalue of the first derivative operator and the eigenfunction are k^{w+2} and k^{w+1} respectively (see figures 4, 6 and table 3). For compact finite difference schemes, the L_2 error varies with k like k^{2w-1} . This is consistent with the theoretical convergence rate (figure 4 and table 3). However, the curve is not smooth as there are many small wriggles on it. Apparently, the boundary condition and boundary schemes do not affect their convergence rate of either scheme.

As mentioned before, changing N would affect the error curves. In particular, the error curves shift vertically. This is because for both schemes, the local truncation error and hence the L_2 error have the form $\alpha(\Delta x)^{i-1} f^{(i)}(x)$, where α is a real constant and i is an integer ([23] and [31]). One way to obtain a curve that is valid for all N is to plot error/ N versus k/k_{max} . The resulting curve would not shift as N changes except when the error is close to 1.

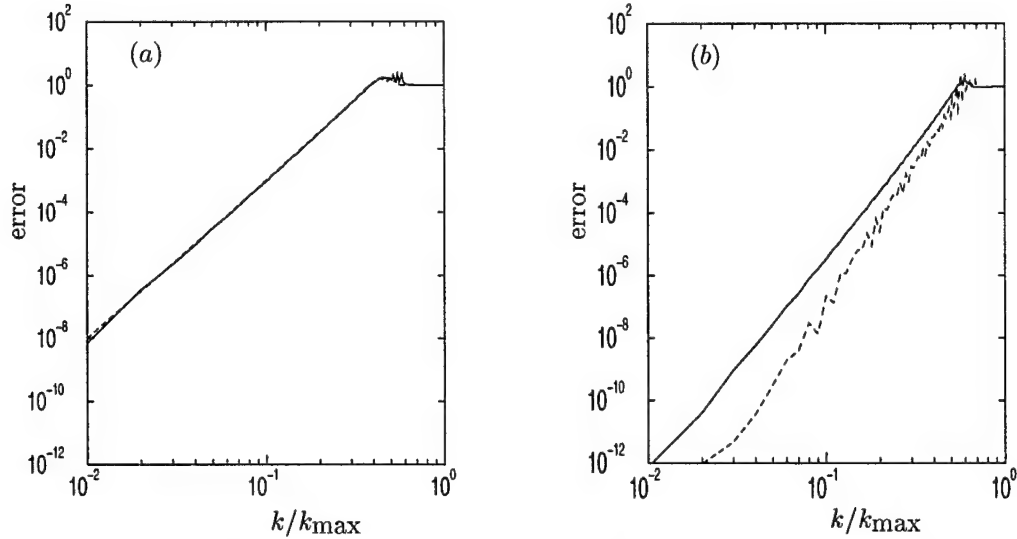


FIG. 7. L_2 error in the representation of the solution of the wave equation with wavenumber k on uniform grids for matrix bandwidth (a)3, (b)5: —, b-spline collocation; ---, compact finite difference.

Perhaps more important than the order of convergence is the resolution of the two schemes. The well-resolved fraction of the wavenumber range for the solution of the wave equation is shown in table 7. It can be seen that for tridiagonal schemes, the two have almost the same resolution. For pentadiagonal schemes, compact finite difference has better resolution due to the higher order of convergence.

Another issue is the effect of a non-uniform grid. The L_2 errors in the representation of the solution of the wave problem using the two numerical schemes on non-uniform grids are shown in figure 8. Here, the wavenumber is normalized by the maximum wavenumber $k_{max} = \frac{\pi}{\Delta x_{max}}$, where Δx_{max} is the maximum grid spacing. Basically, both schemes maintain the same convergence rate as in the case of uniform grids. Note that for the compact finite difference schemes, the curves turn up at the lowest wave number and the cause is not clear. With regard to the resolved fraction, table 8 indicates that the two tridiagonal schemes again have the same resolution. (Note however that in non-uniform grids, B-spline collocation has elements outside the three "main" diagonals in the interior.) For pentadiagonal schemes, compact finite difference has better resolution.

The order of convergence of the two schemes suggests that the difference in resolution properties between compact finite difference and B-spline collocation will become bigger as the matrix bandwidth increases. However, the wriggles on the compact finite difference curves may decrease its resolution. Also, comparing results in periodic domains (table 7 and table 4), it is found that the resolution in finite domains is substantially lower. In particular, the error reaches 1 at $k/k_{max} \approx 0.6$ and then levels off.

Comparison of the numerical solution and the analytical solution as functions of x suggests what happens at the plateau of the error curve. Before the error plateau, the numerical solution is capturing the propagating wave, although the numerical and analytical solution are getting more and more out of phase as x increases in the domain. This is expected as the effective wavenumber is not exact. At the error plateau, the numerical solution cannot capture the propagating wave at all. Small wriggles appear at the inflow boundary and gradually die away as x increases.

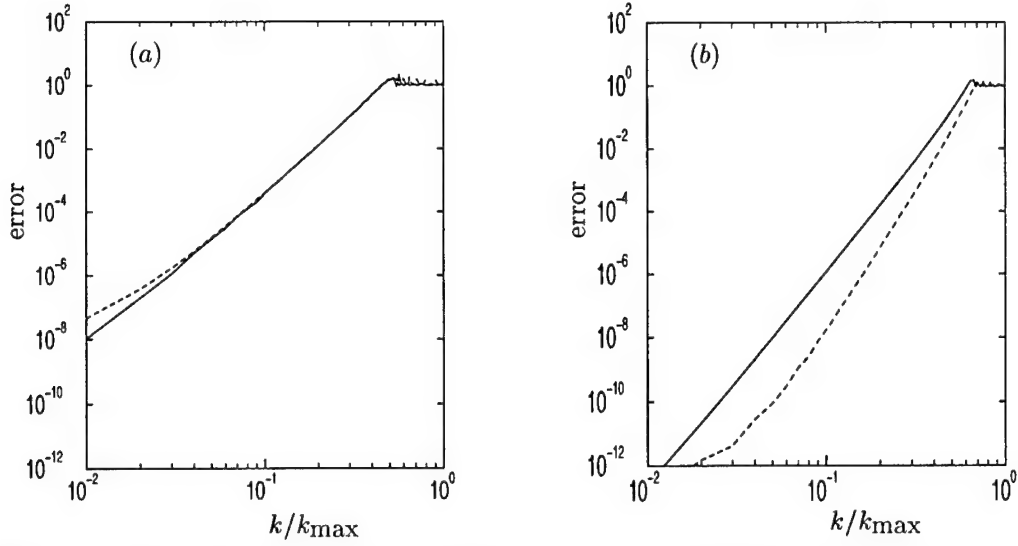


FIG. 8. L_2 error in the representation of the solution of the wave equation with wavenumber k on non-uniform grids for matrix bandwidth (a)3, (b)5: —, b-spline collocation; ---, compact finite difference.

TABLE 7

Resolved fraction for the solution of the wave equation for uniform grid distribution

Bandwidth	B-spline collocation			compact finite difference		
	10 %	1 %	0.1 %	10 %	1 %	0.1 %
3	0.25	0.15	0.10	0.24	0.15	0.09
5	0.40	0.30	0.22	0.45	0.34	0.27

TABLE 8

Resolved fraction for the solution of the wave equation for non-uniform grid distribution

Bandwidth	B-spline collocation			compact finite difference		
	10 %	1 %	0.1 %	10 %	1 %	0.1 %
3	0.29	0.19	0.12	0.29	0.19	0.12
5	0.47	0.35	0.25	0.55	0.43	0.34

5. HEAT EQUATION IN BOUNDED DOMAINS

In this section, the eigenvalue problem arising from the heat equation is solved using B-spline collocation and compact finite difference methods. The problem is defined as

$$v'' = \lambda v \quad \text{for } 0 < x < 1, \quad (24)$$

with some boundary conditions, the most common ones being the Dirichlet ($v(0) = v(1) = 0$) and Neumann ($v'(0) = v'(1) = 0$) boundary conditions. In both cases, the eigenvalues are

$$\lambda_k = -(\pi k)^2, \quad (25)$$

where k is an integer. The corresponding eigenfunctions are $\tilde{v}_k(x) = \sin(\pi k x)$ and $\tilde{v}_k(x) = \cos(\pi k x)$ for Dirichlet and Neumann boundary conditions respectively.

5.1. B-spline Collocation Formulation

Discretizing with B-spline collocation method, we obtain the matrix equation $\lambda M \alpha = D_2 \alpha$, where M is the mass and D_2 the second derivative operator matrix, and α the B-spline coefficient vector for the eigenfunctions. For Dirichlet boundary conditions, $v_0 = v_N = 0$. For Neumann boundary conditions, v'_0 and v'_N are set to zero.

5.2. Compact Finite Difference Formulation

Similar to the case of first derivative, the discretized derivative operators are derived from equation (9) in the interior. Near the boundary, the symmetry breaks down and the corresponding equation becomes

$$\begin{aligned} \sum_{j=0}^{m+i} \alpha_{ij} v_j'' &= \frac{1}{(\Delta x)^2} \sum_{j=0}^{3m+1-i} a_{ij} v_j \quad \text{for } 0 \leq i \leq m-1, \\ \sum_{j=0}^{m+N-i} \alpha_{N-i-j} v_{N-j}'' &= \frac{1}{(\Delta x)^2} \sum_{j=0}^{3m+1-N+i} a_{N-i-j} v_{N-j} \quad \text{for } N \geq i \geq N-m+1 \end{aligned} \quad (26)$$

where $m = \frac{w-1}{2}$. The coefficients in equation (26) are determined by matching the Taylor series coefficients to one order less than the interior for tridiagonal schemes and to the same order of the interior for pentadiagonal schemes (using boundary of the same order for tridiagonal schemes gives rise to bad resolution for unknown reasons). The coefficients are shown in table 9 for the two schemes. After discretization, a generalized eigenvalue problem $\lambda M_2 \alpha = D_2 \alpha$ is obtained, where M_2 is the mass and D_2 the second derivative operator matrix, and α the eigenfunction. The generalized eigenvalue problem can be solved with the appropriate boundary condition.

5.2.1. Boundary conditions

The Dirichlet boundary conditions are implemented by setting $v_0 = v_N = 0$. For Neumann boundary conditions, a one-sided explicit (i.e. not compact) finite difference scheme is used to set $v'_0 = v'_N = 0$. Note that this makes the boundary scheme inconsistent with the interior scheme. Also, a very long one-sided finite difference expression is required to maintain the same order as the interior compact finite difference approximations.

TABLE 9
Coefficients of the boundary formulation for the second derivative

Band-width	i	α_{i0}	α_{i1}	α_{i2}	α_{i3}
3	0	1	11	0	0
5	0	1	3.36092×10^1	1.17128×10^2	0
5	1	3.34302×10^{-2}	1	3.39390	8.58850×10^{-1}

Band-width	i	a_{i0}	a_{i1}	a_{i2}	a_{i3}	a_{i4}
3	0	13	-27	15	-1	0
5	0	2.15798×10^1	1.03882×10^2	-2.92763×10^2	1.91514×10^2	-2.87907×10^1
5	1	6.76347×10^{-1}	2.77175	-7.06964	3.10065	5.39365×10^{-1}

Band-width	i	a_{i5}	a_{i6}	a_{i7}
3	0	0	0	0
5	0	5.25826	-7.32139×10^{-1}	5.24768×10^{-2}
5	1	-1.89438×10^{-2}	4.74627×10^{-4}	0

5.2.2. Non-uniform grids

To solve the problem on a non-uniform grid, a mesh mapping is used as in the wave equation. Notice from the chain rule

$$\frac{d^2 v}{dx^2} = \left(\frac{d\xi}{dx} \right)^2 \frac{d^2 v}{d\xi^2} + \frac{d^2 \xi}{dx^2} \frac{dv}{d\xi} \quad (27)$$

The derivative in the non-uniform x coordinate is expressed in terms of those in the transformed uniform ξ coordinate. In the ξ coordinate, there are finite difference representation of the derivative operators (expressed as $M_1^{-1}D_1$ and $M_2^{-1}D_2$. Note that M_1 and M_2 are different). The finite difference approximation of the second derivative operator can hence be expressed as in equation (27).

5.3. Comparison

Tests based on the eigenvalue problem are performed using $N = 30$. Results based on different N suggest that N has no influence on the order of convergence and minor influence on the well-resolved fraction. The results obtained on uniform grids are presented first. The errors in approximating the eigenvalues are shown in figure 9. Regardless of the boundary conditions, B-spline collocation schemes have eigenvalue errors which decrease with wavenumber as k^{w+1} , while compact finite difference has a convergence rate of k^{2w} . Both of the above are consistent with their corresponding convergence rates in periodic domains (see table 3). For compact finite difference, however, the boundary conditions do have an effect on the magnitude of the error. Neumann boundary conditions give larger errors in the eigenvalues, perhaps due to the boundary approximation of v' . Also with the compact finite difference, there are some sharp decrease in error at particular wavenumbers for reasons that are not clear. At high wavenumbers, wriggles appear on the compact finite difference curves irrespective of the boundary conditions. With regard to resolution, we refer to table 10, which gives the resolved fraction for the eigenvalues. In many cases, compact finite difference schemes provide better resolution for the eigenvalues. However, for pentadiagonal scheme, B-splines have better resolved fractions in many cases. However, due to the high convergence order of the compact finite difference, the more stringent the tolerance for resolved fractions, the better the compact finite difference does.

The L_2 errors of the eigenfunctions of the heat equation are shown in figure 10. For the B-spline collocation schemes, the convergence rate for both Dirichlet and Neumann boundary conditions appears to be k^{w+1} , but in the Neumann case this asymptotic rate is not attained until $k < 0.06$, with the resulting impact on resolution. For compact finite difference schemes, the eigenfunctions have errors that converge at a rate approximately equal to k^{2w} . However, with Neumann boundary conditions, the errors are again larger. In fact, using Dirichlet boundary condition, the tridiagonal schemes give a solution that is exact to round-off errors. It is also very interesting to note that the pentadiagonal scheme curve shows two sharp decrease at $\sqrt{-\lambda}/k_{max} = \frac{1}{3}$ and $\sqrt{-\lambda}/k_{max} = \frac{2}{3}$. At these two particular wavenumbers, the symmetries of the approximate eigenfunctions make the point representations exact. Table 11 shows the resolved fraction of eigenfunctions. Same as for the eigenvalues, compact finite difference schemes in general provide better resolution for tridiagonal methods while B-splines do better for pentadiagonal schemes.

On non-uniform grids, the behavior of both B-spline collocation and compact finite difference schemes is shown in figures 11, 12, tables 12 and 13. The errors in the eigenvalues of the heat equation are shown in figure 11. B-spline collocation methods maintain the same convergence rate of k^{w+1} as in the case of uniform grids irrespective of the boundary conditions. Compact finite difference schemes, however, show a degradation. Convergence rates of the eigenvalues is

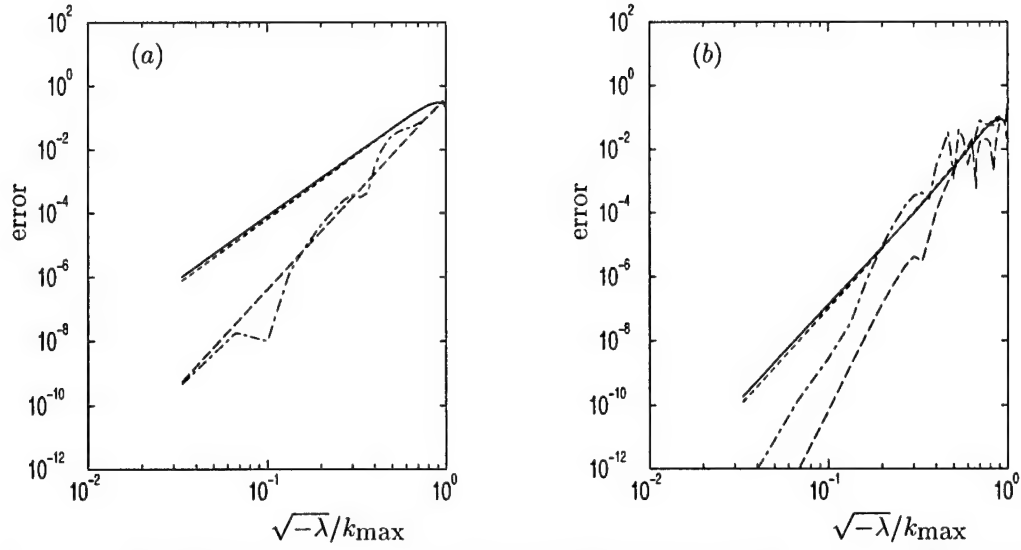


FIG. 9. Error of the eigenvalues of the heat equation with wavenumber k on uniform grids for matrix bandwidth (a)3, (b)5: —, Dirichlet boundary condition; ---, Neumann boundary condition, both for b-spline; - · -, Dirichlet boundary condition; · · · ·, Neumann boundary condition, both for compact finite difference

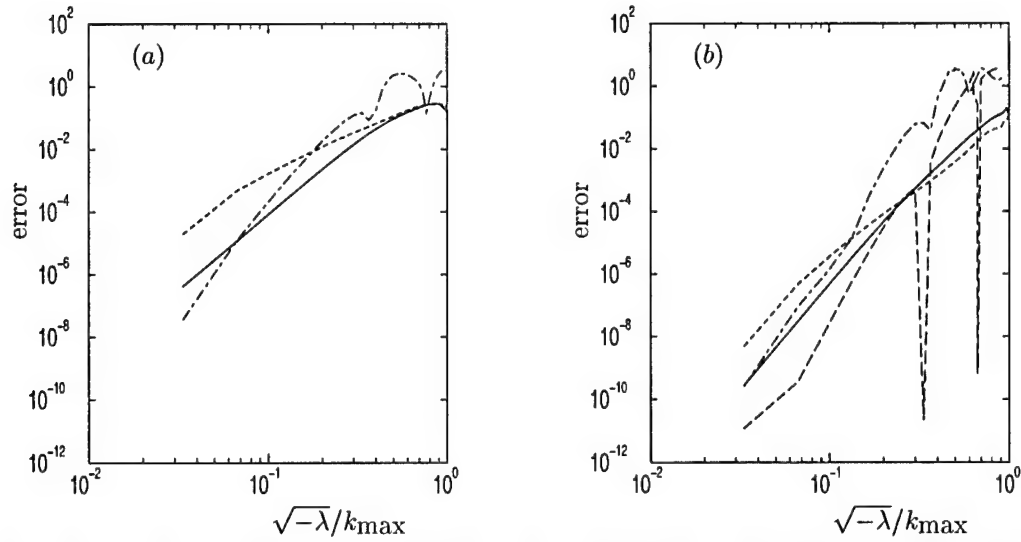


FIG. 10. Error of the eigenfunctions of the heat equation with wavenumber k on uniform grids for matrix bandwidth (a)3, (b)5: —, Dirichlet boundary condition; ---, Neumann boundary condition, both for b-spline; - · -, Dirichlet boundary condition; · · · ·, Neumann boundary condition, both for compact finite difference. For the compact finite difference, with bandwidth of 3 and Dirichlet boundary conditions, the eigenfunctions are exact to round-off errors.

TABLE 10
Resolved fraction for the eigenvalues for uniform grid distribution

Bandwidth	Boundary condition	B-spline collocation			compact finite difference		
		10 %	1 %	0.1 %	10 %	1 %	0.1 %
3	Dirichlet	0.33	0.10	0.03	0.66	0.36	0.20
3	Neumann	0.36	0.10	0.03	0.46	0.36	0.16
5	Dirichlet	0.80	0.46	0.26	> 0.76	0.50	0.40
5	Neumann	0.76	0.46	0.26	0.43	0.36	0.23

TABLE 11
Resolved fraction for the eigenfunctions for uniform grid distribution

Bandwidth	Boundary condition	B-spline collocation			compact finite difference		
		10 %	1 %	0.1 %	10 %	1 %	0.1 %
3	Dirichlet	0.43	0.23	0.13	1.00	1.00	1.00
3	Neumann	0.40	0.13	0.06	0.23	0.16	0.10
5	Dirichlet	0.73	0.46	0.30	0.43	0.37	0.33
5	Neumann	0.93	0.56	0.33	0.36	0.20	0.16

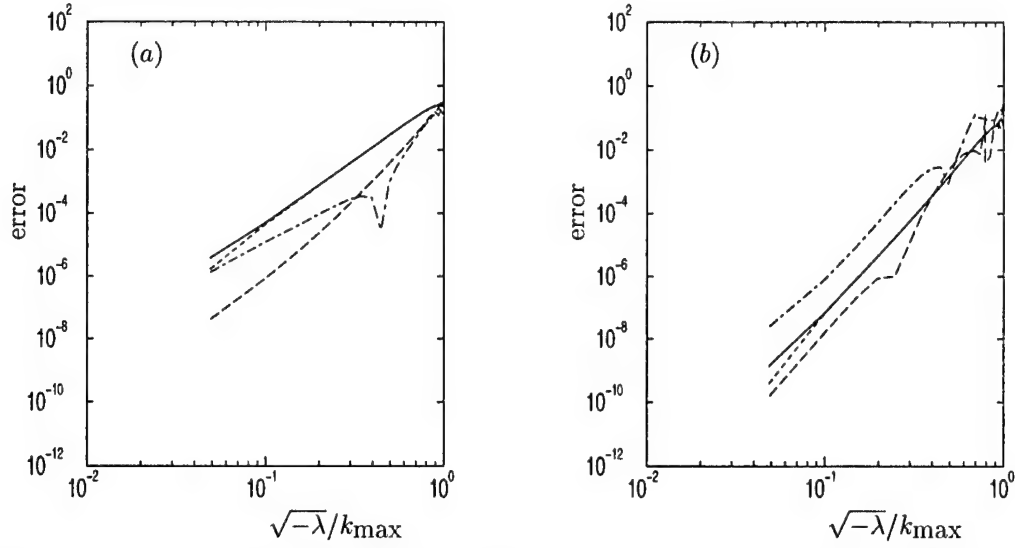


FIG. 11. Error of the eigenvalues of the heat equation with wavenumber k on non-uniform grids for matrix bandwidth (a)3, (b)5: —, Dirichlet boundary condition; ---, Neumann boundary condition, both for b-spline; - - -, Dirichlet boundary condition; - · - · -, Neumann boundary condition, both for compact finite difference

TABLE 12

Resolved fraction for the eigenvalues for non-uniform grid distribution

Bandwidth	Boundary condition	B-spline collocation			compact finite difference		
		10 %	1 %	0.1 %	10 %	1 %	0.1 %
3	Dirichlet	0.44	0.09	< 0.05	0.73	0.44	0.19
3	Neumann	0.44	0.14	0.04	0.74	0.54	0.44
5	Dirichlet	0.92	0.53	0.29	0.73	0.49	0.34
5	Neumann	0.97	0.53	0.29	0.54	0.29	0.14

2 to 3 orders less than the corresponding rate of k^{2w} on uniform grids, with Neumann boundary conditions giving worse convergence rates. Regarding resolution, compact finite difference provides better resolution for bandwidth $w = 3$ while B-spline collocation schemes provides better resolution for bandwidth $w = 5$.

The L_2 errors of the eigenfunctions of the heat equation are shown in figure 12. B-spline collocation schemes give convergence rates of k^w approximately, with Dirichlet boundary conditions giving slightly better solutions at low k . The degradation of resolution is not serious when non-uniform grids are used instead of uniform ones. Compact finite difference schemes, however, show quite serious degradation of convergence and resolution on non-uniform grids. They have convergence rates of about k^w , compared to k^{2w} on uniform grids. A very interesting result is that B-spline and compact finite difference schemes appear to have the same convergence rates on non-uniform grids. From table 13, it can also be seen that B-spline collocation methods have better resolution properties on non-uniform grids.

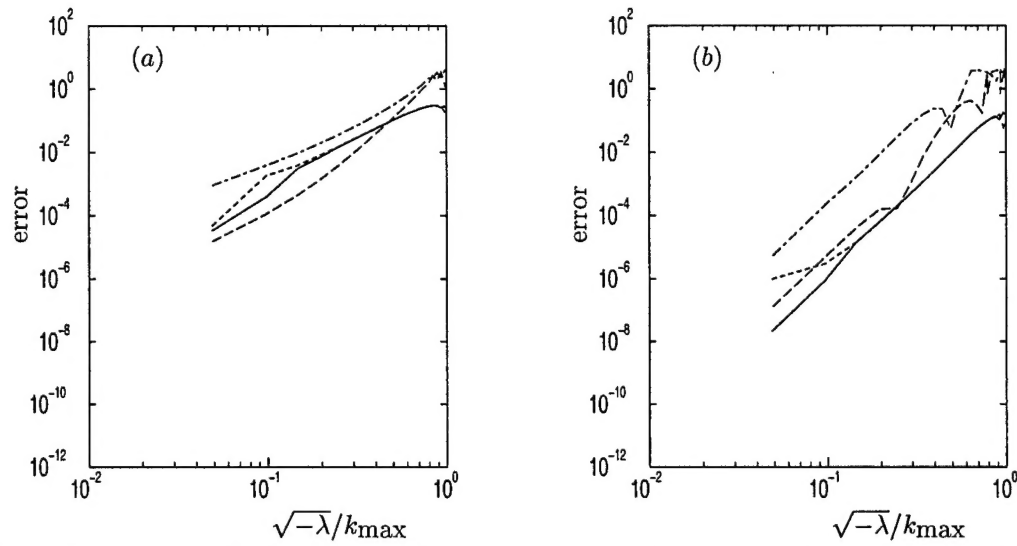


FIG. 12. Error of the eigenfunctions of the heat equation with wavenumber k on non-uniform grids for matrix bandwidth (a)3, (b)5: —, Dirichlet boundary condition; ---, Neumann boundary condition, both for b-spline; - - -, Dirichlet boundary condition; - · - · -, Neumann boundary condition, both for compact finite difference.

TABLE 13

Resolved fraction for the eigenfunctions for non-uniform grid distribution

Bandwidth	Boundary condition	B-spline collocation			compact finite difference		
		10 %	1 %	0.1 %	10 %	1 %	0.1 %
3	Dirichlet	0.39	0.19	0.09	0.44	0.24	0.14
3	Neumann	0.39	0.14	0.04	0.29	0.09	< 0.04
5	Dirichlet	0.72	0.43	0.29	0.39	0.29	0.24
5	Neumann	0.72	0.43	0.29	0.25	0.15	0.09

6. DISCUSSION AND CONCLUSIONS

The results of this paper indicate that in many situations compact finite difference schemes have better resolution and convergence properties than the other numerical methods tested. The comparisons were done for schemes with the same matrix bandwidths, which we use as a surrogate for computational cost. Furthermore, it was shown that finite element and B-spline Galerkin methods had inferior resolution to compact finite difference and B-spline collocation. There are several aspects of these results that deserve further discussion.

Regarding high-order finite element methods, it was noted that a reason for their relatively poor performance in these tests was their low-order (C_0) continuity at the element boundaries (i.e. knots), whereas the spline basis retains as high a degree of continuity as possible, given the order of the piecewise polynomial representation. In essence, in spline methods, an increase in the degree of the polynomials is used to increase the degree of continuity, while in C_0 finite elements, it is used to increase the number of degrees of freedom of the representation. The results of the tests here suggest that the added degrees of freedom do not produce much in the way of added accurately represented modes, resulting in poor resolution properties. However, the improved resolution of splines is not without cost; that is, the representation of the polynomials in each interval (element) is not isoparametric, a very convenient property of finite element representations. Consequently, it is much easier to formulate multi-dimensional finite elements on complex and/or unstructured grids, than it is to formulate spline methods.

It was also noted that piecewise polynomial Galerkin methods yielded poorer representations of complex exponentials (the derivative eigenfunction) than collocation methods. This is true for both finite element methods and spline methods. This is a curious result because Galerkin approximations minimize L_2 error for a given representation. The reason for the curious result is that we are comparing methods with the same matrix bandwidth. For example, a Galerkin method that yields pentadiagonal matrices has cubic polynomials, whereas a pentadiagonal collocation methods has quintic polynomials. The result is a fourth order accurate representation for Galerkin and a sixth order accurate representation for collocation. However, there are other reasons one might choose a Galerkin method, despite this shortcoming; for example, a Galerkin method is trivially shown to be conservative.

The two methods discussed here with the best convergence and resolution properties are compact finite difference and spline collocation, and the comparison between them includes 4 major issues that must be traded off against the improved order of accuracy and in many cases better resolution of the finite difference methods:

1. The generally superior convergence and resolution of compact finite difference compared to B-spline collocation is simply due to the fact that in the finite difference case, the "mass matrix" is not constrained to be the same for all derivatives. There may, however, be costs in code complexity or computational effort in having different mass matrices, depending on the details of the problem being solved.

2. Another difference is in the treatment near a boundary. In the finite difference case, special difference schemes must be formulated near the boundary, and such boundary treatments can cause difficulties. For the wave equation, a criterion for a good boundary treatment was developed in section 4.2.1, and schemes that satisfy the criterion were found by imposing a formal order of accuracy consistent with the interior scheme. However, consistent order of accuracy is a necessary but not necessarily sufficient condition for the criterion to be satisfied, and directly constructing schemes to satisfy the criterion is prohibitively cumbersome in all but the simplest cases (e.g. the tridiagonal scheme). Thus we do not have a practical constructive prescription

for boundary schemes that satisfy the criterion in section 4.2.1. In the heat equation problem, the development of a similar criterion for good boundary schemes is not as obvious, so we have an even less well defined procedure for the boundary treatment in this case. Finally, recall that for the heat equation, with Neumann conditions, an approximation of the first derivative at the boundary had to be devised, so the derivative boundary condition could be imposed. This was essentially ad hoc, and was not inherently consistent with the remainder of the scheme. All of these difficulties are obviated with the spline method, since there is no special treatment near the boundary.

3. On a nonuniform mesh, the spline method can be used directly, without recourse to a mapping to a domain with a uniform mesh, as we did for the finite difference case. Thus the method can easily be applied to an arbitrary mesh, for which no analytic mapping is known. Besides, the resulting approximations are simpler, with no explicit metric terms, and in the case of approximating the second derivative, no first derivative term appears. Of course, one can construct finite difference methods directly on a nonuniform mesh as well, but the process is cumbersome, and generally yields schemes that are lower order than the uniform mesh schemes (for the same matrix bandwidth).

4. In sections 4 and 5, the error associated with the spline collocation method was well-behaved and consistent with the results of the Fourier analysis in Section 3. The same cannot be said for the finite difference schemes. For them, the error spectra were more erratic, with a variety of unexplained features. Furthermore, in at least one case (i.e. nonuniform mesh heat equation with Neumann conditions), the convergence rates appeared to be the same as its spline counterpart, inconsistent with the simple Fourier analysis in Section 3.

Thus, when using a high-order spline collocation scheme instead of compact finite difference with the same bandwidth, one is trading away a potentially higher convergence rate and somewhat better resolution in many cases for a more straightforward and robust formulation. And, as suggested by the results of section 5, in complicated situations, there is no guarantee that the finite difference method would actually yield the theoretical higher convergence rate.

REFERENCES

1. A.J. Baker. *Finite element computational fluid mechanics*. McGraw-Hill, New York, 1983.
2. G. K. Batchelor. *The theory of Homogeneous Turbulence*. Cambridge University Press, Cambridge, 1982.
3. K. J. Bathe and V. Sonnad. In *Proceedings of AIAA Computers and Fluid Dynamics Conf.*, Palo Alto, California, 1981.
4. C. Canuto, M.Y. Hussaini, A. Quarteroni, and T. A. Zang. *Spectral Methods in Fluid Dynamics*. Springer-Verlag, Berlin, 1987.
5. M. H. Carpenter, D. Gottlieb, and S. Abarbanel. The stability of numerical boundary treatments for compact high-order finite-difference schemes. *J. Comput. Phys.*, 108(2), 1993.
6. A. M. Davies. Applications of the galerkin method to the solution of burger's equation. *Comput. Methods Appl. Mech. Engrg.*, 14, 1978.
7. A. M. Davies. The use of the galerkin method with a basis of b-splines for the solution of the one-dimensional primitive equations. *J. Comput. Phys.*, 27, 1978.
8. C. de Boor. *A Practical Guide to Splines*. Springer-Verlag, New York/Berlin, 1978.
9. H. Deconinck and C. Hirsch. In W. C. Reynolds and R. W. MacCormack, editors, *Proceedings of 7th International Conference on Numerical Methods in Fluid Dynamics*, New York/Berlin, 1980. Springer-Verlag.
10. P. Devloo, J. T. Oden, and P. Pattani. An $h - p$ adaptive finite element method for the numerical simulation of compressible flow. *Comput. Meths. Mech. Engrg.*, 70, 1988.
11. C. A. J. Fletcher. *Computational techniques for fluid dynamics*, volume 1. Springer-Verlag, Berlin/New York, 1991.

12. J. B. Freund, P. Moin, and S. K. Lele. Compressibility effects in a turbulent annular mixing layer. Technical Report TF-72, mech. engrg., stanford university, 1997.
13. D. J. Fyfe. The use of cubic splines in the solution of two point boundary value problem. *Compt. J.*, 12, 1969.
14. D. Gottlieb and S. A. Orszag. *Numerical Analysis of Spectral Methods*. SIAM, Philadelphia, 1977.
15. B. Gustafsson. *Math. Comput.*, 29(130), 1975.
16. M. T. Heath. *Scientific Computation : an Introductory Survey*. WCB, McGraw-Hill, 1997.
17. R. S. Hirsh. Higher order accurate difference solutions of fluid mechanics problems by a compact differencing technique. *J. Comput. Phys.*, 19, 1975.
18. G. E. Karniadakis. *Appl. Numer. Math.*, 6, 1989.
19. G. E. Karniadakis and S. A. Orszag. Some novel aspects of spectral methods, algorithmic trends in computational fluid dynamics. page 245. Springer-Verlag, 1993.
20. J. Kim, P. Moin, and R. D. Moser. Turbulence in channel flow at low reynolds number. *J. Fluid Mech.*, 177, 1987.
21. A. G. Kravchenko, P. Moin, and R. D. Moser. Zonal embedded grids for numerical simulation of wall-bounded turbulent flows. *J. Comput. Phys.*, 127, 1996.
22. H. O. Kreiss, S. A. Orszag, and M. Israeli. *Annu. Rev. Fluid Mech.*, 6, 1974.
23. S. K. Lele. Compact finite difference schemes with spectral-like resolution. *J. Comput. Phys.*, 103, 1992.
24. S. A. Orszag. *J. Fluid Mech.*, 49, 1971.
25. S. A. Orszag. *Stud. Appl. Math.*, 49, 1971.
26. D. Papamoschou and S. K. Lele. Vortex-induced disturbance field in a compressible shear layer. *Phys. Fluids A*, 5(6), 1993.
27. A. T. Patera. A spectral element method for fluid dynamics : laminar flow in a channel expansion. *J. Comput. Phys.*, 54, 1984.
28. R. S. Rogallo and P. Moin. Numerical simulation of turbulent flows. *Annu. Rev. Fluid Mech.*, 16, 1984.
29. S. G. Rubin and R. A. Graves. Viscous flow solutions with a cubic spline approximation. *Computers and Fluids*, 3, 1975.
30. S. G. Rubin and P. K. Khosla. Higher-order numerical solutions using cubic splines. *AIAA J.*, 1976.
31. S. G. Rubin and P. K. Khosla. Polynomial interpolation methods for viscous flow calculations. *J. Comput. Phys.*, 24, 1977.
32. K. Shariff and R. D. Moser. Two-dimensional mesh embedding for b-spline methods. *J. Comput. Phys.*, 145, 1998.
33. P. R. Spalart. Direct simulation of a turbulent boundary layer up to $Re_\theta = 1410$. *J. Fluid Mech.*, 187, 1988.
34. B. Swartz and B. Wendroff. *SIAM J. Numer. Anal.*, 11, 1974.
35. F. Thomasset. *Implementation of finite element methods for Navier-Stokes equations*. Springer-Verlag, Berlin, 1981.
36. R. Vichnevetsky and J. B. Bowles. *Fourier Analysis of Numerical Approximations of Hyperbolic Equations*. SIAM, Philadelphia, 1982.
37. K. N. S. Kasi Viswanadham and S. R. Koneru. Finite element method for one-dimensional and two-dimensional time dependent problems with b-splines. *Comput. Methods Appl. Mech. Engrg.*, 108, 1993.

ACKNOWLEDGMENT

This work is supported by AFOSR under grant F49620-97-1-0089.